Analysis of noise source mechanisms for a subsonic jet

Orla Power

A thesis submitted to the University of Dublin in partial fulfilment of the requirements for the degree of Ph.D.

Department of Mechanical & Manufacturing Engineering,
University of Dublin,Trinity College, Dublin, Ireland.

October, 2005

Declaration

I declare that this thesis has not been submitted for a degree at this or any other university and that any works carried out are my own unless otherwise referenced. In addition, I grant permission to the Trinity College Dublin Library to lend or copy this thesis upon request.

Orla Power,

October 2005

Abstract

Despite advances in engine design, from high bypass to co-axial or lobe shaped nozzles, the problem of jet noise reduction continues to require ongoing research in order to comply with the criteria inherent in environmental objectives set out by relevant bodies worldwide. Fundamental to this work, will be a clearer understanding of the generation and propagation of noise sources in subsonic jets.

In this regard, it is the aim of this thesis to identify and examine noise source mechanisms from a subsonic jet. The correlation between the velocity fluctuations inside the jet and the near-field acoustic pressure is measured and a multiple input / multiple output model is implemented. This identifies how each source, independent of all others, propagates and radiates into the near-field. Through the use of dedicated testing, specifically designed to extract information on source propagation, techniques such as those proposed in this work will lead to further understanding of how source terms behave in a subsonic jet.

For this purpose Laser Doppler Anemometry has proved to be an extremely useful technique since it enables very complex flow conditions to be measured successfully. Literature shows that the random acquisition of data associated with this technique has received considerable attention, with many methods available to process the random data.

This thesis contributes to the area of noise source identification in subsonic jets. In this thesis the time domain reconstruction procedure of Sample & Hold is validated against the most common alternative technique of Slot Correlation. The corrections associated with Sample & Hold for coincident data are detailed. This validated technique of Sample & Hold is then used to determine the velocity fluctuations and hence identify noise sources. A technique is proposed to extract

both the hydrodynamic and acoustic regions of the jet. Using this technique the hydrodynamic sources are successfully identified however the acoustic sources are contaminated by external vibrations. The identification technique used in the application of jet noise has proved beneficial in the understanding how noise sources behave.

Acknowledgements

EVERY ENGINEER....

Every little engineer needs a John Fitzpatrick for guidance, encouragement and support, thanks John.

Every engineer can't survive without other engineers - we feed off each other, some of us quite literally!!
for all those entertaining highs and lows, thanks to all.....

Every engineer works in a group - its better for socialising!!
thanks to Craig Meskell, the Fluids & Vibration group, can't forget those Thermo guys either!

Every engineer needs a mathematician (thanks for the '*Welcome to* $\frac{dy}{dx}$ ')
if any mistakes are present we know who to blame!

Every engineer also needs a non-engineer, who doesn't want to hear about jet noise all day long!!
thanks for keeping my sanity...

A special thanks must be given to Dr. Franck Kerhervé who very kindly supplied the Slot Correlation results. Finally, everyone who has supported me over the last number of years, and especially over the final weeks - these are the people who should be referenced for their work.

For those who never got to....

Contents

1 Introduction **1**

1.1 Objectives & Outline 3

2 Jet Noise **5**

2.1 Turbulent Shear Flows 6

2.2 Sources of Noise 7

2.3 Turbulence structures 9

2.4 Noise Pattern 10

2.5 Recent Developments in Jet Noise Research 13

2.6 Modelling & Prediction of Jet Noise 16

2.6.1 Aerodynamics 16

2.6.2 Source and Propagation Predictions 17

2.7 Summary 18

3 LDA Processing Techniques **20**

3.1 Sample & Hold 21

3.1.1 Non-coincident LDA Signals 24

3.1.2 Coincident LDA Signals 26

3.1.3 One LDA Signal & a Conventional Instrument 27

3.2 Slot Correlation 28

3.3 Concluding Remarks 31

4 Preliminary Analysis of LDA Data **32**

4.1 Sample & Hold Analysis 32

4.2 Comparison of Processing Techniques 35

4.2.1 Measurements 35
4.2.2 Auto Spectra 39
4.2.3 Cross Spectra 41
4.2.4 Coherence & Phase 42
4.2.5 Cross Correlation 45
4.2.6 Convection Velocity 46
4.2.7 Spatial-temporal correlations 48
4.2.8 Concluding Remarks 48
4.3 LDA acquisition modes 50
4.3.1 Velocity Fluctuations 51
4.3.2 Reynolds Stress Terms 53
4.3.3 Coherence estimates 58
4.3.4 Concluding Remarks 62

5 Acoustic Experimental Analysis **63**
5.1 Configuration 1 ($r/D = 1.1$) 68
5.1.1 Auto Spectra 68
5.1.2 Coherence 70
5.1.3 Phase 75
5.2 Configuration 2 ($r/D = 4.5$) 78
5.2.1 Auto spectra 79
5.2.2 Coherence 83
5.2.3 Phase 86
5.3 Concluding Remarks 88

6 Source Identification **91**
6.1 Five Input Model 92
6.2 Experimental Setup 94
6.3 Results 95
6.3.1 Configuration 1 98
6.3.2 Configuration 2 107
6.4 Concluding Remarks 111

7 Conclusions & Future Work **115**

List of Figures

2.1 Structure of a Jet 6
2.2 Longitudinal and Lateral Quadrupoles 8
2.3 Convection & Refraction 10
2.4 Cone of Silence 11
2.5 Geometry for quadrupole correlations 12
2.6 Jet Noise Pattern 13
2.7 kR demarcation at 1000Hz 15

3.1 Sample & Hold: Re-sampling a random acquired LDA signal at equal time intervals 21
3.2 Schematic of the Sample & Hold Procedure 22
3.3 Schematic of Two LDA signals 25
3.4 Schematic of an LDA signal and a conventional instrument (e.g. hot-wire or microphone) 27
3.5 The weighting scheme of the fuzzy slotting technique 30

4.1 Sample & Hold Filters (*a*) Continuous (*b*) Discrete 33
4.2 Auto Spectral estimation illustrating the Sample & Hold corrections 34
4.3 Noise to Signal Ratio 34
4.4 Close-up of the JEAN nozzle 36
4.5 One point / two component measurements performed at CEAT Poitiers, France under the JEAN contract 37
4.6 Axial distribution of the mean velocity components (measurements performed at CEAT Poitiers, France under the JEAN contract) . 38

4.7 Radial distribution of the mean velocity components (measurements performed at CEAT Poitiers, France under the JEAN contract) 39
4.8 Location of JEAN two-point measurements on Jet 3 40
4.9 Auto spectra of u': Comparison of Sample & Hold and Slot Correlation estimates 40
4.10 Cross spectrum of u'_1 & u'_2: Comparison of Sample & Hold and Slot Correlation estimates 41
4.11 Coherence estimates from the two-point measurements : comparison of Sample & Hold and Slot Correlation 43
4.12 Phase estimates: comparison of Sample & Hold and Slot Correlation 44
4.13 Cross Correlation estimates using Sample & Hold and Slot Correlation 46
4.14 Contour Correlation Curves from two-point / one-component measurements (a) Sample & Hold, (b) Slot Correlation 47
4.15 Convection Velocities as a function of frequency 48
4.16 Spatial and Temporal Correlation functions comparing Sample & Hold and Slot Correlation 49
4.17 Auto Spectrum of u' : Comparison between Coincident and Non-coincident modes 52
4.18 Noise to Signal Ratio of u' : Comparison between Coincident and Non-coincident modes 52
4.19 Auto Spectrum of v' : Comparison between Coincident and Non-coincident modes 53
4.20 Noise to Signal Ratio of v' : Comparison between Coincident and Non-coincident modes 54
4.21 Comparison between Coincident and Non-coincident modes of the Auto Spectrum of (a) u'^2 and (b) v'^2 55
4.22 Auto Spectrum of $u'v'$: Comparison between Coincident and Non-coincident modes 56

4.23 Noise to Signal Rations of $u'v'$: Comparison between Coincident and Non-coincident modes 56
4.24 Auto Spectrum of $u'v'$ (same data rates) : Comparison between Coincident and Non-coincident modes 57
4.25 Noise to Signal Rations of $u'v'$ (same data rates): Comparison between Coincident and Non-coincident modes 57
4.26 Uncorrected Coherence and Corrected Coherence between the velocity fluctuations and Reynolds stresses 60
4.27 Uncorrected Coherence and Corrected Coherence between (a) u' & v', (b) u' & $u'v'$ and (c) u'^2 & $u'v'$ 61

5.1 Schematic of experimental setup 64
5.2 TCD Jet 64
5.3 Jet Profile 65
5.4 Schematic of experimental setup 67
5.5 $r/D = 1.1$: Microphone Auto Spectra 68
5.6 $r/D = 1.1$: Coherence - Microphone 1 69
5.7 $r/D = 1.1$: Microphone Auto Spectra Conditioned 70
5.8 $r/D = 1.1$: Microphone Coherence (effects of conditioning) 71
5.9 $r/D = 1.1$: Microphone Coherence as a function of kR_j (effects of conditioning) 72
5.10 $r/D = 1.1$: Microphone Coherence - propagation 73
5.11 $r/D = 1.1$: Contour Coherence 74
5.12 $r/D = 1.1$: Contour Coherence conditioned 75
5.13 $r/D = 1.1$: Microphone Phase - frequency 76
5.14 $r/D = 1.1$: Microphone Phase - kR_j 77
5.15 $r/D = 1.1$: Microphone Phase - propagation 78
5.16 $r/D = 1.1$: Convection velocity as a function of frequency 78
5.17 $r/D = 4.5$: Microphone Auto Spectra 79
5.18 Coherence and Phase between vibrations and microphones 80
5.19 Vibration Analysis 81

5.20 $r/D = 4.5$: Coherence - Microphone 1 82
5.21 $r/D = 4.5$: Microphone Auto Spectra Conditioned 82
5.22 $r/D = 4.5$: Coherence - Microphone 2 83
5.23 $r/D = 4.5$: Microphone Coherence - propagation 84
5.24 $r/D = 4.5$: Contour Coherence 85
5.25 $r/D = 4.5$: Contour Coherence conditioned 86
5.26 $r/D = 4.5$: Microphone Phase 87
5.27 $r/D = 4.5$: Microphone Phase - propagation 88

6.1 Conditioned inputs & outputs 93
6.2 Experimental Setup at Trinity - combined LDA and acoustic measurements 94
6.3 LDA auto spectra - u 95
6.4 LDA auto spectra - v 96
6.5 LDA cross spectra 96
6.6 Corrected Coherence between LDA sources 97
6.7 $r/D = 1.1$: Ordinary Coherence between LDA sources and microphones 99
6.8 $r/D = 1.1$: Partial Coherence between LDA sources and microphones 100
6.9 $r/D = 1.1$: Partial Coherence between LDA and microphones . . 103
6.10 $r/D = 1.1$: Multiple Coherence 105
6.11 $r/D = 1.1$: norm + 0-4k: Angle of Frequency Response Function . 105
6.12 $r/D = 1.1$: Angle of Frequency Response Function 106
6.13 $r/D = 1.1$: Angle of Frequency Response Function - coincident data 108
6.14 $r/D = 4.5$: Ordinary Coherence & Conditioned coherence - Velocity fluctuations 109
6.15 $r/D = 4.5$: Ordinary Coherence & Conditioned coherence - Reynolds stresses 110
6.16 $r/D = 4.5$: Partial Coherence between LDA sources and microphones 111

6.17 $r/D = 4.5$: Multiple Coherence 112
6.18 $r/D = 4.5$: Angle of Frequency Response Function 113

List of Tables

4.1 JEAN temperature and velocity information 37

4.2 Length & Time Scales and Convection velocity estimates using Sample & Hold and Slot Correlation 49

4.3 Data rates and Re-sample rates for non-coincident and coincident modes 51

4.4 Sample time trace for two non-coincident signals measuring axial and radial velocities 58

5.1 Axial microphone positions 67

Nomenclature & Abbreviations

α	Noise to Signal Ratio
γ^2	Coherence
δ	Displacement
θ	angle to jet axis
σ^2	variance
ϕ	Phase
C_D	Corrected Doppler amplification factor
D	Diameter of jet
dt	time step
f	frequency
f_m	mean data rate
f_r	Re-sample rate
$G(f)$	One sided spectrum
k	Wavenumber
$L(f)$	filter
R	Radial distance
R_j	Radial distance from shear layer axis to the second measurement position (j)
$R(\delta, t)$	Correlation Curve
R_{ijkl}	Correlation function of the Lighthill tensor
r/D	Radial distance normalised by the diameter

T_λ	Taylor micro-scale
t	Time
u	Velocity vector
$\bar{u}$	Mean velocity
u'	Velocity fluctation
u'^2	Reynolds stress term
U_c	Convection Velocity
$u'_r(t)$	Reconstructed time series
$u'v'$	Reynolds stress term
U_0	Jet exit velocity
v'^2	Reynolds stress term
$x(t)$	Time signal
$X(f)$	Fourier transform
$X^*(f)$	Conjugate of Fourier transform
x/D	Axial distance normalised by the diameter

CFD	**C**omputational **F**luid **D**ynamics
DNS	**D**irect **N**umerical **S**imulation
FFT	**F**ast **F**ourier **T**ransform
HWA	**H**ot-**W**ire **A**nemometry
JEAN	**J**et **E**xhaust **A**erodynamic **N**oise
LDA	**L**aser-**D**oppler **A**nemometry
LEE	**L**inearised **E**uler **E**quations
LES	**L**arge **E**ddy **S**imulation
PSD	**P**ower **S**pectral **D**ensity
RANS	**R**eynolds-**A**veraged **N**avier-**S**tokes
SGS	**S**ubgrid **S**cale

Chapter 1

Introduction

Aeroacoustics is a discipline that unites such topics as acoustics, fluid mechanics, flow induced sound, and flow induced vibration. It is a multidisciplinary subject that has been slow to gain acknowledgment, particularly in engineering where it is essential to deal with problems related to environmental noise. There is a need to reduce noise and vibration due to aeroacoustic phenomena, but at the same time, that has regard to the effect on performance and cost. In the aeroplane industry, in this regard, it is particularly important to minimize the effects of any alterations or modifications to aircraft that would result in significant increases in dimensions and weight.

The pressures implicit in new directives and legislation at EC and international level, for example EC Directive $2002/30/EC$, ICAO Annex 16 Chapter 4, combined with the growing public awareness of the environmental issues involved have forced the aeroplane industry to seriously address the issue of sources of jet noise. In 1999 the World Health Organisation [1] published the Guidelines for Community Noise which stated *'taking all exposure to transportation noise together, about half of all European Union citizens are estimated to live in zones which do not ensure acoustical comfort to residents. More than* 30% *are exposed at night to equivalent sound pressure levels exceeding* $55dB(A)$*, which are disturbing to sleep.'* Aside from the nuisance factor, noise has been shown to be detrimental to health. Prolonged exposure to noise levels of $90dB$ can result in permanent damage to the auditory nerves. Levels of $120dB$ will cause pain and

'ringing' in the ear. Extensive damage to the nerves and sharp pain will occur with levels in the region of $140dB$. The most serious damage, resulting in mass destruction of the auditory nerves with a persistent ringing in the ears, occurs at levels of $150 - 160dB$. The noise levels in the vicinity of aircraft reach these dangerous levels of $160dB$.

At major airports around the world, including Dublin airport, legislation exists to limit the effect of noise in the surrounding areas. These measures require restrictions on maintaining certain flight paths immediately following takeoff, prioritisation of runways for noise abatement purposes and avoidance of reverse thrust procedures on landing specifically between the hours of $11pm$ and $6am$. Presently Dublin airport monitors noise levels using a Brüel & Kjaer system which consists of six fixed stations positioned around the airport in addition to two mobile units.

The aviation industry continues to experience significant growth with forecasts suggesting a demand for 7600 new aircraft every decade, representing a market investment of 1300 billion euro by 2019. In the three decades since aviation became an environmental issue, there have been significant improvements in noise abatement. For example, the noise footprint of an Airbus A320 is 80 per cent smaller than an older Boeing 727-200. The noise level of an Airbus A320 is approximately 20dB less than that of a Caravelle or Boeing 727 of 40 years ago. As reported by Ffowcs-Williams [2] the first generation Boeing 707 at take-off produced as much sound as the world population shouting in phase! A Boeing 767 of 30 years later (with four times as much thrust per engine) produced as much sound as the city of New York shouting in phase. Despite these advances the Aeronautics and Space Transportation Technology Enterprise of NASA has set 25 Year Deliverables to achieve $20dB$ community noise impact reduction relative to 1997 levels.

The total noise that radiates from a jet exhaust is often termed jet noise. In fact this total noise is comprised of several components. The most fundamental and most difficult to reduce is that due to the turbulent mixing of the jet exhaust with the ambient fluid downstream of the nozzle exit plane. The development of

high bypass ratio, low jet efflux velocity engines has brought about other sources, referred to as excess noise, tailpipe noise, or core noise. High bypass ratio engines have led to a reduction in aircraft noise, although this is a direct result of the lowered velocity compared to the low bypass engines. While the combined noise produced by a jet engine may be dominated by fan noise, the jet exhaust is still the most dominant source at full power. Without significant improvements in technology the maximum bypass ratio is limited by many factors, for example rotor speed and length of fan blades, and currently modern engines operate at near this maximum value. Therefore the procedure of increasing the bypass ratio to reduce the jet noise is limited.

1.1 Objectives & Outline

Previous experimental work into the origin of jet noise has used statistical methods to obtain information on noise sources. These techniques have resulted in the accumulation of useful information regarding the average noise source location but have failed to provide detailed information regarding the noise generation mechanisms. Consequently it will be necessary to develop new techniques that will result in jet noise reduction in the long term. This will entail a clearer and more thorough understanding of the source mechanisms and will evolve only if reliable methods for modelling these mechanisms can be developed.

The latest developments in computational fluid dynamics (CFD) provide information on the statistical character of the flow field and also on its instantaneous behaviour. This is used to build prediction techniques based on an understanding of the noise generation mechanisms. The focus of this present work therefore is to examine experimentally the relationship between turbulent structures in the jet and the associated noise generation mechanisms, as this has not received adequate attention to date.

The introductory sections of this thesis sets out to define the concept of Jet Noise. The techniques used to extract relevant information from jet flows are discussed in Chapter 3. Chapter 4 describes the preliminary analysis employed

in this regard. Finally, the experimental findings from the acoustic and combined velocity and acoustic measurements are presented in Chapters 5 & 6.

Chapter 2

Jet Noise

When jet engines were invented in the 1930s, the main design objective was to achieve the required thrust. This resulted in more powerful engines but at the expense of increased noise production. In the following decades this increased noise production was of major concern. However some experimental testing did exist to examine noise production. During the 1940s the experimental setup to predict noise generation was very primitive. Test beds were used to measure jet noise but it was not until open air tests were developed that measurements of the sound radiating away from jets became possible. These techniques lacked calibration and accuracy, and spectral analysis equipment rarely resolved more finely than the octave band. All that could be concluded from these tests was that 'big jets' were noisier than 'small jets', 'fast jets' were noisier than 'slow jets', and that the expansion ratios across the propulsive nozzle were important as were jet temperature and density. What was missing was an understanding of the physics involved before the experimental results could be interpreted properly. In this section an overview of the historical development of jet noise, commencing with the seminal work of Lighthill up to and including the most recent studies and methods currently being researched, are referred to.

2.1 Turbulent Shear Flows

An example of a free shear flow is the jet formed when fluid is continuously added to an otherwise stagnant fluid. The area separating the turbulent jet from the surrounding ambient flow is random in shape and continuously changing. The movement of this interface induces rotational fluid motion of the surrounding fluid.

Figure 2.1 illustrates the development of the jet. As fluid exits from the nozzle the flow of the high velocity fluid is fully aligned with the nozzle wall, and a core region of potential flow is formed (hence 'potential core'). Between the high velocity fluid exiting the nozzle and the surrounding fluid a shear layer is generated. Due to the addition of fluid from the surroundings (entrainment) this shear layer grows and develops and the amount of turbulent fluid increases in the downstream direction. This causes the jet to spread in the transversal

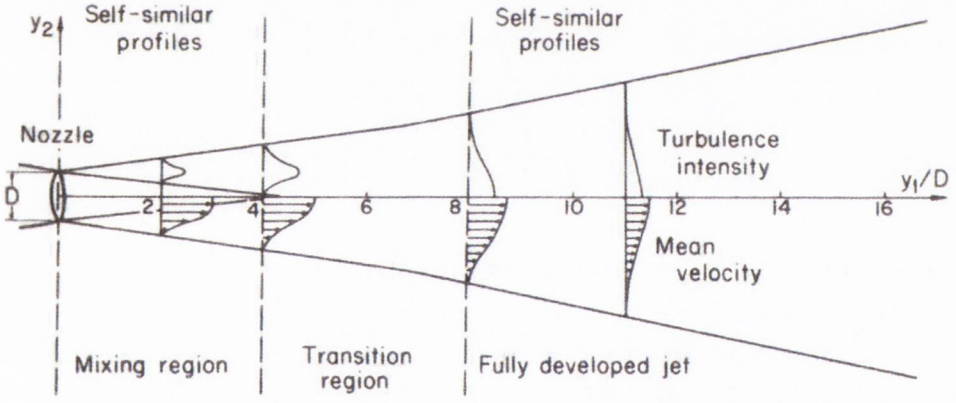

FIGURE 2.1: *Structure of a Jet (Ribner [3])*

direction. The radial extent of the potential core region decreases as the width of the shear layer increases, and more and more of the flow becomes turbulent. It is just downstream of the potential core closure that the jet is turbulent and thus fully developed. It is in this region, where the jet is fully turbulent, that most mixing occurs and hence where most noise originates, which is dependant on frequency.

Fully developed turbulence is a turbulence which is free to develop without imposed constraints. The possible constraints are boundaries, external forces, or viscosity. Implying that no real turbulent flow, can be fully developed in the large energetic scales, even at high Reynolds numbers. At smaller scales, turbulence will be fully developed if the viscosity does not play a direct role in the dynamics of these scales. However for theoretical purposes, when studying a freely-evolving statistically homogeneous turbulence, it is possible to assume that turbulence is fully developed in both the large and small scales.

Self-similar profiles are observed in this far field where the mean velocity profiles experience a linear growth of the jet width and a linear decay of the square of centerline velocity. The assumption that these self-similarity profiles are independent of initial conditions for all quantities and are therefore standard for all jets has been questioned by George [4]. The mean velocity profiles become self-preserving about 5 diameters downstream. Details of the turbulent structure can take much longer to become self-similar.

2.2 Sources of Noise

It was not until the 1950's when Lighthill [5] developed a general theory of aerodynamic sound generation, which became known as the Lighthill Acoustic Analogy Theory, that Jet Noise became a significant issue. In his theory, Lighthill proposed that the unsteady turbulent fluctuations which give rise to noise are replaced by a volume distribution of equivalent acoustic sources embedded in an otherwise uniform medium at rest. The propagation of sound in a uniform medium is governed by the equations

$$\frac{\partial \rho}{\partial t} + \frac{\partial}{\partial x_i}(\rho v_i) = 0 \qquad \frac{\partial}{\partial t}(\rho v_i) + a_0^2 \frac{\partial \rho}{\partial x_i} = 0 \qquad \frac{\partial^2 \rho}{\partial t^2} - a_0^2 \nabla^2 \rho = 0$$

where the first is the exact equation of continuity, the second is an approximate equation of momentum, and the third is obtained by eliminating the momentum density from the first two equations. Lighthill's idea was to change the compressible equations of motion into a form representing the propagation of acoustic

waves. The result is an inhomogeneous wave equation of the form:

$$\frac{\partial^2 \rho}{\partial t^2} - a_\infty^2 \nabla^2 \rho = \frac{\partial^2 T_{ij}}{\partial x_i \partial x_j} \tag{2.1}$$

where ρ is the density, a_∞^2 is the ambient sound speed, and

$$T_{ij} = \rho v_i v_j + (p - \rho a_\infty^2)\delta_{ij} + \tau_{ij} \tag{2.2}$$

is known as the Lighthill stress tensor, where v_i, p, and τ_{ij} are the velocity, pressure, and viscous tensor stresses and δ_{ij} is the Kronecker delta. The left hand side of equation 2.1 represents acoustic wave propagation and the right hand side the sources that generate the noise field. These source terms involve second spatial derivatives of the stress tensor and are referred to as quadrupoles, depicted in figure 2.2. Physically the quadrupole strength is equivalent to the

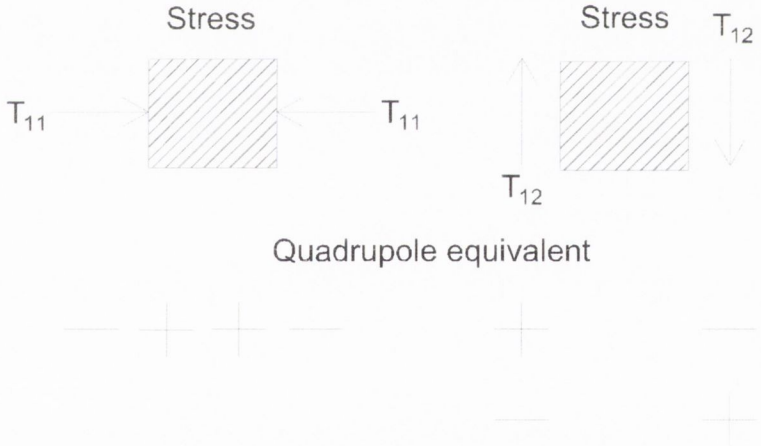

FIGURE 2.2: *Longitudinal and Lateral Quadrupoles*

applied stress to an element of fluid suffering from equal and opposite forces. Where each source of the applied stress is equivalent to a dipole and each such pair to a quadrupole. The auto correlation of the acoustic pressure, in terms of the correlation function of the Lighthill tensor is given by equation 2.3, where the Doppler correction factor (C_D) is applied.

$$I(x,\tau) = \frac{x_i x_j x_k x_l}{16\pi^2 c_0^5 \rho_0 |x|^6} \int\int_V \frac{1}{C_D^5} \frac{\partial^4}{\partial t^4} R_{ijkl}(y',\xi,t)\Big|_{t=\tau/C_D} dy'd\xi \qquad (2.3)$$

A very important result came from Lighthill's inhomogeneous wave equation. By using a Green's function for the wave equation, Lighthill established that the acoustic power radiated by a jet should vary as the eighth power of the jet velocity. This agreed with available experimental data and became known as the V_j^8 Law.

2.3 Turbulence structures

Knowledge of the characteristics of jet flows is essential to the understanding of Jet Noise since the sources of sound are defined by the turbulence structures. In the 1950's, turbulence was considered to be a random assortment of small eddies. As a consequence, the primary focus of jet noise investigation at that time was to quantify the noise generated from fine-scale turbulence, as reviewed by Tam [6]. Later Crow & Champagne [7], and Brown & Roshko [8] discovered independently the existence and importance of large-scale, as well as fine-scale structures within turbulence in jets and mixing layers. It was found that these large-scale structures were important noise sources for supersonic jets. However at that time their importance in subsonic jets was not established. It was not until 1998 that Tam [6] showed that both large and fine-scale structures are responsible for the noise that is generated in subsonic jets.

The instabilities which cause vortices to develop in the shear layer of a jet are known as Kelvin-Helmholtz instabilities. Due to secondary instabilities these vortices, as they move downstream, often evolve into three dimensional structures. Laufer [9] proposed that the principle of pairing of vortices was responsible for noise generation in jets. This pairing occurs in the shear layer, near the lip line of the jet, and is finished within one diameter downstream. However Hussain [10] showed that the break down and interaction of structures near the end of the potential core is in fact the region most responsible for noise generation in jets.

2.4 Noise Pattern

The sound generating structures or quadrupoles in jet flows are convected downstream by the mean flow, so that the sources are moving. Lighthill realised the importance that the source convection effect has on the directivity of jet noise, which is more obvious at higher jet velocity. Ffowcs-Williams [11] found that, by extending Lighthill's dimensional argument including the effect of source convection, for high speed jets the power of the radiated noise should vary as the third power of the jet velocity, i.e. $P \sim V_j^3$. Tam [6] and Ribner [12] showed that moving sources tend to radiate more sound in the direction of motion. When quadrupoles generate sound, in order to reach the far field, this sound must propagate through the jet flow. As the mean flow is highly non-uniform the sound is refracted as it travels outward from the jet flow resulting in less sound being radiated in the direction of the flow, as shown in figure 2.3. This effect creates a relatively quiet region surrounding the jet axis - known as the cone of silence (see figure 2.4). Atvars et al [13] demonstrated experimentally that the noise intensity drops by more than $20dB$ due to the presence of the cone of silence.

FIGURE 2.3: *Convection & Refraction*

Decomposing the turbulence velocity into mean and fluctuating components $v_i = U\delta_i + u_i$, where U is the local mean velocity and u_i the fluctuating component,

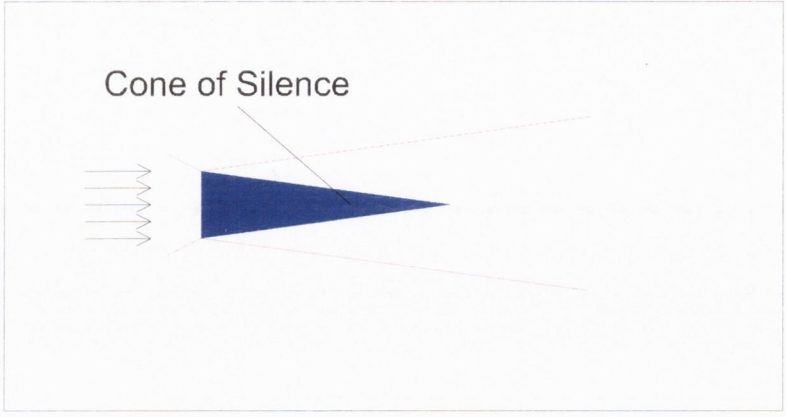

FIGURE 2.4: *Cone of Silence*

enables the quadrupole velocity correlations contributing to the generation of sound to be examined, as was shown by Ribner [12]. Source terms that contain only turbulent velocity components and that are independent of the mean flow are defined as *self noise*. Whereas terms that contain both turbulent velocity and mean flow components are known as *shear noise*. The self noise terms have the form: $\overline{u_i u_j u_k' u_l'}$ while the shear noise terms have the form: $U_1 U_1' \overline{u_i u_j'}$. The quadrupole correlation can be expressed as a function of the midpoint and the separation in space and time, as shown in figure 2.5. Ribner [12] analysed the potential contribution of the source terms and concluded that only nine of the thirty-six possible quadrupole correlations yield distinct contributions to the axisymmetric noise pattern of a round jet. The correlations contribute either $\cos^4\theta$, $\cos^2\theta\sin^2\theta$, or $\sin^4\theta$ directional patterns, where θ is the angle with the jet axis. He showed that the nine self-noise patterns combine as:

$$\begin{aligned} A\cos^4\theta(1) + A\cos^2\theta\sin^2\theta(\tfrac{7}{8}+\tfrac{7}{8}+\tfrac{1}{8}+\tfrac{1}{8}) + A\sin^4\theta(\tfrac{12}{32}+\tfrac{12}{32}+\tfrac{7}{32}+\tfrac{1}{32}) \\ = A(\cos^2\theta+\sin^2\theta)^2 = A \end{aligned} \tag{2.4}$$

and two shear-noise correlation patterns combine as:

$$(1)B\cos^4\theta + (\frac{1}{2})B\cos^2\theta\sin^2\theta = \frac{B}{2}(\cos^2\theta+\cos^4\theta) \tag{2.5}$$

The self noise is radiated equally in all directions whereas the shear noise gives a dipole like contribution. Therefore the overall 'basic' pattern is the addition

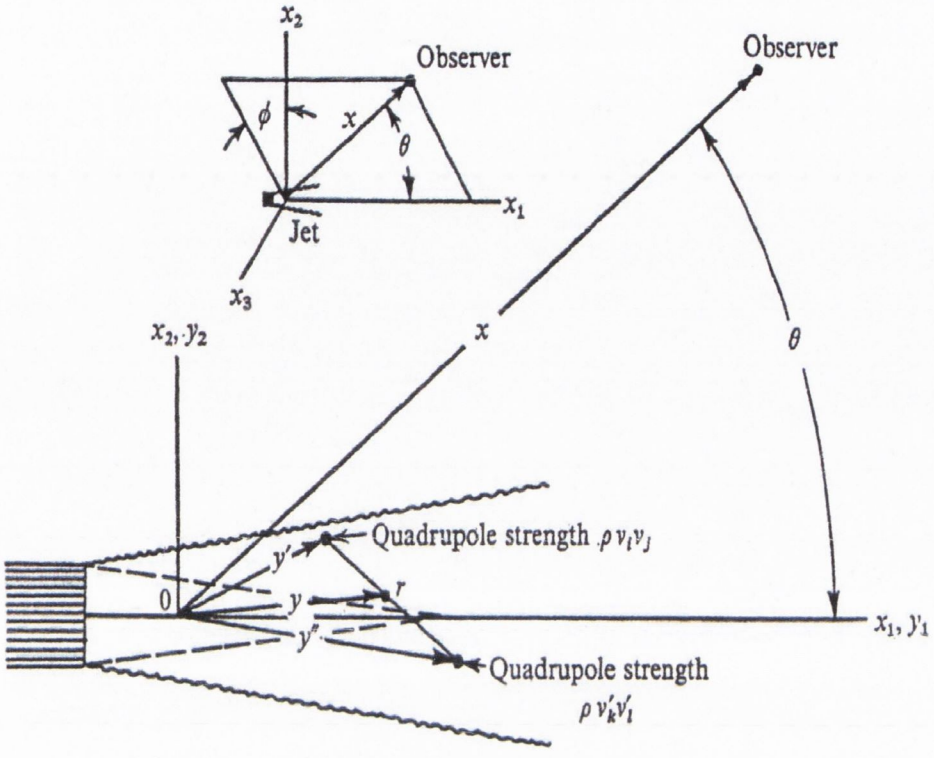

FIGURE 2.5: *Geometry for quadrupole correlations, (Ribner [12])*

of the self and shear noise terms, resulting in a form shown in equation 2.6 and illustrated in figure 2.6 as the basic pattern.

$$A + B(\cos^2\theta + \cos^4\theta)/2 \tag{2.6}$$

In addition to the basic pattern, the directional pattern of jet noise is dominated by convection and refraction. Figure 2.3 also shows the effect of convection on the sound waves, where it attempts to convect sound waves downstream into a broad fan enveloping the jet. Convection and refraction alter the basic noise pattern of a jet to the form shown in figure 2.6, where the resulting shape is a heart-shaped pattern of jet noise.

The correlation function is found to comprise a sum of second, third and fourth order velocity correlations as shown by Ribner. Of these, the radiat-

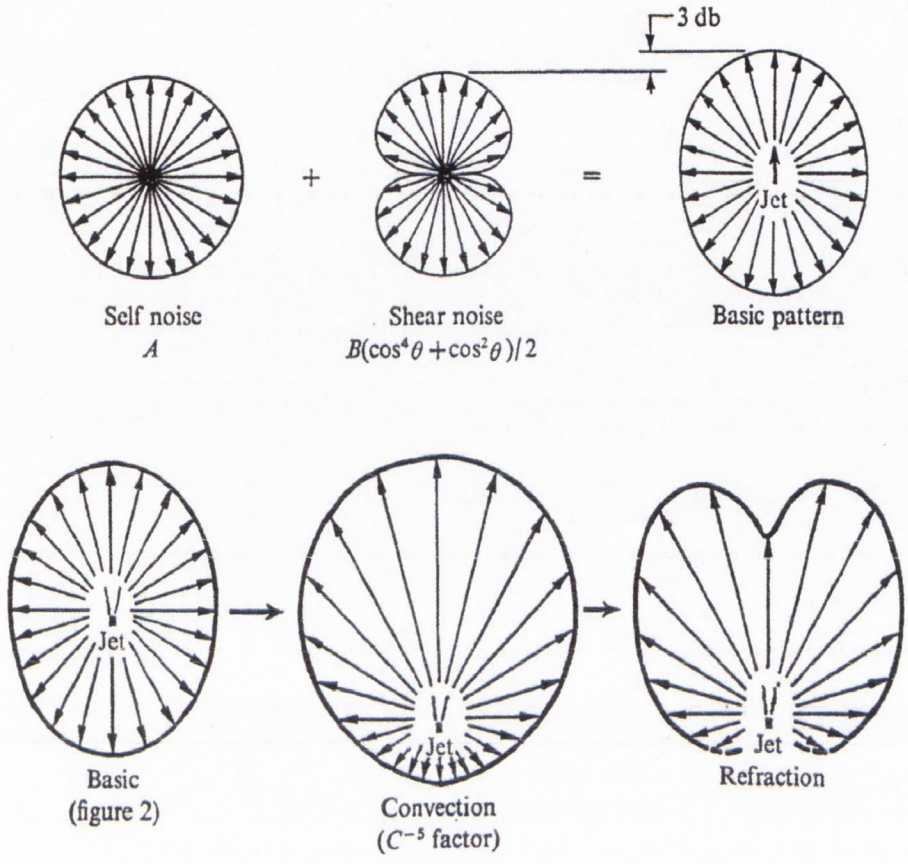

FIGURE 2.6: *Jet Noise Pattern (Ribner [12])*

ing quadrupoles are the fourth and second order terms, corresponding to self and shear noise mechanisms respectively. Through single and two-point turbulence velocity measurements an estimate of the quadrupole field structure can be achieved. Considering only a two dimensional slice through the jet the necessary required terms are: $\overline{u_1 u_1'}$, $\overline{u_2 u_2'}$, $\overline{u_1^2 u_1'^2}$, $\overline{u_2^2 u_2'^2}$, $\overline{u_1^2 u_2'^2}$, and $\overline{u_1 u_2 u_1' u_2'}$.

2.5 Recent Developments in Jet Noise Research

Throughout the 1980's the frequency content of jet noise was measured in 1/3 octave bands. However this technique artificially enhances the importance of the high frequency noise component, which complicated the physical interpretation of the measured data. Improvements in instrumentation and experimental facilities

in the following decade led to detailed analysis being carried out on the two components of turbulent mixing noise in supersonic jets.

Hussain [10] showed that large eddies evolve and interact in three ways. Firstly, structures form and convect downstream while growing in size. Secondly, when a fast moving structure catches up with a slower structure that is further downstream, they begin to rotate about a common point leading to 'pairing' of the two structures. Thirdly, individual structures have been observed to break down into two or more separate structures. The understanding of how these structures behave is important in the understanding of turbulence and hence jet noise.

Convection velocity is an important quantity in aeroacoustics since it can be used to establish the speed of moving sources within jets. The end of the potential core is where most of the turbulent mixing noise production occurs, as reported by, for example Tam [14] and Morrison et al [15]. Turbulent mixing noise has been shown to be highly directional within the acoustic far field, with peak noise emission at angles close to the jet axis. Using the correlation between the velocity fluctuations inside the jet and the far-field acoustic pressure the noise sources can be identified as originating from a particular region in the jet and their propagation speeds identified.

In irrotational flows, the relationship between pressure and velocity is described by the unsteady Bernoulli equation:

$$\frac{P - P_\infty}{\rho} = \frac{\partial \phi}{\partial t} - \frac{\bigtriangledown \phi \bigtriangledown \phi}{2} \tag{2.7}$$

where P_∞ is the pressure far from the flow and ϕ is the velocity potential. The pressure fluctuations associated with equation 2.7 can be divided into two parts. The first being the propagating or ***acoustic*** fluctuations which are usually in phase with the velocity fluctuations and secondly the non-propagating or ***hydrodynamic*** fluctuations that are 90 deg out of phase with the velocity. The acoustic fluctuations usually dominate the far field whereas the hydrodynamic fluctuations occur in the near field. Arndt et al [16] determined both analytically and experimentally that the demarcation between the hydrodynamic and

acoustic regions, dependant in a change of spectral roll-off from $kR^{-6.67}$ to kR^{-2}. Where k is the wavenumber which describes the spatial variation of waves, i.e. the phase change per unit distance ($= 2\pi f/c$) and R is the radial position relative to the shear layer axis. Arndt et al showed that a value of $kR = 2.0$ defined the demarcation with the hydrodynamic for $kR < 2.0$ and acoustic for $kR > 2$. Experimentally this implies that to achieve either the hydrodynamic or acoustic regions for a given frequency the measurement position needs to be carefully located, as shown in figure 2.7. This demarcation region, as examined by Jordan et al [17], identifies a coherence drop which results from a locally highly coherent mechanism.

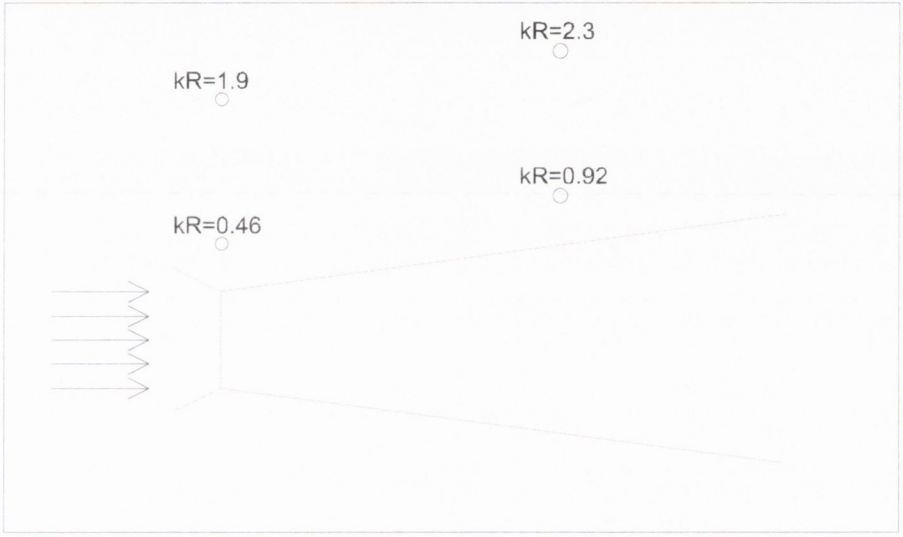

FIGURE 2.7: *kR demarcation at 1000Hz*

Hileman et al [18] concluded from an examination of the sound pressure signal, in the time domain, and from the associated spectra that different mechanisms of noise production are present within a jet. They observed large amplitude sound pressure peaks interspersed among quiet periods, where the jet did not produce any large amplitude noise. The quiet periods lasting over one millisecond, are equivalent to large structures travelling over seven jet diameters. This led Hileman et al. to suggest that there are distinct events within the jet that are producing the largest amplitude noise.

2.6 Modelling & Prediction of Jet Noise

In order to estimate aerodynamic source terms for jet noise prediction in subsonic jets Lighthill [19] suggested that his Acoustic Analogy Theory should be used in conjunction with Computational Fluid Dynamics (CFD) methods.

2.6.1 Aerodynamics

The first step towards jet noise reduction is to improve prediction techniques using the most recent CFD models. The processes of sound generation and propagation to the far field for a real jet flow is completely governed by the compressible Navier-Stokes equations which can be investigated by direct numerical simulation methods. New techniques can only be developed when a better understanding of the source mechanisms of jet noise is achieved. These new techniques will subsequently require validation using reliable methods for modelling the source mechanisms. The simulation of the flow that generates sound requires a time dependent solution of the Navier-Stokes equation. The numerical solution of the turbulent Navier Stokes equations can be achieved using a number of approaches. These include Reynolds Averaged Navier Stokes (RANS), Direct Numerical Simulation (DNS), and Large Eddy Simulation (LES). Each method involves approximations and simplifications.

The most common procedures are Reynolds Averaged Navier Stokes where the statistical characteristics of the turbulence are determined using turbulence closure models. These results can then be used as input for aeroacoustic source modelling and propagation. In a Reynolds-averaged approach, the turbulent flow is averaged and solved. Statistics based on previous experimental data are then used to model the fluctuating effects of the turbulent motions greatly reducing the computational requirements. But RANS lacks the necessary information required on spatial correlations and is therefore not accurate enough on its own to deal with flow separation and noise generation. Self [20] for example has defined a source model which incorporated the frequency dependance of the moving-axis timescale.

Alternative methods to solve the Navier Stokes equations include Direct Numerical Simulation and Large Eddy Simulation. Both have the capacity to compute the unsteady aerodynamic and acoustic (near and far) fields. DNS is the most precise way to model the physics involved in turbulent mixing. However, this involves solving even the smallest turbulent motions in a flow and thus makes it very computationally intensive, and is therefore, currently restricted to very low Reynolds number flows in jets (< 1000).

LES is a more recent approach to turbulence modelling and is an intermediate step between DNS and RANS. In this approach a filter is used to separate the large turbulent motions from the smaller ones. Since large scale motions are more significant, they are solved. Subgrid scale (SGS) models are then used to model the interactions that would have otherwise occurred between the large and small eddies. Although large eddy simulation requires much less computing power than the DNS approach, it requires more computational time than that of a Reynold's averaged solution, but achieves more accurate results. This technique has been used to resolve the turbulent scales in shear layers at high Reynolds numbers. For noise prediction LES combined with other techniques has been applied to circular jets and has proved very promising, for example, by Bogey et al [21] and Andersson et al [22]. Recently LES and RANS have been combined to produce a hybrid LES/RANS, as shown by, for example, Spalart [23] and Shur et al [24]. An alternate approach to the grid based techniques, i.e. RANS, LES, DNS, is the Vortex Filament Method which is based on modelling the dynamics of discrete vortex tubes.

2.6.2 Source and Propagation Predictions

When the convection velocity of large turbulent structures is supersonic, Tam & Aurialt [25] determined that the most important factor is the radiation of instability waves, whereas for high Reynolds number subsonic flows, the fine scale turbulence is the main source of noise. They also showed that that the Linearized Euler Equations (LEE) can provide good predictions for far field noise. The Stochastic Noise Generation and Radiation (SNGR) model, as proposed by

Bailly et al [26] [27], generates unsteady pressure for noise source terms by using RANS solutions combined with the turbulent velocity field which is estimated from a sum of random Fourier modes. This is then combined with either LEE or an acoustic propagation model.

The more widely used approach is 'classical' acoustic propagation modelling which is based on Green's functions and Kirchhoff methods. To model acoustic propagation the most recent studies, for example Bogey et al [21] and Bailly & Juve [28], have focused on the combination of LEE and LES, where some success has been seen for simple jet flows. An advantage of this approach is that LEE does not require as much computational power and LES could provide the necessary requirements to accurately capture the noise generating turbulent structures. However due to refraction effects being neglected and simplified descriptions of the turbulent correlations the spectral predictions can be unsatisfactory.

Self [29] for example, has examined the Fourier Transform equation of the two-point correlation of the Proudmann stress equation. When the Fourier Transform is known throughout the jet then the far field noise spectrum can be calculated. His aim was to develop a jet model that uses RANS data as input, but it may not be practical to provide the quantity of data that would be required to calculate the far field spectrum. Instead the approach taken is to model a functional form for $R(y, \eta, \omega)$ which is consistent with what is known experimentally. Despite all of this extensive knowledge and work the direct estimation of aerodynamic noise sources in turbulent flows is still very limited to low Reynolds number flows.

2.7 Summary

The Lighthill Acoustic Analogy in 1952 provided the starting point for the understanding of the physics responsible for jet noise production. In the following years it was determined that both large and small scale structures were important in the jet noise investigation and, the correlation between the velocity fluctuations in the jet and the far field acoustic pressure enables the noise sources to be identified. In order to obtain a significant reduction of jet noise reliable predic-

tion methods accounting for all phenomena responsible for sound generation and propagation are required.

Existing prediction techniques as discussed are still very limited. RANS technique can be linked to aeroacoustic source modelling. The Navier Stokes equations can be solved using DNS, but this is limited to very low Reynolds numbers, or LES, which is currently limited to simple geometries but shows promise for development. For these and future techniques to have the ability to predict the acoustic performance, for say novel geometries, they will rely heavily on extensive validation from experimental measurements. Currently, measurements can provide information such as potential core length, turbulence intensities and spatio-temporal correlations. In order for future modelling and prediction to be tested and validated, experimental findings will need to provide information concerning how the noise source terms behave in and around the jet. In this thesis, techniques are developed to achieve this objective.

Chapter 3

LDA Processing Techniques

It has been shown that the important statistical properties of coherence, phase, convection velocities and length and time scales can be derived from the auto and cross spectra, as shown by for example Kerhervé et al [30]. LDA systems provide a non-intrusive study of flows, for example, and provide the necessary data to estimate spectra.

Obtaining the auto and cross spectrum using a Laser Doppler Anemometer is complicated by the intermittent nature by which data is acquired from the random passing of particles through the measuring volume. A number of techniques are available for computing the auto spectrum from LDA measurements. The limiting factor for all methods is the average sample rate of the data and the number of data points in each sample, as these influence the maximum and minimum frequencies that can be resolved.

The most straight forward technique for dealing with the LDA random acquisition is the Sample & Hold time domain reconstruction procedure, whilst the most common alternative method is the Slot Correlation technique proposed by Gaster & Roberts [31]. Various comparisons have been made of the different methods used to determine the auto spectrum from LDA data by, for example, Buchave et al [32], Lee & Sung [33], Britz & Antonio [34] and Benedict et al [35], but no particular technique has proved superior although Slot Correlation is widely used.

3.1 Sample & Hold

The ***Zeroth-Order Interpolation*** or ***Sample and Hold method***, as illustrated by Figure 3.1, has been well analyzed in terms of spectral content (Adrian & Yao [36]) and in terms of moments (Edwards & Jensen [37]). The inherent

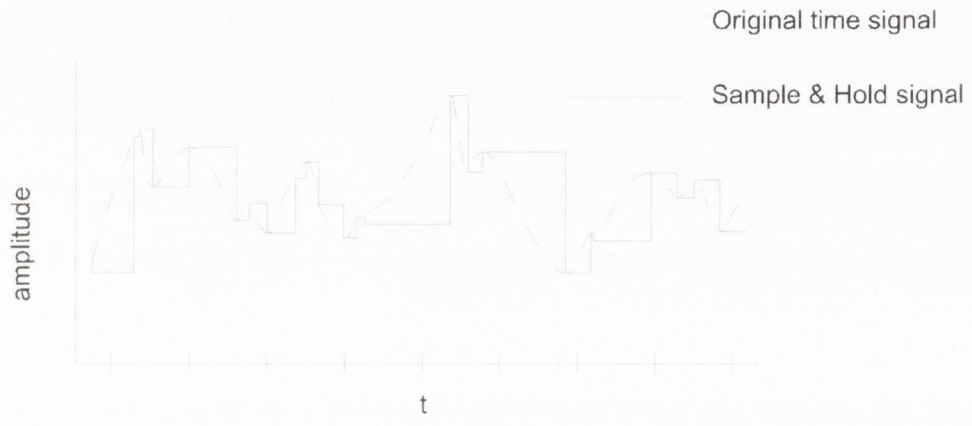

FIGURE 3.1: *Sample & Hold: Re-sampling a random acquired LDA signal at equal time intervals*

errors associated with Sample & Hold have been detailed by Adrain & Yao [36] and Boyer & Searby [38]. They consist of a step noise, which adds a constant bias to the estimated spectrum, and a low pass filter effect. These errors were shown to be functions of the mean sample rate and the maximum frequency to be resolved. Adrian & Yao determined that by using the autocorrelation function, an expression can be derived for the expectation of the power spectral density, as given by equation 3.1.

$$S_{u_m}(\omega) = \underbrace{\frac{1}{1+(2\pi f)^2/f_m^2}}_{\text{filter}} \left(S_u(\omega) + \underbrace{\frac{2\sigma_u^2}{f_m^3 T_\lambda^2}}_{\text{step noise}} \right) \tag{3.1}$$

where $S_{u_m}(\omega)$ is the Sample & Hold spectrum, $S_u(\omega)$ is the true spectrum, f_m is the mean data rate, T_λ is the Taylor micro-scale and σ^2 is the variance. The second term in the parentheses is termed step noise and corresponds to the spec-

tral contribution necessary to account for the step-like jumps in a Sample & Hold signal. The term in front of the parentheses, which affects both the true spectrum and the step noise, is a first-order low-pass filter with cut-off frequency $f_m/(2\pi)$. By comparing the effect of data rates Adrian & Yao concluded that spectra are only reliable up to a frequency of $f_m/(2\pi)$, which substitutes the Nyquist frequency rule for regularly sampled data. In order to improve this limit correction procedures proposed by Nobach et al [39] and Simon & Fitzpatrick [40] have resulted in reliable spectra up to $f_m/2$.

Simon & Fitzpatrick [40] illustrated the estimation of the auto-spectrum of a random LDA signal $u(t)$ by Sample & Hold, as shown in figure 3.2. Here the

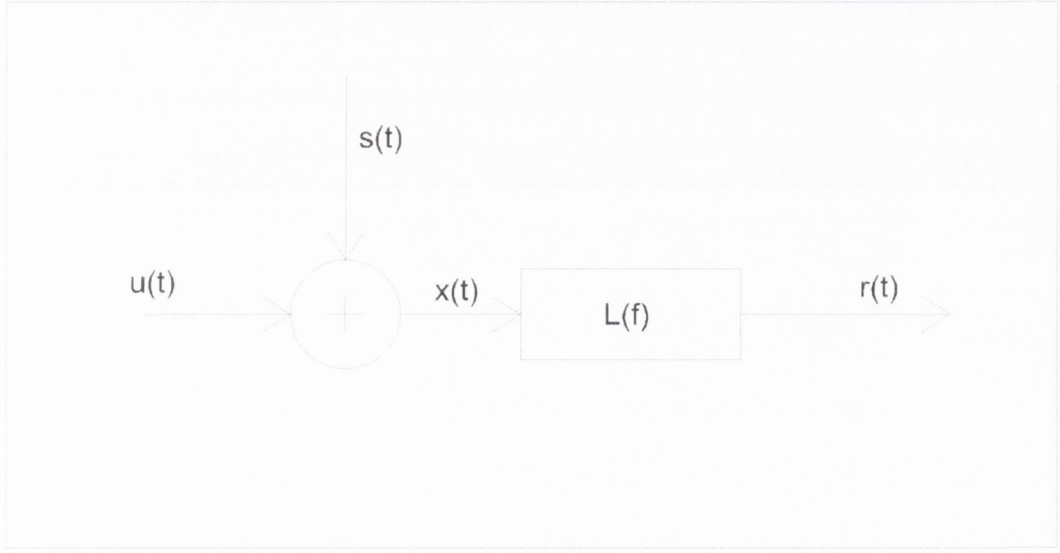

FIGURE 3.2: *Schematic of the Sample & Hold Procedure*

step noise is represented by $s(t)$ and the low pass filter effect by $L(f)$ so that $r(t)$ is the reconstructed signal. The relationships are as follows:

$$G_{xx}(f) = G_{uu}(f) + G_{ss}(f) \tag{3.2}$$

where G_{uu} corresponds to the one-sided true spectrum, G_{xx} to the one-sided filter corrected Sample & Hold spectrum, and G_{ss} to the step noise estimate.

$$G_{rr}(f) = |L(f)|^2 G_{xx}(f) \tag{3.3}$$

If the characteristics of the low pass filter are known and if the step noise can be estimated, then the calculated spectrum $G_{rr}(f)$ can be corrected to obtain the true spectrum $G_{uu}(f)$. Simon & Fitzpatrick [40] showed that the use of the continuous filter proposed by Adrian & Yao in 1987, (equation 3.4), was incorrect and proposed a discrete filter, given by equation 3.5. The continuous filter is a function of the mean data rate f_m, whereas the new discrete filter is a function of both the mean data rate and the re-sample rate f_r. The difference in a filter corrected signal when using a discrete and continuous filter will be examined in chapter 4.

$$|L_c(f)|^2 = \frac{1}{1 + (2\pi f / f_m)^2} \tag{3.4}$$

$$|L_d(f)|^2 = \frac{f_m}{2f_r}\left(\frac{1 - e^{-2f_m/f_r}}{1 - 2\cos(2\pi f dt)e^{-f_m/f_r} + e^{-2f_m/f_r}}\right) \tag{3.5}$$

It is possible to estimate the step noise, but the actual form of the spectrum needs to be known and this is impossible in most practical cases. However as the step noise spectrum is white it can be estimated using the variances as follows:

1. The variance of the turbulent velocity, $u(t)$ can be determined from the original time domain data as:

$$\sigma_u^2 = \frac{1}{N}\sum u^2 \tag{3.6}$$

   This has been shown (Simon et al [40]) to be equal to the variance of the reconstructed signal σ_r^2.

2. The variance of the reconstructed signal corrected for the low pass filter effect can be determined from the auto-spectrum as:

$$\sigma_x^2 = \frac{1}{N}\sum \frac{G_{rr}(f)}{|L(f)|^2} \tag{3.7}$$

   From figure 3.2, this is equal to the variance of the original signal plus the step noise, so that the variance of the step noise can be found from:

$$\sigma_s^2 = \sigma_x^2 - \sigma_u^2 \tag{3.8}$$

and,

3. Since the step noise is white its spectrum over N points is a constant given by:

$$G_{ss}(f) = \frac{1}{N}\left(\sum \frac{G_{rr}(f)}{|L(f)|^2} - \sum u(t)^2\right) \tag{3.9}$$

Once the step noise is quantified an estimated spectrum $G_{ee}(f)$ can be found by subtracting the step noise spectrum from the filter corrected spectrum.

$$G_{ee}(f) = \frac{G_{rr}(f)}{|L(f)|^2} - G_{ss} \tag{3.10}$$

An LDA signal acquired with either a low or high acquisition data rate is re-sampled ($G_{rr}(f)$) at approximately ten times the data rate. This is to avoid any high frequency contamination. However this does not imply that frequencies above the mean data rate can be accurately interpreted from the spectrum ($G_{ee}(f)$).

Now that the auto spectra has been corrected for the errors that are associated with the Sample & Hold reconstruction procedure, it is necessary to determine how the cross spectra is estimated. There are two conditions under which cross spectra are to be found from two LDA measurements, coincident and non-coincident.

3.1.1 Non-coincident LDA Signals

Consider the schematic shown in figure 3.3 where two signals (subscripts 1 & 2) are acquired in non-coincident mode (i.e that each signal acquired is independent, with its own acquisition time and data rate). The cross spectrum can be defined as:

$$G_{x_1x_2}(f) = \langle X_1^*(f)X_2(f)\rangle = \langle\{U_1^*(f) + S_1^*(f)\}\{U_2(f) + S_2(f)\}\rangle \tag{3.11}$$

where a capital letter (namely X, U and S) denotes a Fourier transform and $*$ its conjugate. As these two signals are acquired in non-coincident mode the step noise contaminations ($s_1(t)$ & $s_2(t)$) can be considered to be uncorrelated with

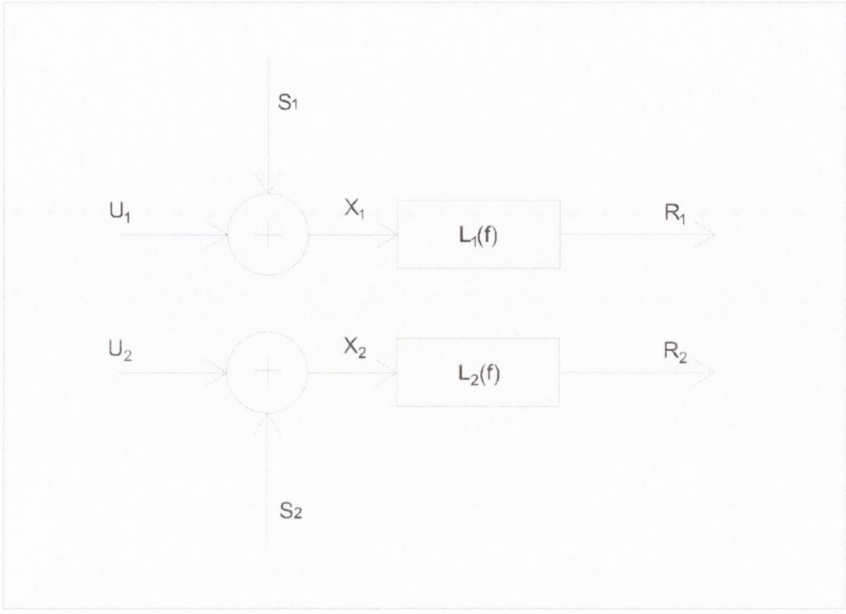

FIGURE 3.3: *Schematic of Two LDA signals*

each other, and also with $u_1(t)$ and $u_2(t)$, so that the estimated cross spectrum can be simplified to become:

$$G_{e_1e_2}(f) = G_{x_1x_2}(f) \tag{3.12}$$

Obviously, some of the data will be acquired coincidentally, but this is only likely at the lower frequencies. The estimated cross spectrum between two LDA signals acquired in non-coincident mode is simply the filter corrected cross spectrum. The coherence between the two signals can then be written as:

$$\gamma^2_{x_1x_2}(f) = \frac{G^*_{x_1x_2}(f)G_{x_1x_2}(f)}{[G_{u_1u_1}(f) + G_{s_1s_1}(f)][G_{u_2u_2}(f) + G_{s_2s_2}(f)]} \tag{3.13}$$

From this the actual coherence (as defined by Fitzpatrick & Simon [41]) can be estimated from:

$$\gamma_{e_1e_2}(f) = \gamma^2_{x_1x_2}(f)[1 + \alpha_1(f)][1 + \alpha_2(f)] \tag{3.14}$$

where $\alpha_1(f) = G_{s_1s_1}(f)/G_{e_1e_1}(f)$ and $\alpha_2(f) = G_{s_2s_2}(f)/G_{e_2e_2}(f)$ are the noise to signal ratios that ultimately determine how effective estimates can be. When the noise to signal ratio becomes saturated obviously the corrected estimates of coherence will be unrealistic.

3.1.2 Coincident LDA Signals

However if the LDA signals in figure 3.3 are acquired in coincident mode (i.e. a data point is only validated if it is registered by both measurement points simultaneously) the correction procedure is somewhat different. Both signals will use the same filter correction, as the data rate is constant between the two channels. However the step noise contamination will affect the cross spectrum. If the reconstructed data is filter corrected, then the cross spectrum is

$$\begin{aligned} G_{x_1x_2}(f) &=< X_1^*(f)X_2(f) > \\ &=< \{U_1^*(f) + S_1^*(f)\}\{U_2(f) + S_2(f)\} > \\ &= U_1^*(f)U_2(f) + U_1^*(f)S_2(f) + S_1^*(f)U_2(f) + S_1^*(f)S_2(f) \end{aligned} \tag{3.15}$$

In this case the step noise sources S_1 and S_2 are not identical due to the different variance of two signals and cannot be eliminated. Therefore the cross spectrum will be contaminated by step noise. The issue now is how to estimate this step noise $G_{s_1s_2}$ and correct the cross spectrum, in the equation 3.16.

$$G_{x_1x_2}(f) = G_{u_1u_2}(f) + G_{s_1s_2}(f) \tag{3.16}$$

The method proposed to correct the coincident data and ultimately determine the actual coherence is as follows:

1. The estimate of the step noise that contaminates the coincident cross spectrum, in equation 3.16, is determined by using the same procedure that was implemented on the auto spectra (non-coincident & coincident). In other words, the step noise $G_{s_1s_2}$ will be defined as:

$$G_{s_1s_2}(f) = \frac{1}{N}\left(\sum_{i=1}^{N} G_{x_1x_2} - \sum_{i=1}^{N} G_{r_1r_2}\right) \tag{3.17}$$

2. When $G_{s_1s_2}$ is inserted into equation 3.16 it yields the Sample and Hold estimate of the cross spectrum between two coincident LDA signals. The

uncorrected coherence $\gamma^2_{x_1x_2}(f)$ is calculated using equation 3.13. However, the corrected coherence estimate from coincident data is different from the non-coincident form and needs to be defined. This difference arises due to the step noise contamination of the cross spectrum.

3. The estimated coherence from two coincident LDA signals is given by equation 3.18 where all terms are a function of frequency. $\alpha_1(f)$ and $\alpha_2(f)$ are the noise to signal ratios previously defined, $G_{s_1s_2}$ is the step noise estimate that is applied to the cross spectrum, $G_{x_1x_2}(f)$ is the filter corrected cross spectrum and $G_{e_1e_1}(f)$ & $G_{e_2e_2}(f)$ are the estimated auto spectra that have been filter and step noise corrected.

$$\gamma^2_{e_1e_2}(f) = \gamma^2_{x_1x_2}(1+\alpha_1)(1+\alpha_2)+\frac{|G_{s_1s_2}|^2 - G^*_{x_1x_2}G_{s_1s_2} - G_{x_1x_2}G^*_{s_1s_2}}{G_{e_1e_1}G_{e_2e_2}} \quad (3.18)$$

3.1.3 One LDA Signal & a Conventional Instrument

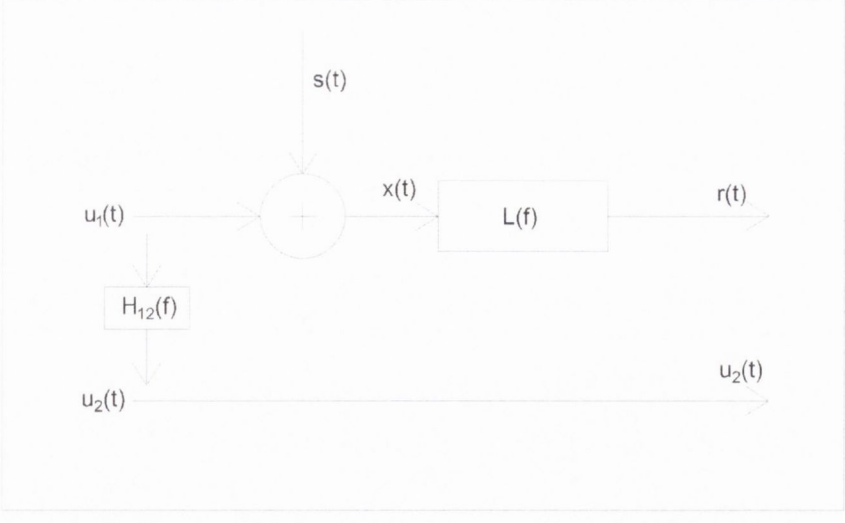

FIGURE 3.4: *Schematic of an LDA signal and a conventional instrument (e.g. hot-wire or microphone)*

One other configuration exists for an LDA signal, which is illustrated in figure 3.4. This schematic shows a Sample & Hold reconstructed signal with a conventional instrument sampled independently. As with non-coincident data the step

noise contamination does not affect the cross spectrum. Therefore the estimated cross spectrum between the LDA signal and a convectional instrument can be simply defined as:

$$G_{eu_2}(f) = G_{xu_2}(f) \tag{3.19}$$

where the LDA signal has been filter corrected. The uncorrected coherence is calculated from equation 3.20 where $G_{xu_2}(f)$ is the cross spectrum with the LDA signal filter corrected, $G_{xx}(f)$ is the filter corrected LDA auto spectrum and $G_{u_2u_2}(f)$ is simply the auto spectrum of the convectional instrument. The actual coherence (defined by Fitzpatrick & Simon [41]) between an LDA signal and a convectional instrument sampled independently is defined by equation 3.21, where α_1 is the noise to signal ratio.

$$\gamma^2_{xu_2}(f) = \frac{|G_{xu_2}(f)|^2}{G_{xx}(f)G_{u_2u_2}(f)} \tag{3.20}$$

$$\gamma^2_{eu_2}(f) = \gamma^2_{xu_2}(f)(1 + \alpha_1(f)) \tag{3.21}$$

In the three configurations of LDA processing (i.e. non-coincident, coincident modes and with a conventional instrument) the coherence corrections associated with Sample & Hold are influenced by the noise to signal ratio. It will be shown, using experimental data, in later chapters how this parameter will be the key to frequency limits.

3.2 Slot Correlation

The Slot Correlation technique was introduced by Mayo et al [42] and Gaster & Roberts [31] as a means of estimating the autocorrelation function of the flow velocity fluctuations from randomly sampled LDA data. The velocity product of all sample pairs with time separations falling within a given bin width is added to the bin's sum as another estimation of the autocorrelation function for that time lag. After processing all sample pairs, each bin is divided by the number of accumulated products. This can be written as:

$$\hat{R}_k = \hat{R}(k\Delta\tau) = \frac{\sum_{i=1}^{N}\sum_{j=1}^{N} u_i u_j b_k(t_j - t_i)}{\sum_{i=1}^{N}\sum_{j=1}^{N} b_k(t_j - t_i)} \tag{3.22}$$

The cross-product is plotted as a function of the associated time lags, which gives an estimation of the autocorrelation function which is then windowed and Fourier transformed to result in an estimation of the power spectral density of the signal. A one-sided power spectral density is formed by taking the discrete cosine transform, mathematically shown as:

$$\hat{S}_j = \hat{S}(f_j) = \hat{S}(\frac{j}{2K\Delta\tau}) = 2\Delta\tau\Big(\hat{R}_0 + 2\sum_{k=1}^{K-1}\hat{R}_k \cos(\pi f_j k\Delta\tau) + (-1)^j \hat{R}_K\Big) \tag{3.23}$$

where K is the index of the maximum time lag of the auto correlation function.

Due to limited accuracy of the particle velocity estimation the self-products lead to an estimate of the velocity variance that is too large and a biased power spectral density estimate. Hence a limitation of the standard slotting technique is its high variance which results in poor estimates of turbulence spectra. Van Maanen & Tummers [43] reduced the high variance that results from the slotting technique by using an auto-correlation function normalized by a variance estimate particular to each slot, called the local normalization. Another approach to reduce the high variance was proposed by Nobach et al [39], which was called the fuzzy slotting technique. This operation defined as:

$$\hat{R}_k = \Big[\sum_{i=1}^{N}\sum_{j=1}^{N} u_i u_j b_k(t_j - t_i)\Big]\Big\{\Big[\sum_{i=1}^{N}\sum_{j=1}^{N} u_i^2 b_k(t_j - t_i)\Big]\Big[\sum_{i=1}^{N}\sum_{j=1}^{N} u_j^2 b_k(t_j - t_i)\Big]\Big\}^{-1/2} \tag{3.24}$$

where $\hat{R}_k$ is the autocorrelation function estimate for slot k, N is the number of data points in the signal, b_k is the triangular windowing function used to perform the "fuzzy" operation, defined as

$$b_k(t_j - t_i) = \begin{cases} 1 - |(t_j - t_i)/\Delta\tau - k| & \text{for } 1 - |(t_j - t_i)/\Delta\tau - k| < 1 \\ 0 & \text{otherwise} \end{cases}$$

with τ the slot width.

Nobach et al [39] used a lag product weighting scheme instead of the top-hat function in the original algorithm. This proved a more accurate technique as it enabled the lag products to contribute to two slots at the same time and weights lag products that lie close to the slot centers more heavily, as illustrated in Figure 3.5. The slotting results that will be presented in later chapters were calculated using the 'Fuzzy Slotting' approach.

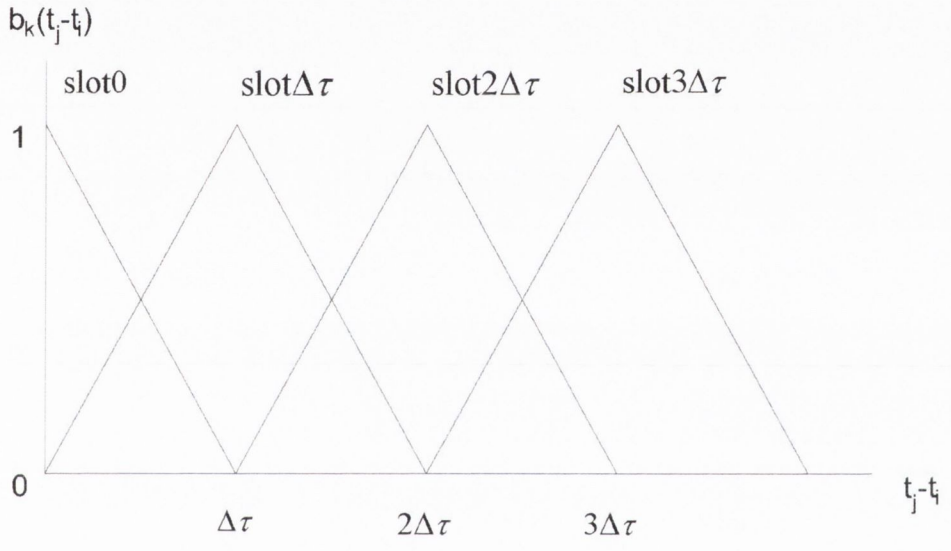

FIGURE 3.5: *The weighting scheme of the fuzzy slotting technique*

Slot Correlation has been used in the past for many applications. Benchmark tests were performed using numerous methods including slot correlation and Sample & Hold, Benedict et al [35]. Two distinct data sets were examined, namely band-limited random noise and Pao-like spectrum. It was shown that of the algorithms examined the fuzzy slotting technique and the refined reconstruction technique were superior. Benedict et al. [44] examined the fuzzy slotting technique using local normalisation (proposed by van Maanen et al [45]) and compared this to a refined Sample & Hold technique (proposed by Nobach et al [39]). The refined Sample & Hold technique incorporates an inverse particle-rate filter, which simply removes the mean velocity and large-scale fluctuations from the data, to improve the pre-estimate. It was found that both techniques estimate

very similar results even at low data rates.

3.3 Concluding Remarks

The random data acquisition that arises from LDA systems requires a specific type of processing. The two most common techniques used are Sample & Hold and Slot Correlation. In this section the correction procedures associated with Sample & Hold were defined for four acquisitions types:

1. Single component LDA signal (Simon & Fitzpatrick [40])
2. Non-coincident LDA signals (Fitzpatrick & Simon [41])
3. Coincident LDA signals
4. One LDA signal with a convectional instrument (Fitzpatrick & Simon [41])

Also defined is the 'Fuzzy' Slotting technique (Nobach et al [39]). The main differences between these two techniques is their approach to estimate spectra. Sample & Hold directly estimates the frequency domain from the time domain, whereas Slot Correlation must perform a Fast Fourier Transform to determine the frequency domain from the initially estimated correlation domain.

Chapter 4

Preliminary Analysis of LDA Data

The analysis procedures derived are now applied to real data. In the first instance, the correction procedure for Sample & Hold reconstruction is examined. Then a comparison is made between the signal processing techniques of Sample & Hold and Slot Correlation. This comparison includes auto and cross spectra, coherence and phase, and correlation curves. Finally the different modes of LDA acquisition that exist and the consequences on velocity fluctuations and the Reynolds stress terms are examined.

4.1 Sample & Hold Analysis

The mathematical corrections associated with Sample & Hold were covered in chapter 3, where it was shown that two different filters have been used; a continuous filter, (equation 3.4), proposed by Adrian & Yao [36] and a discrete filter, (equation 3.5), proposed by Simon & Fitzpatrick [40].

When the filter correction is applied to the raw Sample & Hold spectrum ($G_{rr}(f)$) of experimental data, the differences between the two filters, as shown in figure 4.1 can be seen. In the case of the continuous filter, it can be seen that the step noise estimate is greater than the continuous filter corrected spectrum. When the step noise is subtracted from the filter corrected spectrum, the estimated

spectrum will be negative at frequencies above approximately $4kHz$. However

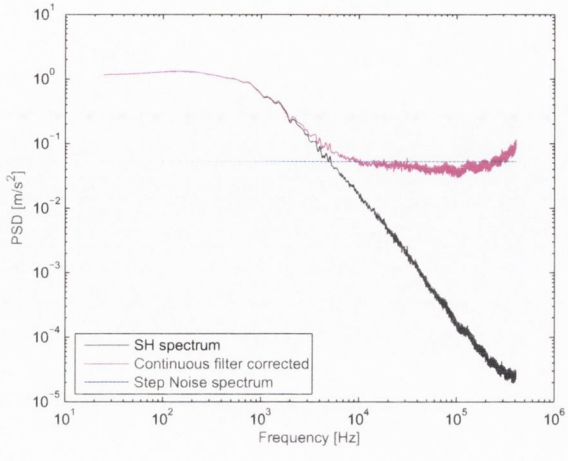

(a)

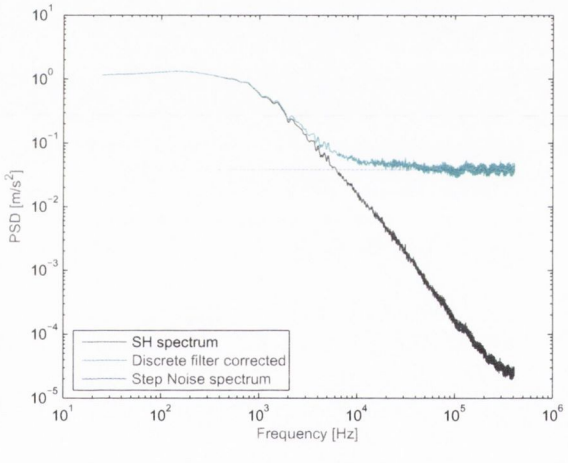

(b)

FIGURE 4.1: *Sample & Hold Filters applied on JEAN Jet 3 data (a) Continuous (see equation 3.4) (b) Discrete (see equation 3.5))*

when the discrete filter is used, the filter corrected spectrum approaches the step noise. Therefore any negative spectral values will occur at higher frequencies. For this reason the filter employed will be the discrete filter of Simon & Fitzpatrick (2004).

Now that the filter selection has been verified the remainder of the correction procedure associated with Sample & Hold, as detailed in chapter 3, can be il-

lustrated. Figure 4.2 represents the auto spectra for u' where the final corrected (filter and step noise corrected) spectrum is shown in green, denoted $G_{ee}(f)$ in equation 3.10. The limiting factor of spectral estimates is not solely dependent on the data rates as the Noise to Signal ratio (α) plays a significant role. Figure

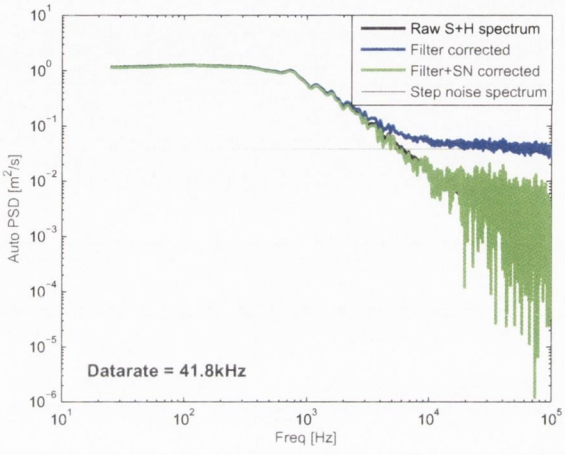

FIGURE 4.2: *Auto Spectral estimation illustrating the Sample & Hold corrections applied on JEAN Jet 3 data*

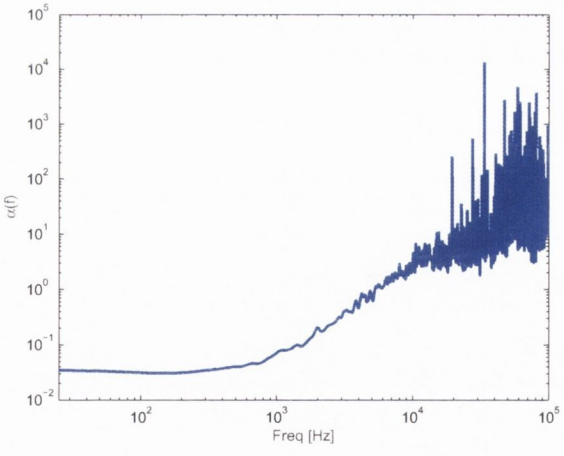

FIGURE 4.3: *Noise to Signal Ratio estimated from JEAN Jet 3 data*

4.3 illustrates the noise to signal ratio corresponding to the auto spectrum of figure 4.2. The frequency that corresponds to the noise to signal ratio reaching a value of approximately 10 appears to indicate the upper limit of the spectral estimate. This is considerably less than the value of 50 obtained by Fitzpatrick et

al [41], but their data was simulated. The additional noise associated with real measurements has reduced this limit. It will be shown in the next section how this noise to signal limit is also evident in the cross spectral estimates and the phase. In this example, the upper frequency limit is approximately $20kHz$, which corresponds to half the data rate of the acquisition ($f_m/2$). This is a considerable improvement on the Adrian & Yao [36] resolution of $f_m/(2\pi)$.

4.2 Comparison of Processing Techniques

To ensure that the modified Sample & Hold technique performs efficiently a comparison with Slot Correlation is now examined. This approach has already been mathematically defined in chapter 3. The most obvious difference between the two techniques is the path they take to estimate a spectrum from random data. The Sample & Hold technique estimates the frequency domain directly from the time data, whereas the Slot Correlation requires a Fourier transform to obtain the frequency domain from the initially estimated correlation domain. Since both techniques approach random data from opposite ends it will therefore be inevitable that some discrepancies will exist. However it is the aim of this section to validate the Sample & Hold procedure.

4.2.1 Measurements

The data presented in this section was acquired under the European 'JEAN' (**J**et **E**xhaust **A**erodynamic **N**oise) contract. The objectives of the JEAN project were

1. the assessment of efficient flow solvers for aeroacoustic applications
2. interfacing these to update classical and novel source & propagation models
3. use of new signal processing techniques for turbulence/acoustic measurements
4. prediction methodologies for jet noise applications.

The experimental measurements under this contract were performed on a subsonic jet at the MARTEL facility of CEAT (Centre d'Etudes Aerodynamiques et Thermiques) in Poitiers, France.

Acoustic and aerodynamic measurements were performed using a 50-mm diameter nozzle (figure 4.4) operating at temperatures and velocities as shown in table 4.1. The jet was aligned vertically and exhausting into free space. The Martel test facility is open to the external environment and is therefore subject to ambient noise. The facility is not fully anechoic, however it is acoustically treated. A Laser Doppler Anemometer (LDA) system was operated in forward scatter using two configurations. Firstly, one point / two component (as depicted in figure 4.5) and secondly two-point / one-component. The laser light source was generated by a 5 watt argon-ion laser producing both blue and green beams. Silicon dioxide seeded both the potential core and shear layer, with particles of diameter $\sim 0.4 \mu m$.

FIGURE 4.4: *Close-up of the JEAN nozzle*

Jet No.	Temperature T_s/T_a	Velocity V_j/a_0	Velocity V_j $[m/s]$
3	1	0.75	253.31
4	1	0.90	303.98
8	2	0.75	253.31
9	2	0.90	303.98

TABLE 4.1: *JEAN temperature and velocity information*

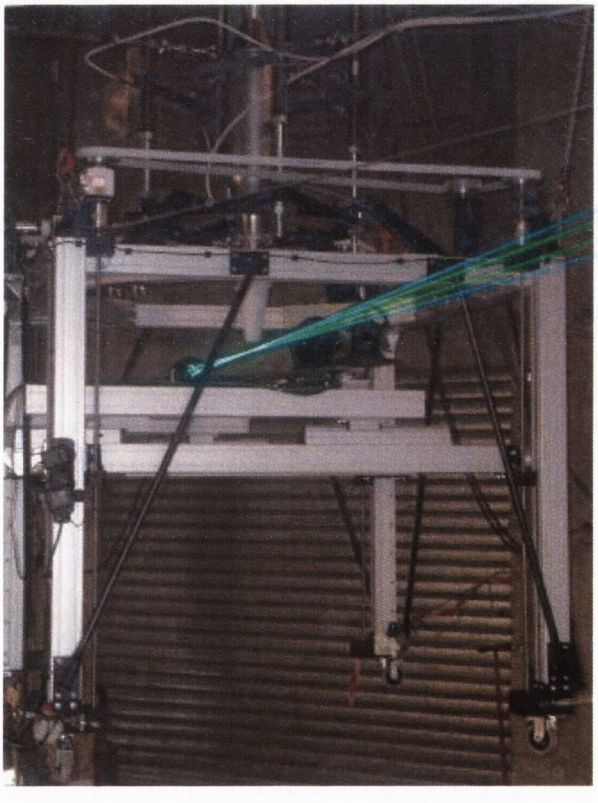

FIGURE 4.5: *One point / two component measurements performed at CEAT Poitiers, France under the JEAN contract*

The single point measurements were used to map the jet and determine characteristics such as potential core length and location of the shear layer. The two velocity components were acquired simultaneously so that the Reynolds stress components could be obtained. Mapping the jet enabled the two-point measurements to be performed in those areas within the jet considered to be responsible for noise generation. These two-point measurements were then performed for

various axial locations within the jet ($X = 3/4Lc$, Lc, $5/4Lc$, where Lc represents the location of the potential core for each jet). From these, the correlation functions of the longitudinal component velocity and Reynolds stress fields can be determined. The length and time scales can then be estimated from these correlation functions.

The axial and radial profiles of the mean (U & V) and turbulent (u', v' & $u'v'$) velocities were obtained from single-point two-component measurements. The axial profiles were normalised with respect to the jet exit velocity (V_j), are shown in figure 4.6 as a function of x/L_c, where x is the axial position and L_c

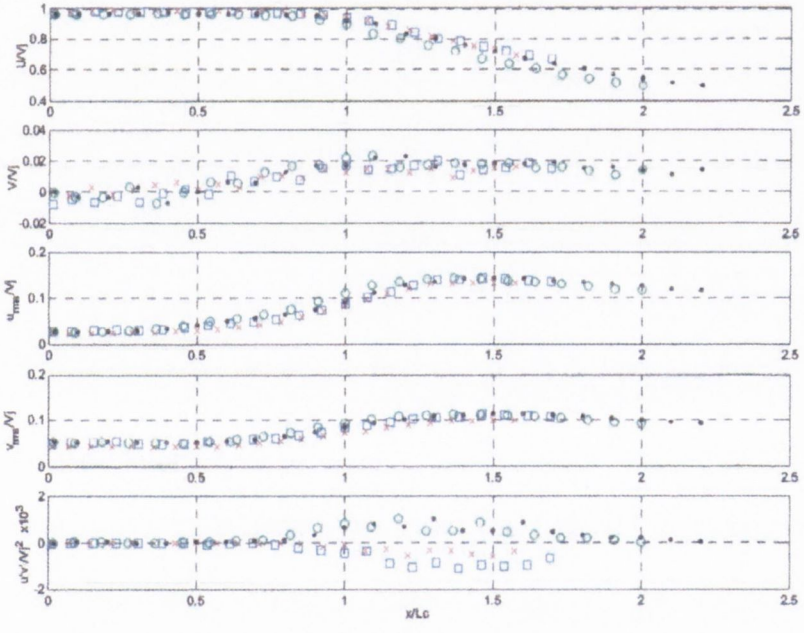

FIGURE 4.6: *Axial distribution of the mean velocity components (measurements performed at CEAT Poitiers, France under the JEAN contract)* □ *Jet 3,* × *Jet 4,* • *Jet 8,* - *Jet 9*

the length of the potential core evaluated at $U = 0.95V_j$. Using this criterion the potential core length for Jet 3 is estimated at $6.5D$. The radial profiles, normalised with respect to the jet exit velocity, are shown in figure 4.7 for x/D

values of 1, 2.5 & 5 as a function of y/D. This data was analysed as part of the JEAN contract and presented in Technical Reports [46].

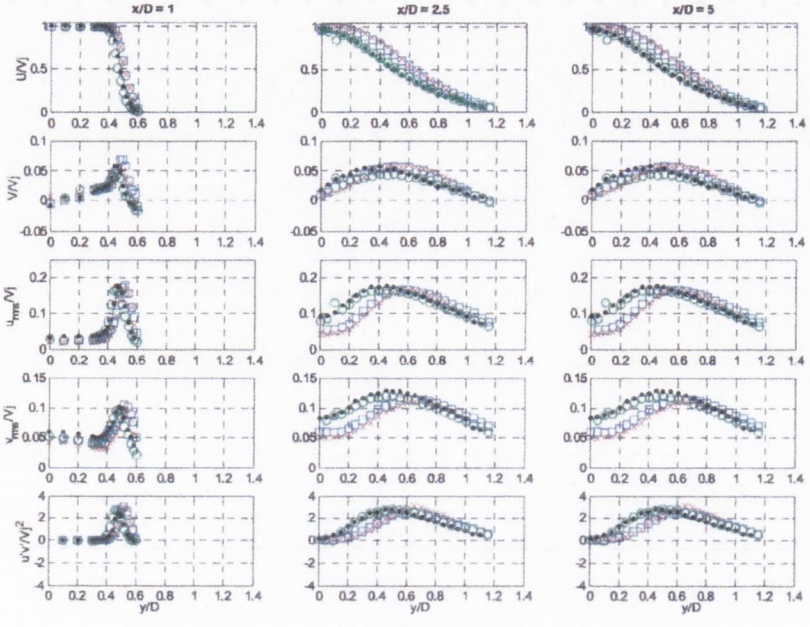

FIGURE 4.7: *Radial distribution of the mean velocity components (measurements performed at CEAT Poitiers, France under the JEAN contract)* □ *Jet 3,* × *Jet 4,* . *Jet 8,* - *Jet 9*

4.2.2 Auto Spectra

The first comparison between the two processing techniques will focus on the estimate of the auto spectrum. The LDA measurement position for this example was on the shear layer axis at the end of the potential core for the Mach 0.75 jet (jet No. 3 in table 4.1), depicted in figure 4.8 as '$x4y2$'. The auto spectra shown in figure 4.9 reveal the standard turbulent shape that would be expected for this particular measurement location. Here it can be seen that the Sample & Hold estimate, shown in black, compares very well with the Slot Correlation estimate, shown in blue. The Sample & Hold estimate reaches a slightly higher

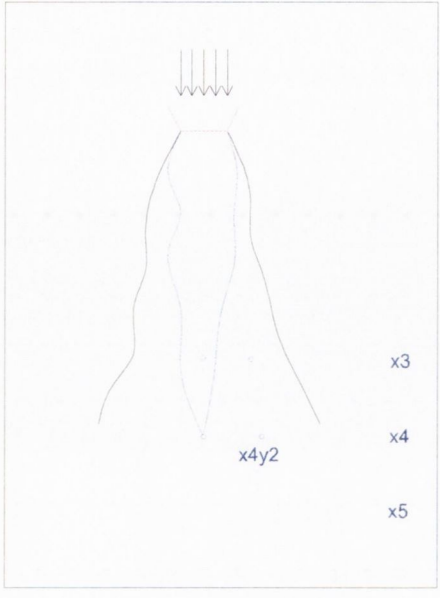

FIGURE 4.8: *Location of JEAN two-point measurements on Jet 3*

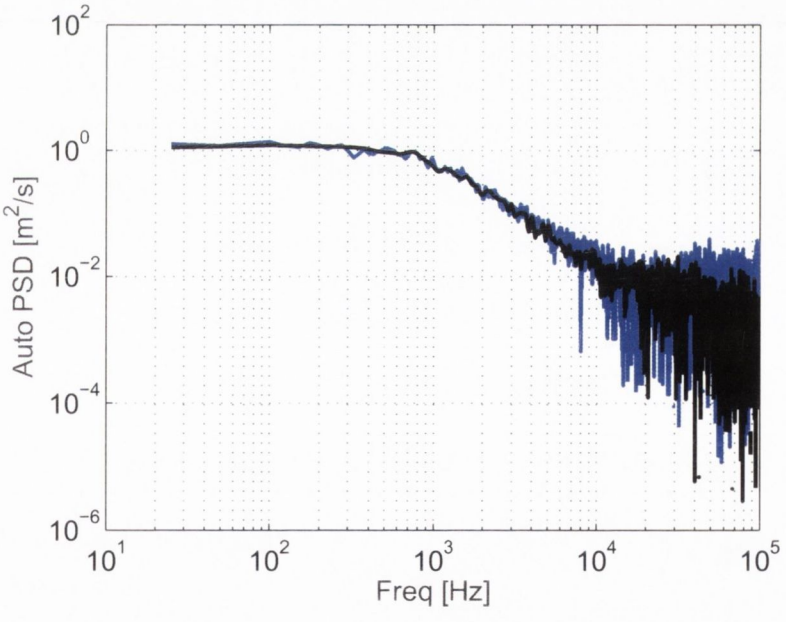

FIGURE 4.9: *Comparison of Sample & Hold estimates (black) to Slot Correlation estimate (blue) of the auto spectra of u' (Jet 3)*

frequency resolution, but both techniques easily attain the Nyquist frequency of $20kHz$. Above this Nyquist frequency the noise to signal ratio is too high to interpret the auto spectra. It should be noted that the auto spectral estimates as

plotted in figure 4.9 could be misinterpreted at higher frequencies. The Sample & Hold reconstruction is performed at a re-sample rate of approximately ten times the data rate, however this does not imply that the estimates are accurate at frequencies above the mean data rate of the original acquired signal.

4.2.3 Cross Spectra

Two point/one component measurements entail the first measurement, u_1', being fixed (at position '$x4y2$' in figure 4.8), while u_2' represents the measure of the movable point. Therefore the cross spectrum of the resulting data will have a displacement between the two measurement points, except for the initial position, where both points coincide. The cross spectral estimates used in this comparison are for the initial position and are shown in figure 4.10. The estimates for the PSD of $u_1'u_2'$ for both techniques compare well in magnitudes and shape, with some small deviations at higher frequencies.

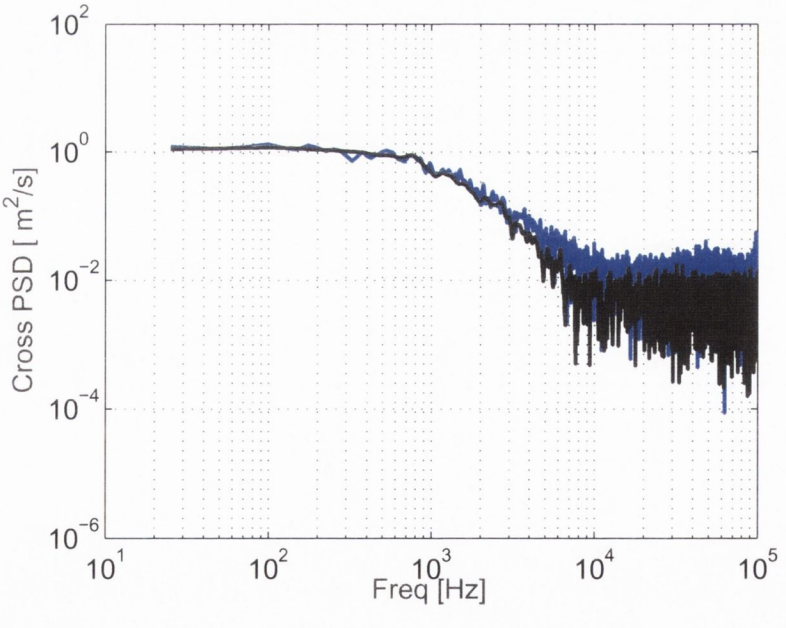

FIGURE 4.10: *Comparison of the cross spectrum of u_1' & u_2' with 0D separation: Sample & Hold (black) and Slot Correlation (blue)*

4.2.4 Coherence & Phase

The coherence between two-point/one-component measurements gives the spatial decay as the second measurement moves away from the first. In figure 4.11 the results obtained from Sample & Hold and Slot Correlation are presented, where each plot represents the coherence for five different axial displacements (0, 0.18, 0.62, 1.26, and $1.9D$). As this displacement increases it is expected that the coherence will reduce. On comparison of Sample & Hold versus Slot Correlation, the coherence estimates can be seen to differ. With zero separation between the measurement positions, the Slot Correlation coherence is greater than one, over most frequencies, whereas with Sample & Hold a definite frequency dependence manifests itself in the coherence estimates, with a decay occurring above 1kHz. The frequency resolution seen for the auto and cross spectra will not be achieved for the coherence estimates, even when the measurements are spatially coincident, as discrepancies in positioning and local interference can occur in experimental testing.

When the axial separation is increased to $0.18D$, a similar result is noted, i.e. Slot Correlation estimates a coherence greater than one while Sample & Hold estimates a frequency decay. A coherence of greater than one is only seen with Sample & Hold when the effect of the noise to signal ratio is present. Consequently it would appear that Slot Correlation is less reliable when estimating the coherence between measurements taken in close proximity of each other. Having regard to the small diameter of LDA beams it is not considered that overlapping of the fringes could give rise to this phenomenon, especially at a separation of $0.18D$. When the separation between the measurement positions is increased to $0.62D$ both techniques appear to estimate a similar decay of coherence over the frequency range of 0-3kHz. This continues to be the trend between the two techniques as this observed decay is seen for displacements of 1.26 and $1.9D$.

A peak can be seen in the region of $200 - 300Hz$ in figure 4.11. These peaks correspond to the Strouhal instability of the MARTEL jet for this particular location, which was noted as 0.4 in the JEAN reports [46].

The phase is presented in figure 4.12 for both techniques, where the same

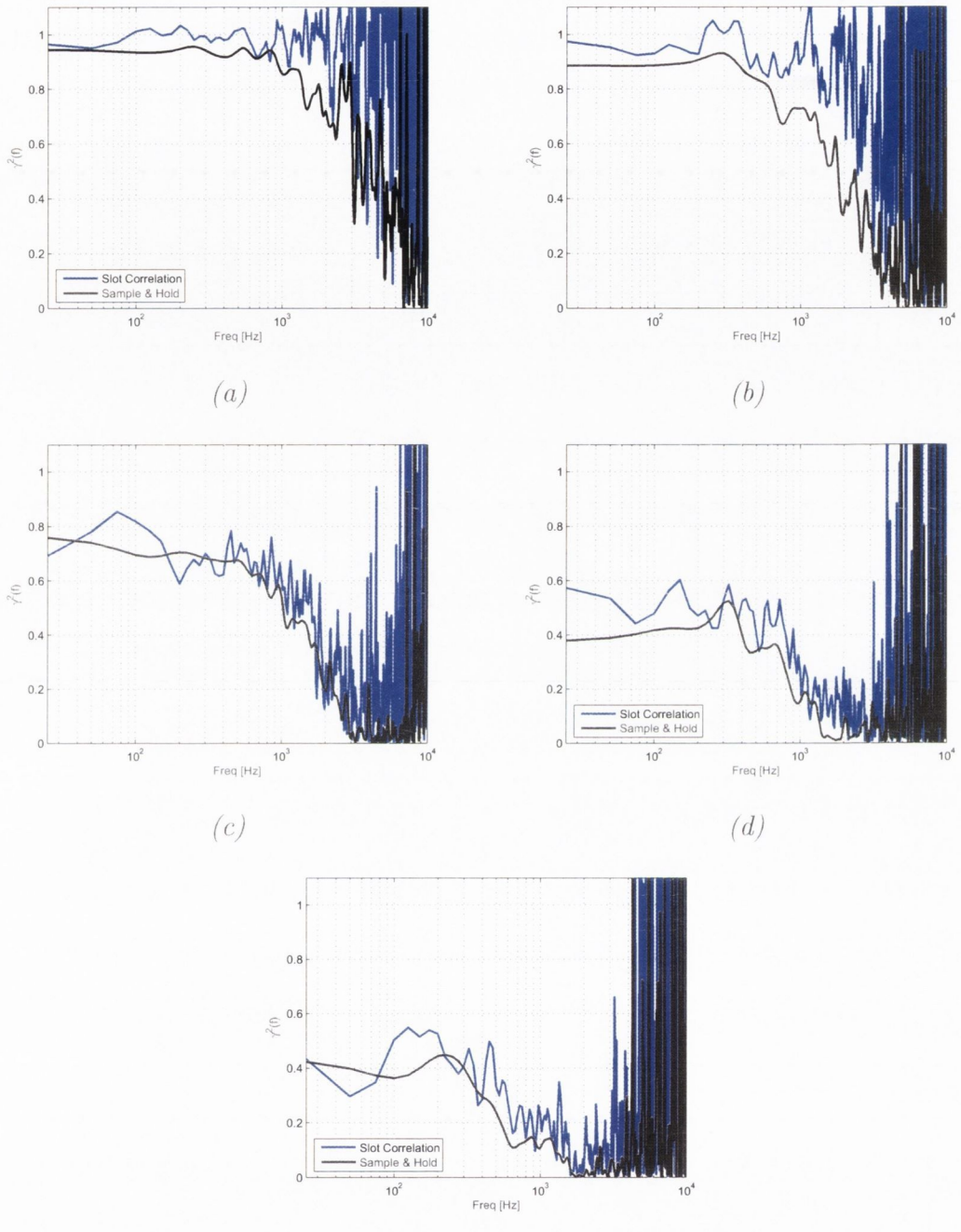

FIGURE 4.11: *Comparison of Coherence estimates from the two-point measurements where the displacements are (a)* 0*, (b)* 0.18*, (c)* 0.62*, (d)* 1.26 *& (e)* 1.9D *: Sample & Hold (black), Slot Correlation (blue)*

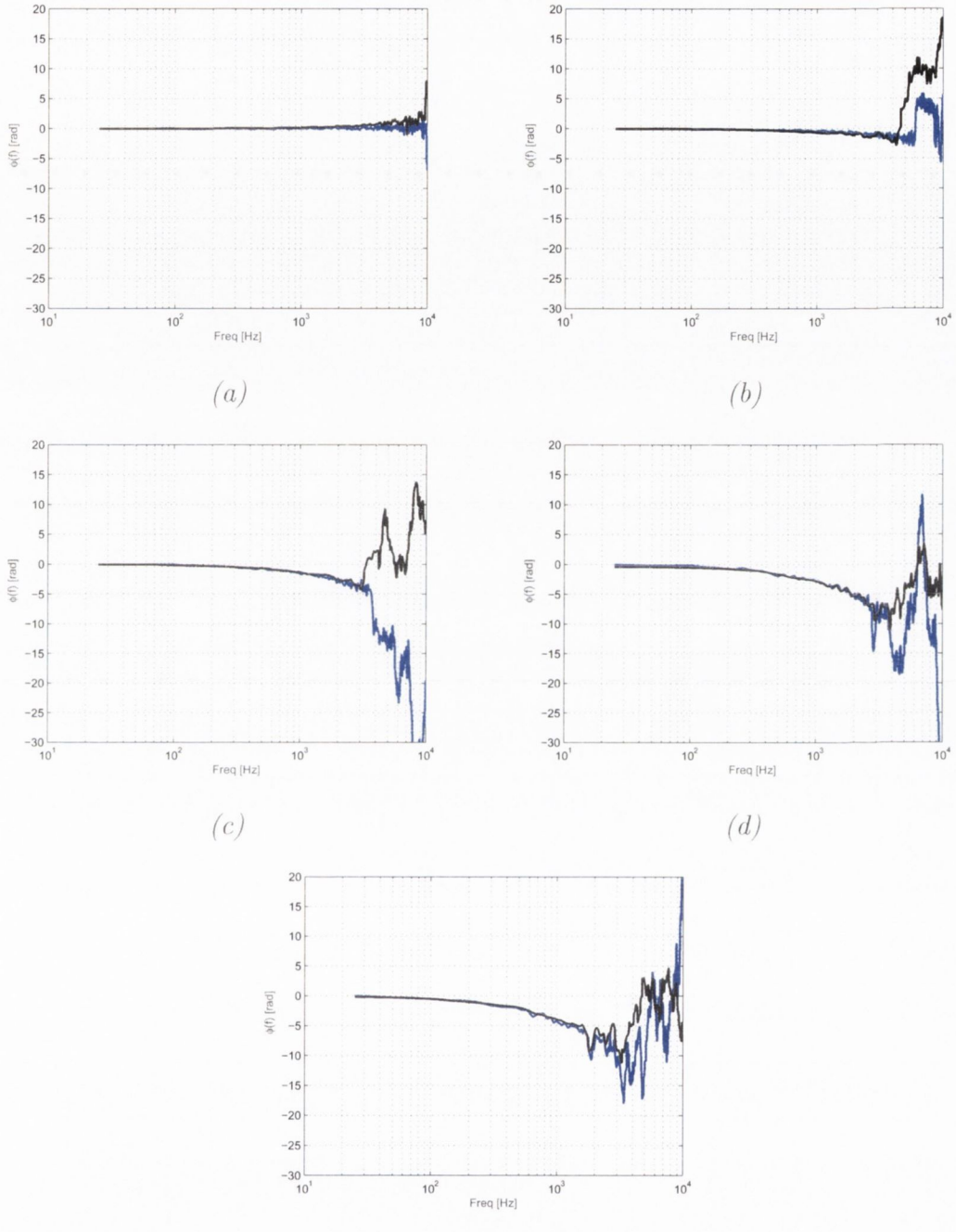

FIGURE 4.12: *Comparison of Phase estimates from the two-point measurements where the displacements are (a)* 0, *(b)* 0.18, *(c)* 0.62, *(d)* 1.26 *& (e)* 1.9*D* : *Sample & Hold (black), Slot Correlation (blue)*

displacements for the coherence were examined. When the measurement positions coincide (i.e. $0D$), both techniques show excellent agreement, with only some difference occurring at the high frequency end. The phase is realistic up to the point where the coherence reaches zeros, and this is due to the lack of step noise contamination. With increasing displacement the phase estimates of both Sample & Hold and Slot Correlation result in a consistent pattern of decay.

A variable phase can be observed for displacements of $0.62D$, $1.26D$ and $1.9D$ which suggests that the turbulent structures are convecting at varying speeds. This can physically be applied to a jet, since a jet will consist of large and small scales structures that will convect at different speeds and dissipate at different rates. The limit of reliability of the phase estimates decreases with increasing separation. This is due to the lower frequencies, which represent the larger structures in the jet, being capable of being examined over these greater distances. Whereas the higher frequency, small scale structures, dissipate over these greater distances. The previously noted noise to signal limit of 10 revealed a frequency resolution of the Nyquist frequency from the auto spectrum. This limit is also evident in the phase estimates, in particular in figure 4.12 (a), where the phase estimates are reliable up to this limit only.

4.2.5 Cross Correlation

Performing two-point/one-component measurements also enables the extraction of information such as length and time scales and bulk convection velocities from the correlation domain. It is necessary that Sample & Hold can also accurately predict these parameters.

The cross correlation function for a number of normalised separations, shown in figure 4.13, show the classical form of spatio-temporal correlations. Using the same five separations of $0, 0.18, 0.62, 1.26$, and $1.9D$ reveals that some discrepancies between the two techniques are observed. One possible reason stems from the way in which Sample & Hold and Slot Correlation estimate the correlation domain. Sample & Hold does not appear to consistently over or underestimate the curves compared to Slot Correlation, as seen by the five locations in figure

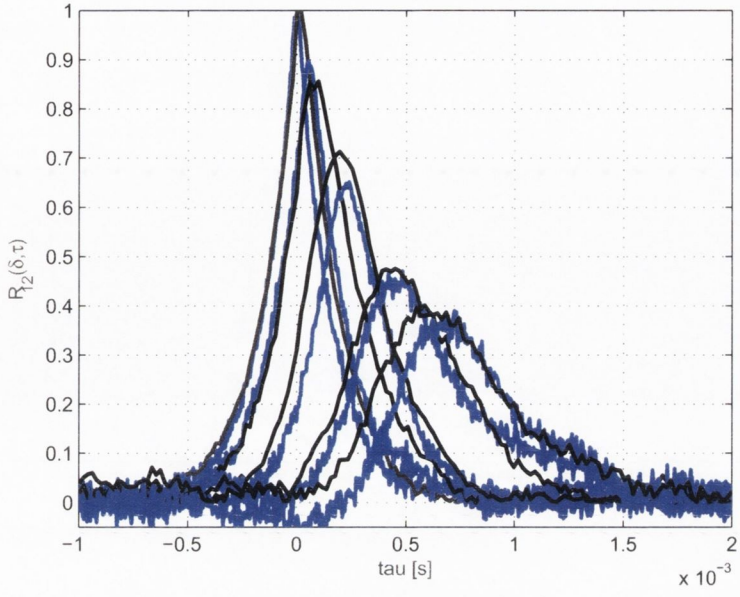

FIGURE 4.13: *Cross Correlation estimates using Sample & Hold (black) and Slot Correlation (blue) for displacements of* 0, 0.18, 0.62, 1.26, *and* 1.9D

4.13 but the overall comparison between the two techniques is very good.

4.2.6 Convection Velocity

The correlation domain can be examined in iso-contour form which provides information on the bulk convection velocity. Figure 4.14 illustrates this for both Sample & Hold and Slot Correlation. This convection velocity is calculated from the slope of the line that intercepts the correlation peaks when plotted in iso-contour form. These calculated bulk velocities are included in table 4.2. Good agreement between the iso-contour plots can be seen, with similar overall evolution as noted by the comparable bulk convection velocities.

The bulk convection velocity is not an accurate representation of the convection velocities within a jet. Since a jet will consist of different size structures it is essential that the convection velocity, as a function of frequency, be examined. This frequency dependance can be extracted from the previously examined phase plots (figure 4.12) using the formulation:

$$U_c = \frac{2\pi f \delta}{\phi} \tag{4.1}$$

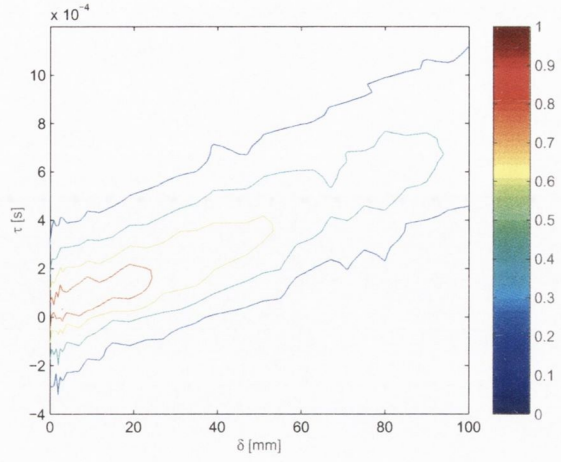

(a)

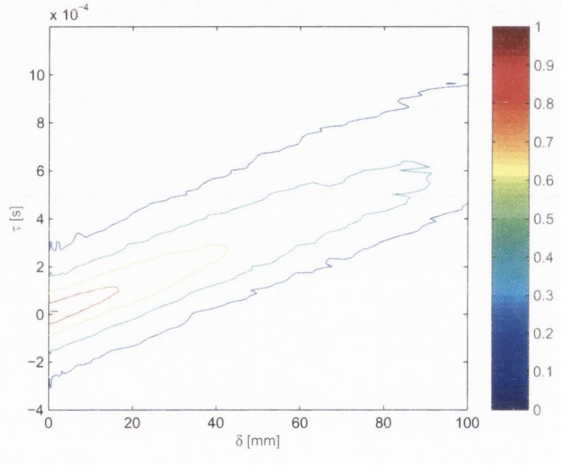

(b)

FIGURE 4.14: *Contour Correlation Curves from two-point / one-component measurements (a) Sample & Hold (b) Slot Correlation*

where f is the frequency, δ the displacement observed between the two measurement positions and ϕ the phase. Figure 4.15 shows how Sample & Hold and Slot Correlation deal with this extraction of the frequency dependance of convection velocity where all displacements from the two-point measurements are used. A definite increase in velocity with frequency is evident up to approximately $2kHz$ for both techniques. Where the larger structures are convecting at slower speeds and the small scale structures at higher speeds. It is clear that the previously

estimated bulk convection velocities correspond to frequencies of approximately $800Hz$ (for S&H) and $1100Hz$ (for Slot).

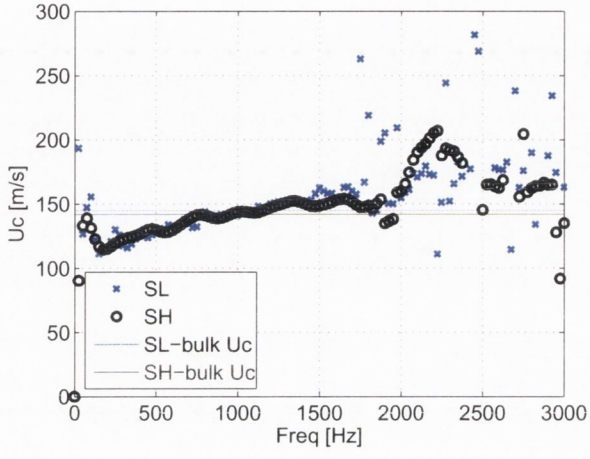

FIGURE 4.15: *Convection Velocities as a function of frequency, included also are bulk convection velocities*

4.2.7 Spatial-temporal correlations

The spatial-temporal correlation function $R_{12}(\delta, \tau)$ can be separated into the spatial and temporal decreases denoted by $R_{12}(\delta, 0)$ and $R_{12}(0, \tau)$ respectively. These are shown in figure 4.16 where similar esimates are observed. As can be seen from figure 4.16 (b) insufficient points were acquired to estimate the temporal correlation. Therefore in order to estimate this scale the data was extrapolated and an exponential curve was fitted to the data. When these functions are integrated over separation distance and time, the length and time scales are obtained, as detailed in table 4.2. Overall differences of less than 15 per cent are globally seen between both techniques, but Sample & Hold gives higher estimates of length and time scales as compared to the Slot Correlation method.

4.2.8 Concluding Remarks

The aim of this section was to validate the Sample & Hold technique proposed by Simon & Fitpatrick [40], versus the most commonly used alternative, i.e.

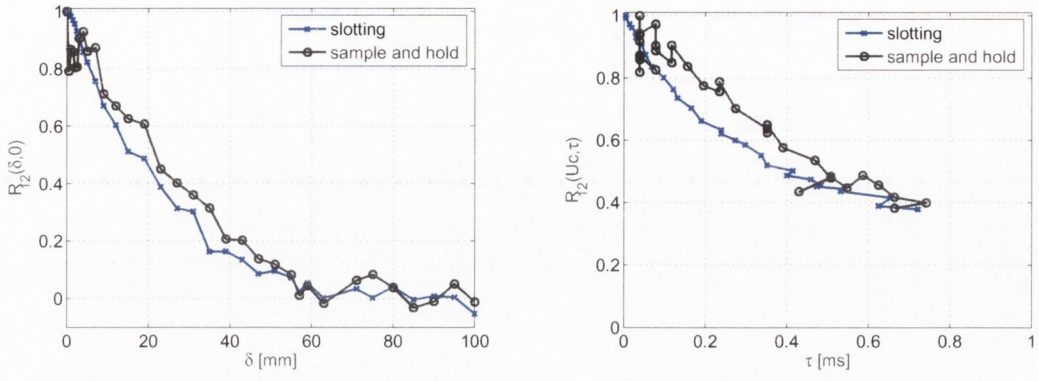

(a) *(b)*

FIGURE 4.16: *Spatial and Temporal Correlation functions comparing Sample & Hold (black) and Slot Correlation (blue) (a) spatial, (b) temporal*

Jet	Technique	Length Scale [mm]	Temporal Scale [ms]	Convection Velocity [m/s]
Mach 0.75	S & H	56	0.77	142
	Slotting	45	0.69	145

TABLE 4.2: *Length & Time Scales and Convection velocity estimates using Sample & Hold and Slot Correlation*

Slot Correlation. The outcome of the physical results that were obtained from the two-point/one-component measurements is not the issue here; the data sets have already been analysed in this regard, for example by Jordan & Gervais [47] and Laurendeau et al [48]. The purpose was purely to validate the processing methods of this Sample & Hold technique.

The use of the procedures proposed by Simon & Fitzpatrick [40] for Sample & Hold reconstruction achieved an upper frequency limit of $f_m/2$ for PSD estimates for both auto and cross spectra. This replaces Adrian & Yao [36] frequency limit of $f_m/2\pi$. The auto spectra estimates from Sample & Hold and Slot Correlation compared well. Some discrepancies between the techniques were noted for the cross spectra and correlation functions. From this study it would appear that

Slot Correlation still has some difficulties with the coherence estimates. However both techniques determine very similar phase estimates, and consequently comparable estimates of the convection velocity as a function of frequency. An added advantage of Sample & Hold is the shorter time required to process data.

Finally, Sample & Hold can provide, if required during acquisition for example, a very powerful and fast insight into randomly sampled data. Sample & Hold more accurately estimates the frequency domain while the Slot Correlation technique is more accurate in the correlation domain, suggesting a combined method would best be suited to this type of LDA data, in order to examine both the frequency and correlation domains.

4.3 LDA acquisition modes

As detailed, LDA data is acquired randomly, however there is another concern regarding LDA acquisition that needs to be addressed as it also affects the processing technique of Sample & Hold. LDA data can be acquired in one of two ways, either in *non-coincident mode* or *coincident mode*. These modes of acquisition differ in how the random data is acquired. For non-coincident acquisition the two measurement positions sample independently, i.e a particle can pass through the fringes of either measurement position and its velocity is registered, whereas coincident mode requires that a particle be registered by both positions at the same time. Realistically, coincident mode can only be implemented for one-point/two-component measurements. In chapter 3 the procedures for dealing with the different corrections associated with non-coincident and coincident data when using Sample & Hold reconstruction was obtained. What was not mentioned was the extraction procedure necessary to obtain all the Reynolds stress terms from one-point / two-component measurements. The turbulent velocity fluctuations (u' & v') and Reynolds stresses (u'^2, v'^2 & $u'v'$) can all be obtained from coincident time domain data. However when data is acquired using the non-coincident mode the Reynolds stress term $u'v'$ needs to be calculated from $u'(t)$ and $v'(t)$ which have been sampled independently. The approach taken is to estimate this term from

the reconstructed time series of $u'_r(t)$ and $v'_r(t)$. The aim of this section is to examine the effect that the mode of acquisition has on the estimation of spectra and on the extraction of the Reynolds stress term $u'v'$, as this term plays an important role in the prediction and understanding of jet noise.

4.3.1 Velocity Fluctuations

Controlled measurements to examine in detail the effects of the mode of acquisition were performed on a subsonic jet of $50mm$ diameter at a velocity of $80m/s$. For this comparative study of LDA acquisition modes the data was acquired in either non-coincident or coincident mode and the LDA system was setup to acquire two-point / one-component data (the axial component - denoted u, and the radial component - denoted v). The experimental details for these tests are described in chapter 6.

As the approach to extract the $u'v'$ term from non-coincident data is to use the reconstructed time series it is essential first to compare the velocity fluctuation estimates from both acquisition modes. The first comparison is of the estimation of the PSD of u'. The estimated PSD are illustrated in figure 4.17 for both acquisition modes. Generally the data rates associated with non-coincident data are higher than those obtained for coincident. As table 4.3 reveals the data rate associated with the non-coincident u' term is more than double that for the coincident mode. As previously shown the Sample & Hold spectral estimates will be accurate up to approximately $f_m/2$, i.e. half the data rate. This automatically implies

Data Type	Data rates (f_m)	Resample rates
Non-coincident	u' - 68kHz & v' - 27kHz	800kHz
Coincident	u' & v' - 25kHz	400kHz

TABLE 4.3: *Data rates and Re-sample rates for non-coincident and coincident modes*

that the frequency resolution associated with the non-coincident estimate will be higher than that of the coincident estimate. However, as previously discussed, the

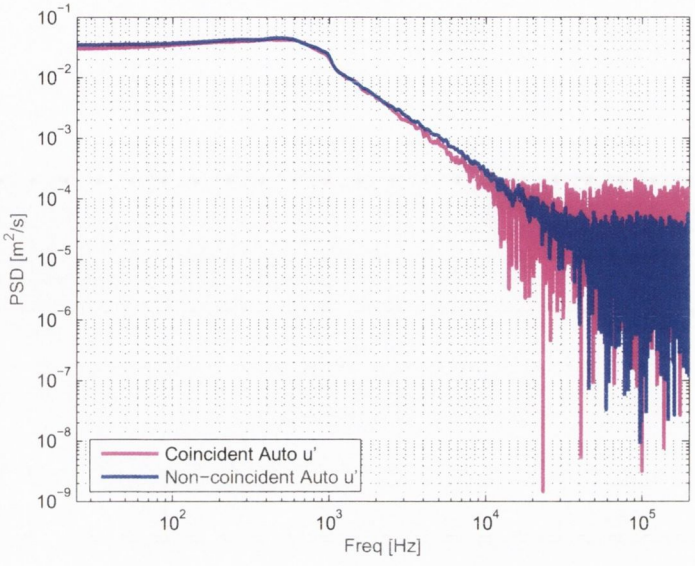

FIGURE 4.17: *Auto Spectrum of u′ : Comparison between Coincident and Non-coincident modes*

noise to signal ratios also play an important role in spectral estimates. Figure 4.18 shows the noise to signal ratios for both coincident and non-coincident modes for u'. The noise to signal ratio for the coincident mode reaches the limiting value of ten at approximately $10kHz$ whereas the non-coincident mode obtains a higher frequency of approximately $30kHz$. Despite the different frequency resolution

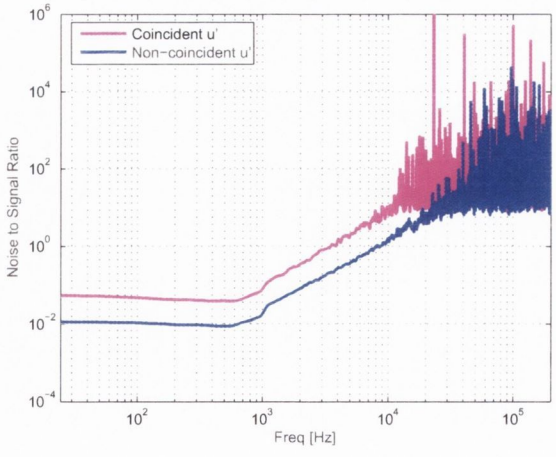

FIGURE 4.18: *Noise to Signal Ratio of u' : Comparison between Coincident and Non-coincident modes*

between the two modes the overall shape and levels of both PSD estimates of u' (figure 4.17) compare well.

The examination of the radial fluctuation is shown in figure 4.19, where the coincident and non-coincident auto spectral estimates are almost exact. The estimates are accurate up to a frequency of approximately $f_m/2$ $(12kHz)$. Table

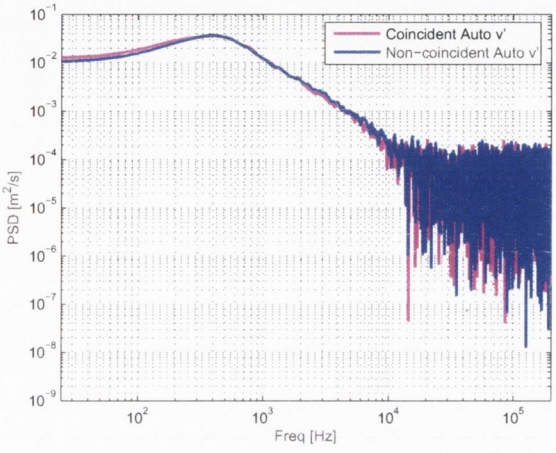

FIGURE 4.19: *Auto Spectrum of v' : Comparison between Coincident and Non-coincident modes*

4.3 gives the data rates associated with non-coincident v', which is similar to the coincident data rate. The noise to signal ratios (figure 4.20) show that the estimates from the different modes of acquisition show little difference in shape, magnitude and frequency resolution.

4.3.2 Reynolds Stress Terms

The Reynolds stress terms of u'^2 and v'^2 are estimated directly from the random time series of u' and v'. Therefore the comparison of modes on their auto spectra should not present any changes already seen from the velocity fluctuations. Figure 4.21 shows the auto spectra for these Reynolds stress terms using both coincident and non-coincident modes of acquisition. Slight differences occur with the u'^2 estimates, which as seen from u' is due to the data rates, whereas the v'^2 estimates compare very well.

The final Reynolds stress term $u'v'$ from non-coincident data is calculated

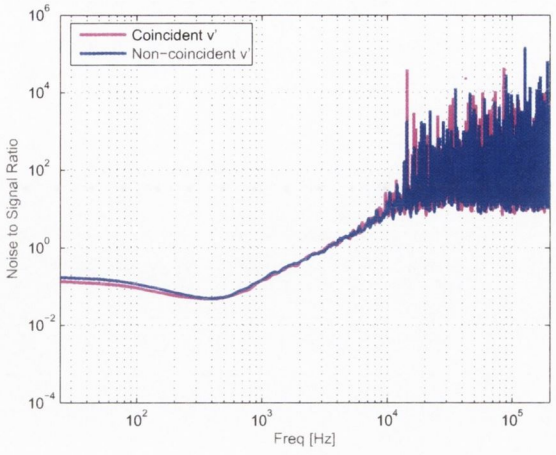

FIGURE 4.20: *Noise to Signal Ratio of v' : Comparison between Coincident and Non-coincident modes*

from the reconstructed time series of $u'_r(t)$ and $v'_r(t)$. The auto spectra of the Reynolds stress term $u'v'$ derived from the non-coincident and coincident data is shown in figure 4.22. Firstly it can be seen that some discrepancies exist at the low frequency end of the spectrum, with the non-coincident mode estimating a slightly higher energy value. Evident also is a difference in the spectral shape which occurs in the region of $3-10kHz$. On examination of the noise to signal ratios, as shown in figure 4.23, similar differences are revealed between the acquisition modes. The maximum frequency resolution appears again to be dependant on the data rate and the noise to signal ratio, with the non-coincident mode achieving a slightly higher resolution than the coincident estimate.

To establish whether the varying data rates results in the observed differences, data with the same acquisition rates for all components in both non-coincident and coincident modes was acquired. Although this is difficult experimentally as coincident acquisition normally results in lower data rates. Figure 4.24 illustrates the spectral estimate for u' when the data rate for all components for both non-coincident and coincident acquisition was approximately $56kHz$. Since the data rates are the same throughout, the filter correction associated with each component is the same. Figure 4.24 shows that the only remaining discrepancy between the two estimates occurs at the low frequencies where again the non-coincident

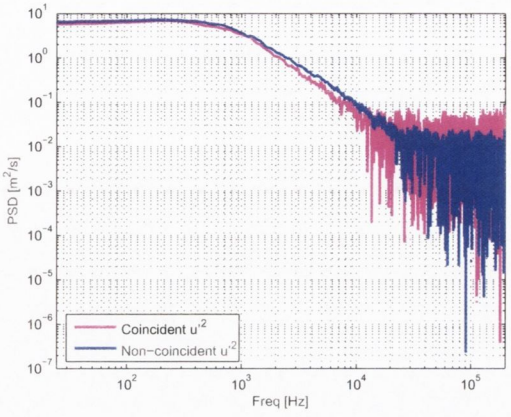

(a)

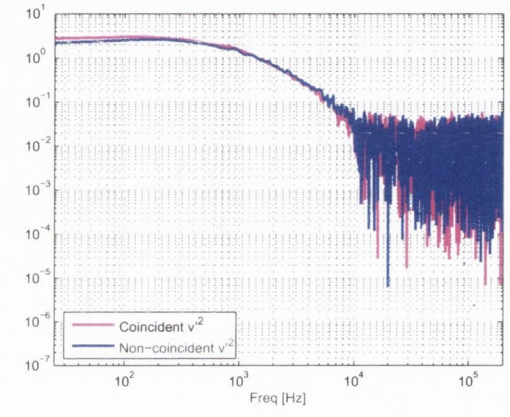

(a)

FIGURE 4.21: *Comparison between Coincident and Non-coincident modes of the Auto Spectrum of* (i) u'^2 *and* (ii) v'^2

mode estimates a different magnitude and shape to that of the coincident mode. The remaining shape, magnitude and frequency resolution are identical. The corresponding noise to signal ratios, shown in figure 4.25, also reveal this discrepancy at the low frequency end from the non-coincident data. This suggests that the technique of combined the reconstructed non-coincident signals of $u'_r(t)$ and $v'_r(t)$ is causing this low frequency discrepancy seen in both the auto spectrum and the noise to signal ratio.

The nature of non-coincident data is that the two LDA signals are uncorrelated, in other words, their time traces are not identical. However, especially

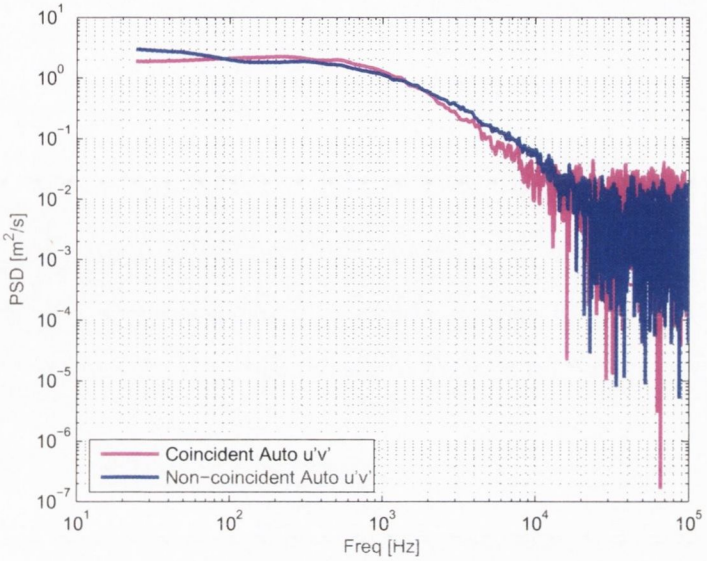

FIGURE 4.22: *Auto Spectrum of $u'v'$: Comparison between Coincident and Non-coincident modes*

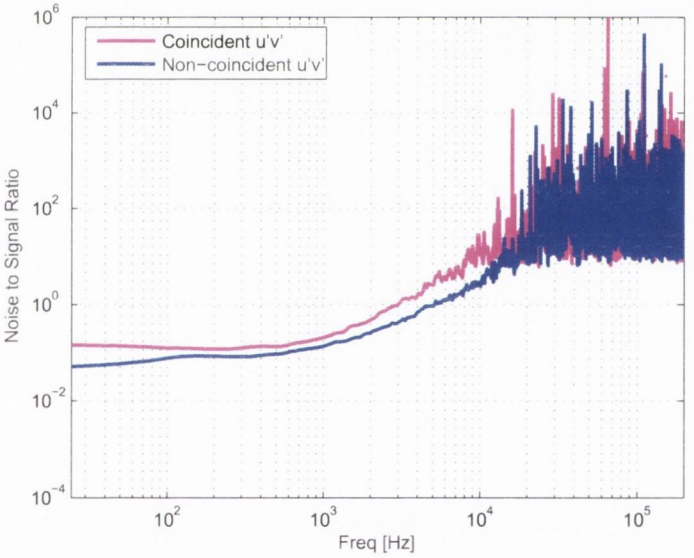

FIGURE 4.23: *Noise to Signal Rations of $u'v'$: Comparison between Coincident and Non-coincident modes*

with high data rate acquisition it cannot be guaranteed that a particle will pass through the two volumes and be registered at the same time. Table 4.4 shows a sample time trace, where the times in bold and color coded highlight that coincident acquisition occurs when running in non-coincident mode. However, these

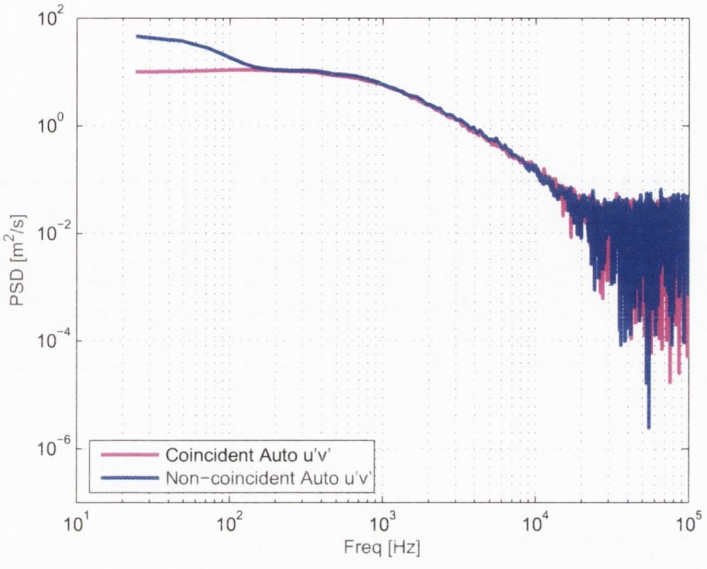

FIGURE 4.24: *Auto Spectrum of u'v' (same data rates) : Comparison between Coincident and Non-coincident modes*

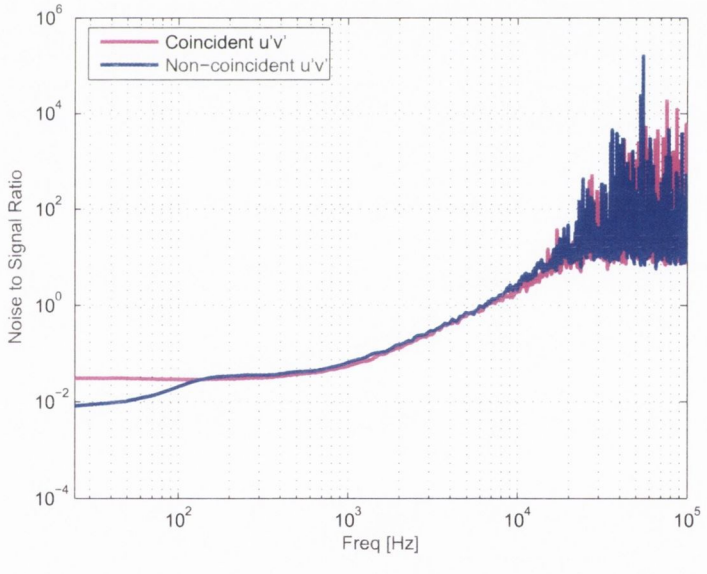

FIGURE 4.25: *Noise to Signal Rations of u'v' (same data rates): Comparison between Coincident and Non-coincident modes*

occurrences should not affect the estimation of an auto spectrum. The possible complication arises when calculating the cross spectrum and subsequently the coherence.

Time u [sec]					
0.0556	0.0872	0.1027	0.1125	0.1373	0.1437
0.1526	0.1557	0.1659	0.1687	**0.1712**	0.1770
0.1921	0.1978	0.1990	0.2383	0.2398	0.2465
0.2531	0.2667	0.2720	0.2739	0.2851	0.3067
0.3235	0.3289	0.3338	**0.3470**	0.3534	0.3861
0.3937					
Time v [sec]					
0.0559	0.0874	0.1375	0.1439	0.1690	**0.1712**
0.1773	0.2401	0.2723	0.3291	**0.3470**	0.3535
0.3937	0.4259	0.4352	0.4367	0.4474	0.4581
0.5716	0.5864	0.6451	0.6638	0.7005	0.7098
0.7211	0.7307	0.7505	0.7660	0.8282	0.8368
0.8437					

TABLE 4.4: *Sample time trace for two non-coincident signals measuring axial and radial velocities*

4.3.3 Coherence estimates

Good spectral estimates of the velocity fluctuations and the Reynolds stress components are necessary if these are to be used to identify noise source mechanisms. In chapter 6, the use of a five input model (inputs being u', v', u'^2, v'^2 and $u'v'$) to identify possible sources requires accurate estimates of the auto and cross spectra of these five inputs. This enables the conditioned coherence (i.e. where the mutual coherence between the inputs is removed) to be calculated. Accurate coherence estimates are required for the extraction of length and time scales, as a function of frequency, as shown by for example Kerhervé et al [30]. To complete the comparison of acquisition modes, the coherence between the velocity fluctuations and the Reynolds stress terms are examined.

Figure 4.26 shows the coherence between all five components for both the

non-coincident and coincident modes. In both cases the uncorrected (dashed line) and corrected (solid line) coherence is shown, for the non-coincident acquisition (left column) and the coincident acquisition (right column). In chapter 3 the corrections were detailed to calculate the coherence between two LDA signals, equation 3.14 for non-coincident and equation 3.18 for coincident, where both corrections were a function of the noise to signal ratios, (α_1 & α_2). It can be seen that the modes have varying effects on the coherence estimates. It would appear that the non-coincident corrected estimates are in general greater than those obtained from the coincident data. These variations are not confined to the Reynolds stress term of $u'v'$. The velocity fluctuations are also affected. The most notable differences between the two modes occur as a result of the noise to signal ratios used to correct the coherence. This is clearly evident for the non-coincident corrected coherence in figure 4.26, where it can be seen the coherence rises dramatically when the frequency is above $1kHz$. By comparison the corrected coincident estimates do not exhibit a similar characteristic above this frequency.

This data was acquired with the measurement volumes positioned in the shear layer close to the edge of the potential core. At this location the flow is anisotropic, i.e. $u' \neq v'$. The flow will be dominant in the axial direction, implying that the Reynolds stress term of u'^2 will be the dominant source in this region. This physically explains why, for example, in figure 4.26 (a) a lower coherence is noted between u' & v' than u' & u'^2.

The example with constant data rates is examined in relation to the non-coincident and coincident coherence estimates, and is shown in figure 4.27. The coherence between u' & v', u' & $u'v'$ and u'^2 & $u'v'$ are shown. The comparison for u' & v' show very similar coherence estimates for non-coincident and coincident. Some difference is noted at low frequencies in the coherence estimates of u' & $u'v'$. However the main differences occur from the coherence estimates of u'^2 & $u'v'$, where the consequence of the low frequency variation seen in the auto spectra of $u'v'$ is witnessed.

A final note must be made on the observed coincident data that is inherent

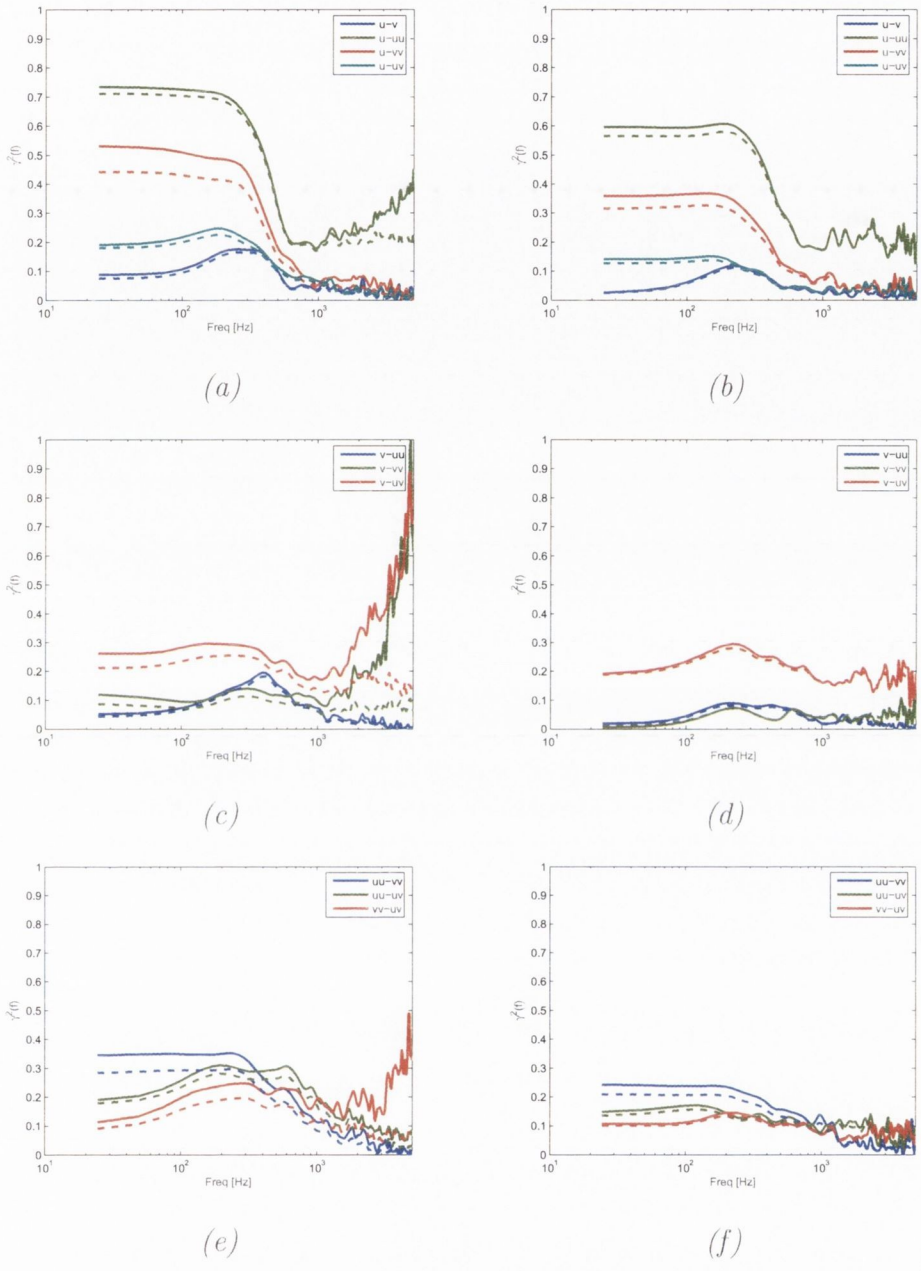

FIGURE 4.26: *Uncorrected Coherence (dashed line) and Corrected Coherence (solid line) between the velocity fluctuations and Reynolds stresses, left column : Non-coincident, right column : Coincident*

in non-coincident acquisition and the implications for coherence estimates. As chapter 3 detailed, when two LDA signals are acquired in coincident mode, the cross spectrum is contaminated by step noise and consequently the actual co-

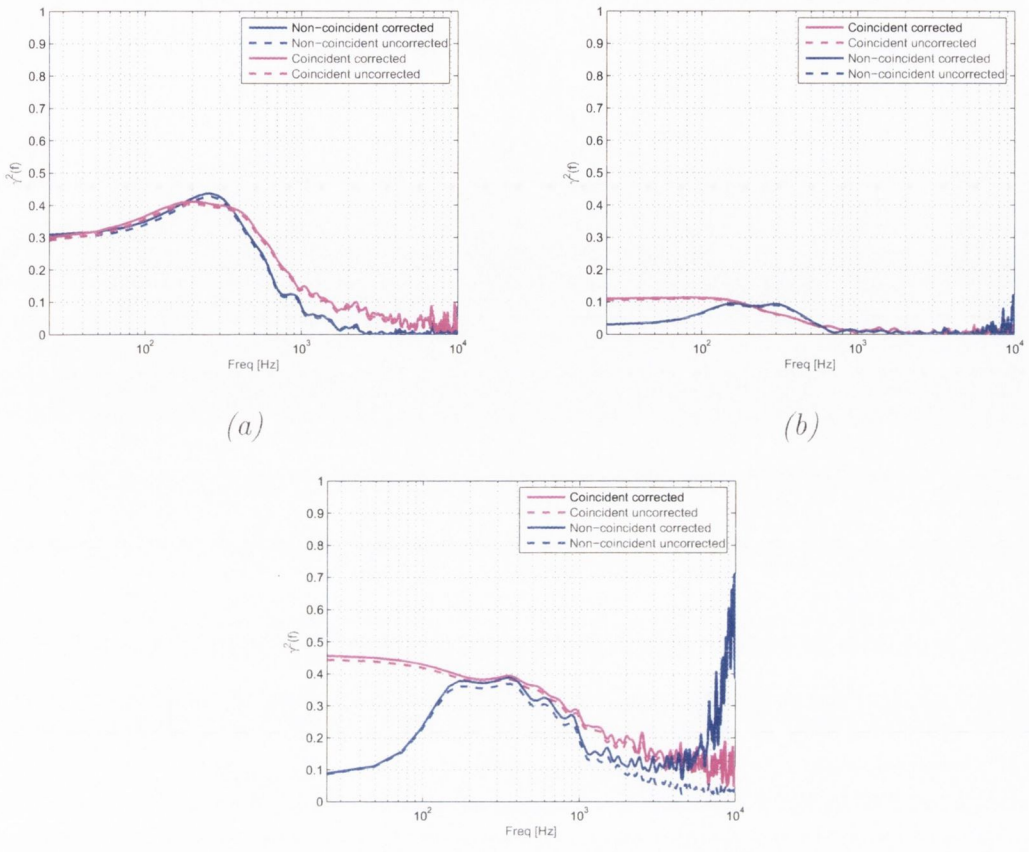

FIGURE 4.27: *Uncorrected Coherence (dashed line) and Corrected Coherence (solid line) between (a) u' & v', (b) u' & $u'v'$ and (c) u'^2 & $u'v'$*

herence is estimated by equation 3.18. For non-coincident data, no step noise contamination occurs and equation 3.14 is applied in this case. However, the question arises, when data is acquired in non-coincident mode and some coincident points are occurring, how can the actual coherence be calculated. In this situation, it is found that when these coincident points are removed from the non-coincident acquisition no change appears to occur in the actual coherence estimates. This implies that the observed differences between the actual coherence estimates from coincident and non-coincident data are not due to coincident points occurring during non-coincident acquisition.

4.3.4 Concluding Remarks

This section has examined the implications of acquiring LDA data in non-coincident and coincident mode. This analysis is useful to assess the differences that arise in the estimation of the Reynolds stress term $u'v'$, using both modes of acquisition. It has been shown that this Reynolds stress term is easily obtained from coincident data, when the random time series of $u'(t)$ and $v'(t)$ are combined. The process for obtaining this same term from non-coincident data involved combining the reconstructed time series $u'_r(t)$ and $v'_r(t)$.

The comparison of acquisition modes was applied to the velocity fluctuations and the Reynolds stress terms of u'^2 and v'^2. Slight spectral differences were observed which were due to varying mean data acquisition rates. The study of the $u'v'$ term resulted in different spectral estimates from the two modes of acquisition. By obtaining coincident and non-coincident data with similar mean data acquisition rates enabled the elimination of errors associated with the filter correction to be made (as the data rates were constant the filter would be constant). The only difference in the spectral estimates occurred at low frequencies, which may suggest a velocity bias. When the non-coincident time trace was examined, coincident data points were discovered. However these coincident points did not appear to have any significant effect on the coherence.

The influential parameters for this comparison would appear to be noise to signal ratios and the data rates. This concurs with the conclusions of Fitzpatrick & Simon [41] in respect of inherent noise in LDA measurements. The auto spectrum of the velocity fluctuations and Reynolds stress terms u'^2 and v'^2 can be obtained from coincident or non-coincident data. However to correctly estimate $u'v'$ it is required that LDA data is acquired in coincident mode, until the low frequency bias associated with correction procedures can be eliminated. When this bias is addressed some coincident data points may still occur in non-coincident acquisition (especially for high data rates). This suggests that the Reynolds stress term $u'v'$ should therefore be estimated from coincident data.

Chapter 5

Acoustic Experimental Analysis

A series of acoustic measurements on a subsonic jet were performed using the open-jet facility described by Chatellier & Fitzpatrick [49]. The purpose of these tests was to determine if the noise generated by the jet could be registered by microphone measurements and to examine if the hydrodynamic and acoustic regions of the jet could be identified and hence decisions made in respect of regions of interest for combined LDA and microphone measurements.

As detailed in chapter 2 the pressure fluctuations associated with the unsteady Bernoulli equation can be divided into hydrodynamic fluctuations and acoustic fluctuations. Arndt et al [16] defined the demarcation between the hydrodynamic and acoustic regions to be proportional to the wavenumber (k) and the radial position of the measurement device relative to the shear layer axis (R). In this regard the hydrodynamic region occurs for $0 < kR < 2$ and the acoustic region for $kR > 2$. This kR parameter enables the acoustic region of a jet to be examined much closer to the jet axis than was previously thought.

The experimental setup as shown in figure 5.1 was carried out on an open-jet where the inlet flow was generated by a 5.5kW centrifugal fan. This air flow was channelled through wire meshes and honeycomb into a plenum chamber as illustrated in figure 5.2. Through a bell-mouth elliptic cross section the jet discharged the air at velocities from $U_0 \simeq 30$ to $83m/s$ ($R_D \simeq 10^5$ to $2.8\text{x}10^5$).

Seeding was introduced to the jet flow in order to perform the LDA measurements, this was provided by an Antari Z300 fog generator. Particles of approxi-

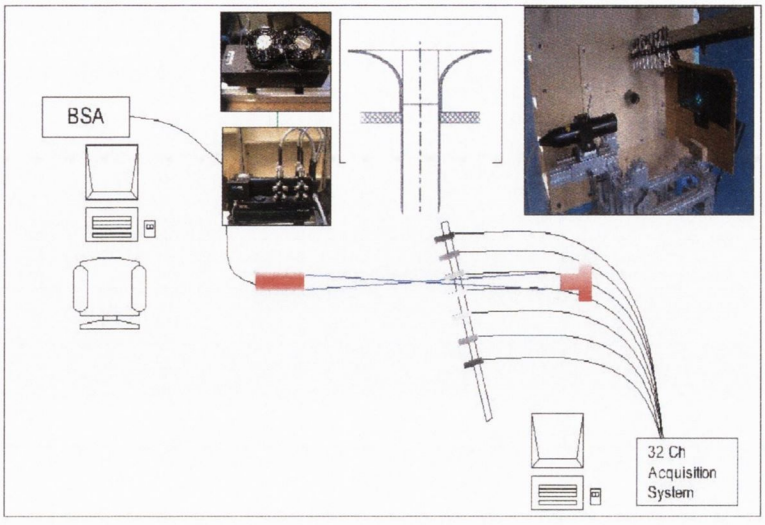

FIGURE 5.1: *Schematic of experimental setup*

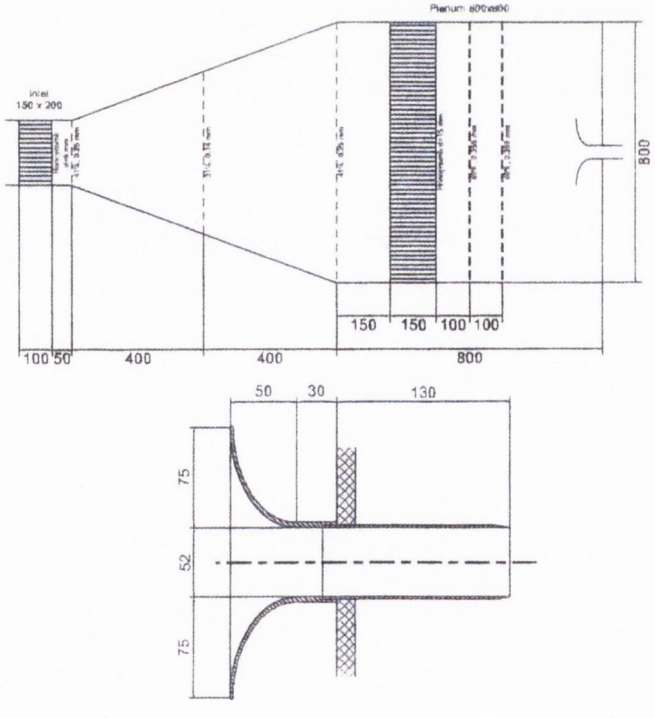

FIGURE 5.2: *TCD Jet (Chatellier & Fitzpatrick [49])*

mately $1\mu m$ were added at the centrifugal fan inlet. The LDA head was mounted on a traverse to achieve movement in both the axial and radial directions. The forward scatter camera was also mounted on this rig so as to maintain volume focus throughout testing.

The axial and radial velocity profiles are shown in figure 5.3. For these profiles it can be seen that the potential core length for this jet can be estimated to be $6D$ and there appears to be a slight deviation of the potential core along the center axis. This is also confirmed from the turbulence intensity, figure 5.3 (c), where a bias towards the positive y-direction is evident.

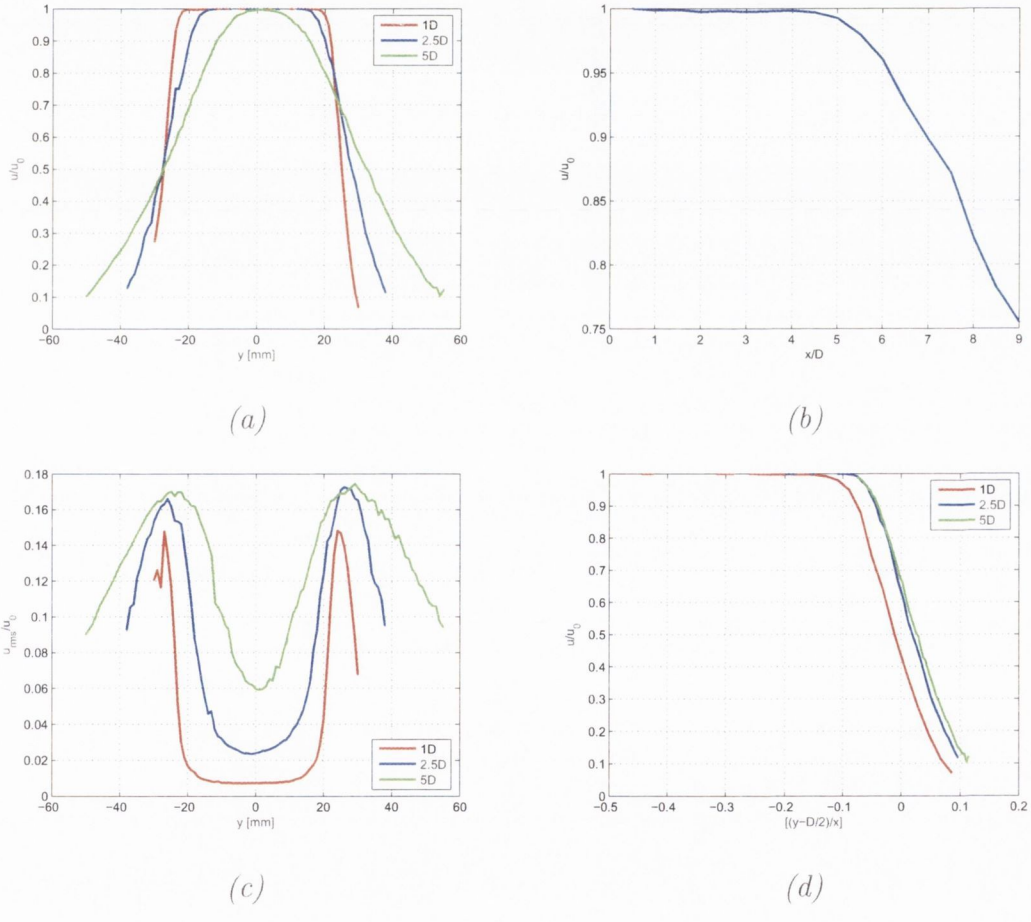

FIGURE 5.3: *Jet Profile (a) Radial velocity profile, (b) Potential Core length, (c) Turbulence Intensity profile, (d) Self-Similarity Axial Profile*

The microphones were acquired at a rate of 25kHz over a ten second range. In

order to acquire synchronized measurements between the LDA and microphones an additional channel was acquired. This channel recorded when the LDA system acquired its first and last data point. This time trace was then used to extract the correct microphone data from the ten second acquisition. The LDA data was acquired for six seconds with the parameters for record length, bandwidth and voltage were altered depending on test and laboratory conditions. No filters were initially applied to the acquired data. On implementing Sample & Hold on the LDA data, the time trace was divided into a number of blocks, typically applying 100 averages. The number of points in each block was dependant on the mean data acquisition rates.

To achieve acoustic measurements that were not contaminated by outside noise, for example by the centrifugal fan, numerous precautions were taken. The test area was enclosed on both sides and above and below the jet without causing interference with the jet exhaust and foam wedges were placed on the ground to prevent reflection. If any unusual peaks occurred in the microphone trace, tests were repeated to ensure repeatability and avoid possible environmental noise contamination.

The acoustic measurements were obtained using 10 Senhauser Electrotet quarter inch microphones. The microphone array, as illustrated in figure 5.4 was positioned parallel to the outer shear layer axis. The closest position of the array, relative to the jet axis, was $r/D = 1.1$ (which corresponds to the distance of the first microphone to the jet axis). This is the closest that the array could be positioned to avoid measurement saturation. The axial position of the microphones is presented in table 5.1. This somewhat irregular microphone positioning was implemented in order to enable conditioning of exit effects if required.

Microphone 1 is positioned inline with the jet exit while the remaining microphones are positioned approximately $6D$ downstream at the end of the potential core of the jet at intervals of $34mm$. Measurements were performed with the array positioned at $r/D = 1.1$, 2.0, 3.0 and 4.5 for two jet velocities of $83m/s$ & $40m/s$. In the following sections the results obtained from the acoustic array positioned at $r/D = 1.1$ & 4.5 with the jet operating at maximum velocity (i.e.

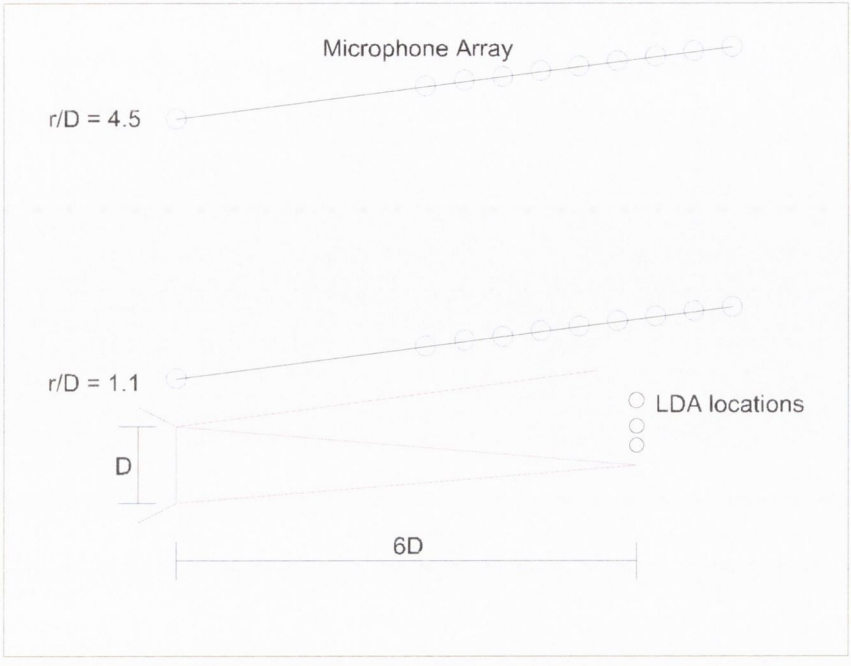

FIGURE 5.4: *Schematic of experimental setup*

Microphone	Axial Position /D
1	0
2	4.67
3	5.34
4	6.01
5	6.68
6	7.34
7	8.01
8	8.68
9	9.35
10	10.02

TABLE 5.1: *Axial microphone positions*

83m/s) are presented.

5.1 Configuration 1 ($r/D = 1.1$)

Measurement of the acoustic region of a jet is dependent on two factors, namely, the position of the measuring device relative to the shear layer axis and the wavenumber. In this respect a large r/D is necessary while for $r/D = 1.1$ it is expected that the measured data will mainly relate to the hydrodynamic region of the jet.

5.1.1 Auto Spectra

With $r/D = 1.1$, the auto spectra of all ten microphones is shown in figure 5.5 (a) as a function of frequency, and in, 5.5 (b) as a function of kR_j. It can be seen

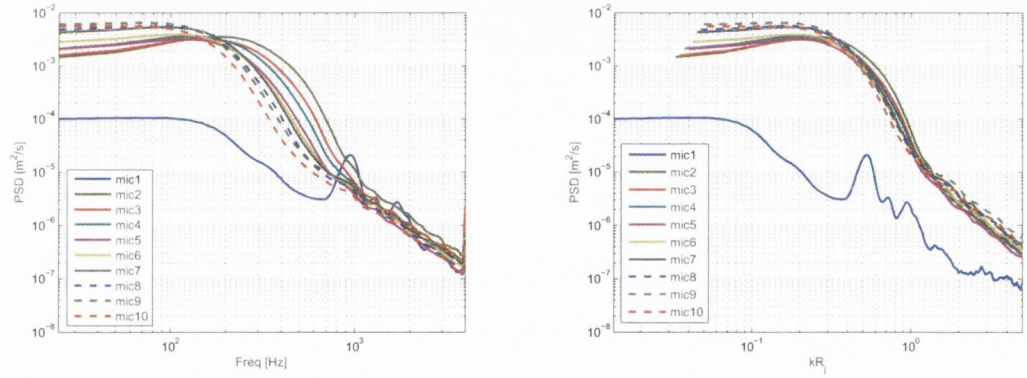

(a) *(b)*

FIGURE 5.5: $r/D = 1.1$: *Auto Spectra for Microphones as a function of* (*a*) *frequency* (*b*) kR_j

clearly that the auto spectrum of microphone 1 is different from the others. From the frequency domain, this spectrum has a peak at approximately $1000Hz$. Other peaks are observed at 1200 & $1900Hz$ whereas the spectra of microphones $2-10$ do not have similar characteristics. This suggests that microphone 1, positioned at the jet exit, is measuring some 'additional extraneous noise'. When the auto

spectra are plotted as a function of kR_j (figure 5.5 (b)), the peaks observed in the auto spectrum of microphone 1 occur for $kR < 2.0$ implying that the observed extraneous noise is within the hydrodynamic region. As stated earlier, measurement of the acoustic region required a large r/D. Notwithstanding, figure 5.5 (b) indicates some measurement of this phenomenon when $r/D = 1.1$.

Although the observed extraneous noise appears to be present only in the immediate area surrounding the jet exit, it was deemed necessary to eliminate this as a possible source of contamination that might effect the downstream measurements. When the coherence between microphone 1 (at the jet exit) and all other microphones is examined, as shown in figure 5.6, it can be seen that the observed extraneous noise is partially coherent with the downstream microphones, particularly at frequencies of $1000, 1200$ and $1900Hz$. When the extraneous noise

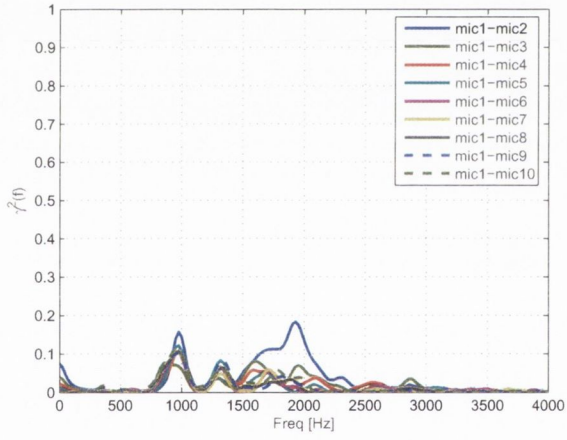

FIGURE 5.6: *Coherence between microphone* 1 *and all other microphones at* $r/D = 1.1$

is conditioned out, by removing the coherent part between microphone 1 and the remaining microphones from the auto spectra of microphones $2-10$, the resulting auto spectra are shown in figure 5.7 (a), as a function of frequency, and in, 5.7 (b) as a function of kR_j. When the conditioning is applied very little noticeable difference is observed, suggesting that, even with the extraneous noise being present, the jet noise is still dominant at the end of the potential core.

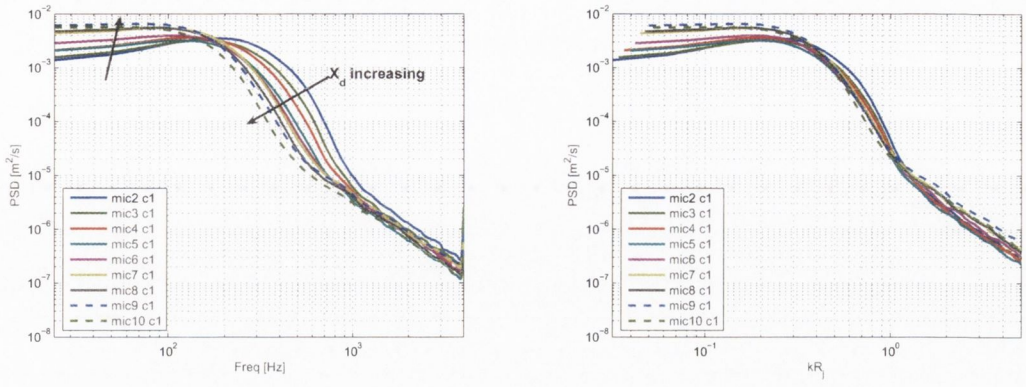

(a) *(b)*

FIGURE 5.7: $r/D = 1.1$: *Auto Spectra for Microphones conditioned using microphone* 1 *as a function of* (*a*) *frequency* (*b*) kR_j

5.1.2 Coherence

The use of the microphone array allows for identification of the hydrodynamic and acoustic regions of the jet. An examination of the coherence between each individual microphone and all other microphones enables the coherence decay within a region to be observed. Figure 5.8 (a) & (c) shows the coherence between both microphone 2 and microphone 7 with the microphones located downstream. These coherences were then conditioned for the extraneous noise, and are shown in 5.8 (b) & (d). Some differences are noted. In particular at the frequencies where the extraneous noise between microphone 1 and the remaining downstream microphones, are coherent, as seen by figure 5.6. From figure 5.8 two distinct regions of decay occur. The first between 0 and approximately $800Hz$, where the region is highly correlated. The second region occurs at frequencies above $800Hz$. Here the region is less correlated with increasing distance between the microphones. The sudden drop off in coherence between the regions can only be due to the existence of a local interference node, indicating a highly coherent mechanism, as observed by Jordan et al [17].

The demarcation between the hydrodynamic and acoustic regions, as previously detailed, is dependent on wavenumber and frequency. Arndt et al [16]

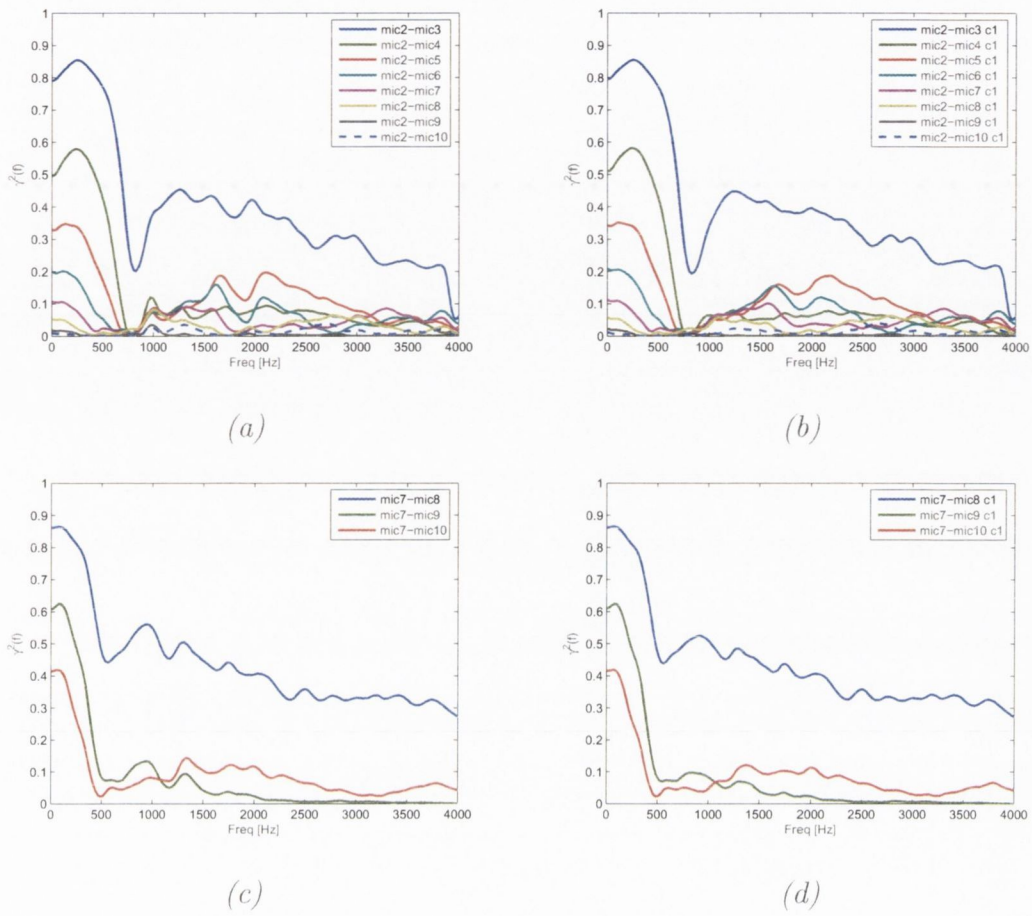

FIGURE 5.8: $r/D = 1.1$: *Coherence between microphones as a function of frequency - (a) & (c): no conditioning applied, (b) & (d): conditioning for microphone* 1 *applied*

showed this to be $kR = 2.0$. Examination of the coherence as a function of kR_j, shown by figure 5.9 reveals this demarcation very well. However it appears that the measured hydrodynamic region occurs for $0 < kR < 1.2$, with the acoustic region occurring for $kR > 1.2$. Both the unconditioned and conditioned case are illustrated.

In order to further understand this demarcation and the difference in coherence decay between regions, the propagation of coherence moving downstream with the microphones was examined. Figure 5.10 shows this, as a function of (a) frequency but, more importantly, (b) as a function of kR_j. Figure 5.10 (b) shows

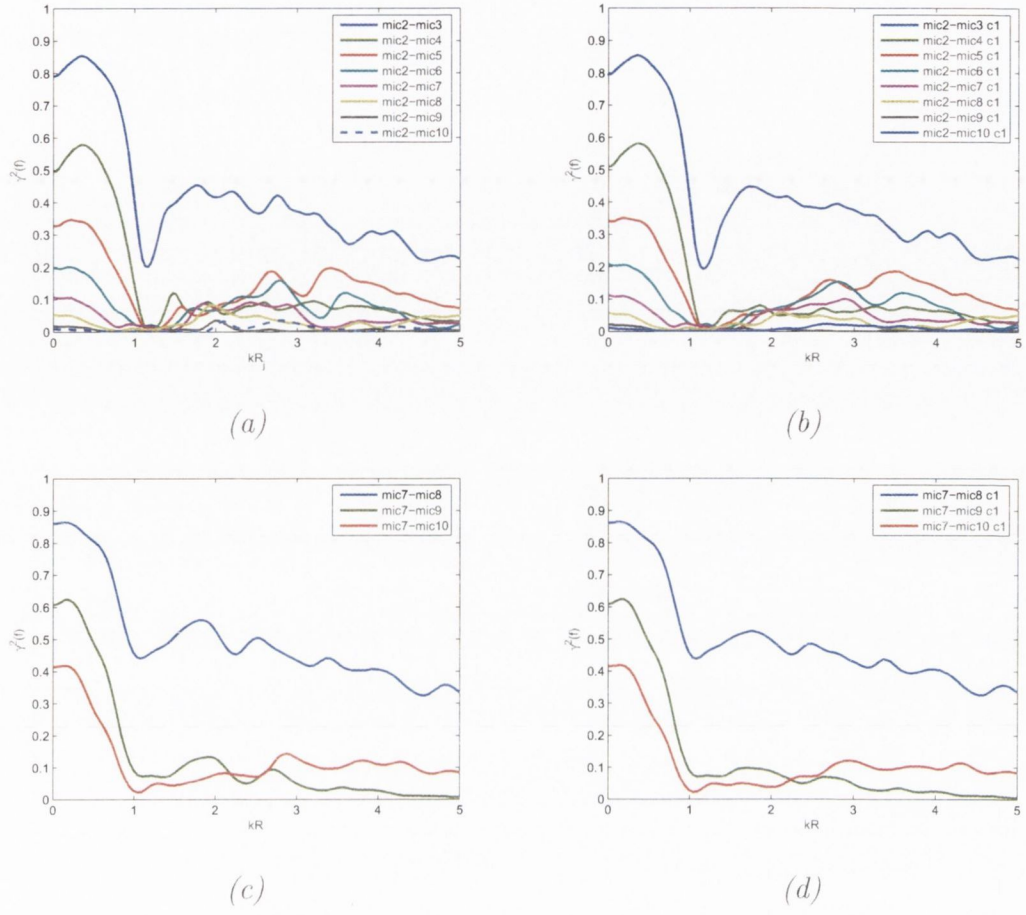

FIGURE 5.9: $r/D = 1.1$: *Coherence between microphones as a function of* kR_j *- (a) & (c): no conditioning applied, (b) & (d): conditioning for microphone* 1 *applied*

that the coherence in the hydrodynamic region ($kR < 1.2$), which comprises plane waves convecting perpendicular to the shear layer axis, appears to be highly correlated over all microphone locations and would seem to act as a single oscillating unit, as reported by Jordan et al [17], while in the acoustic region ($kR > 1.2$), the coherence increases in the downstream direction with the greatest coherence occurring between microphones 6 & 7. The nature of wavenumber examination is similar to Strouhal number examination, where a collapse of data is expected. Figure 5.10 (b) reveals a slight increase of the demarcation with the downstream direction. The velocity profile of this jet is such that it is biased in the upwards

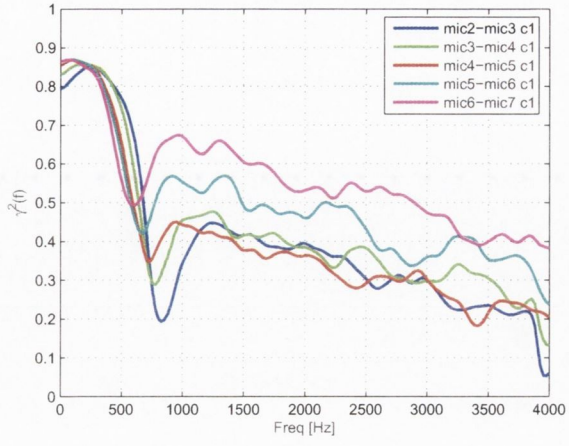

(a)

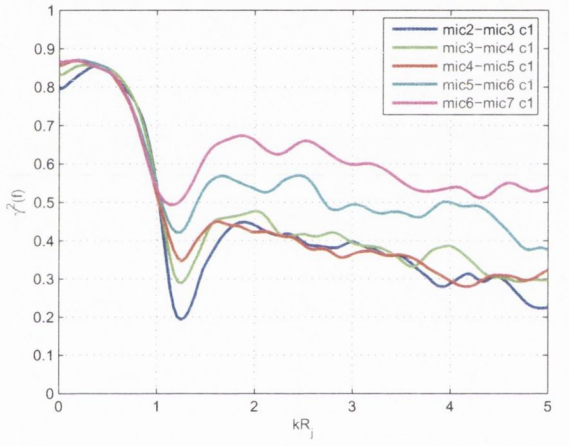

(b)

FIGURE 5.10: $r/D = 1.1$: *Microphone Coherence as a function of* (*a*) *frequency* (*b*) kR_j

direction, suggesting that the measured radial distance between the microphones and the shear layer axis are over estimated, which would account for the observed increase in demarcation.

This observed difference in coherence decay between the regions is due to the lower frequencies in the hydrodynamic region (the energy region) being associated with larger turbulence scales and these larger scales are correlated over a much greater distance. Furthermore, downstream of the potential core, sources

behave more like a single source mechanism due to the dominance of the column instability, as suggested by Jordan et al [17].

To further illustrate this demarcation the coherence between all microphones is presented in the form of contour plots, where the x-axis is the axial distance from the jet exit and the y-axis is the wavenumber term kR_j. Figure 5.11 illustrates the contour coherence and figure 5.12 the conditioned contour coherence. In both

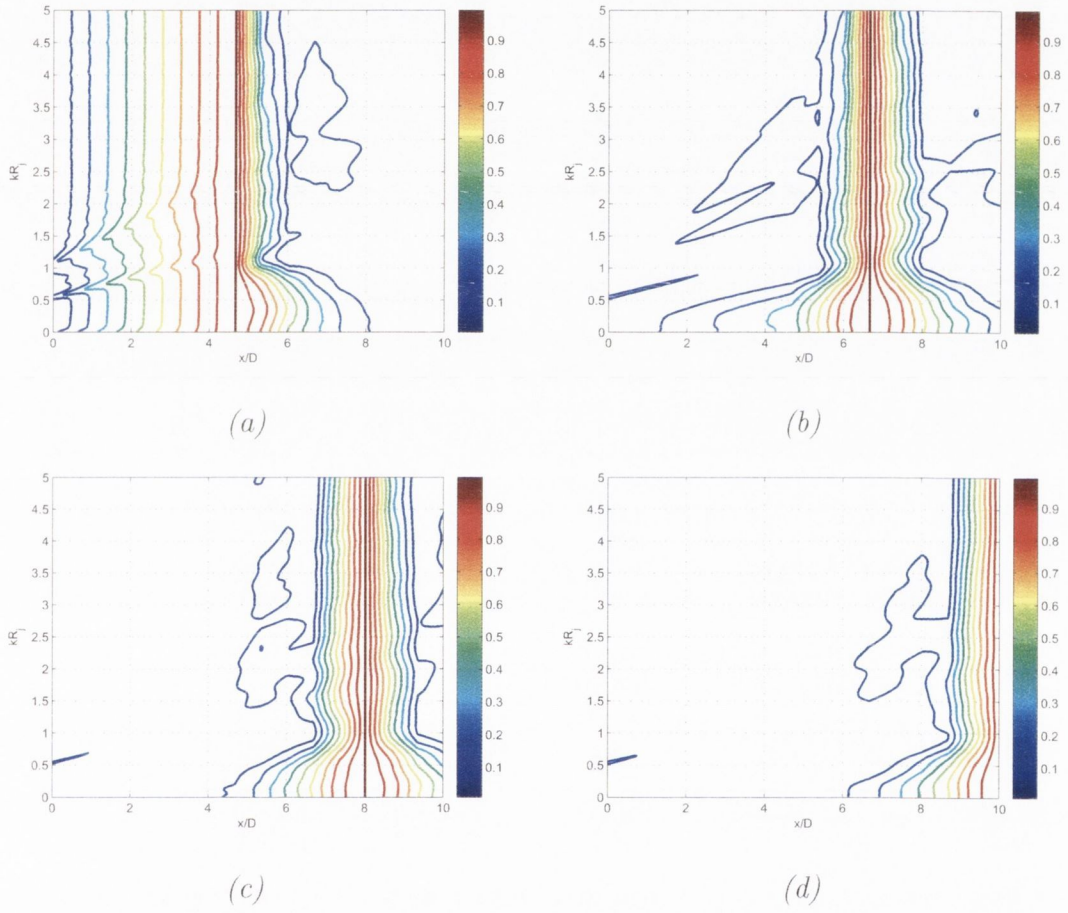

FIGURE 5.11: $r/D = 1.1$: *Contour Coherence with reference microphone (a) 2, (b) 5, (c) 7, (d) 10*

of these figures the reference microphones are $2, 5, 7, \& 10$, with a straight vertical line indicating the coherence of each microphone with itself (i.e. a coherence of one). Some small differences are seen when the effect of the extraneous noise, as measured by microphone 1, is conditioned out of the coherence. This reaffirms

that the extraneous noise is only affecting the immediate area surrounding the jet exit. The demarcation between the hydrodynamic and acoustic regions is also

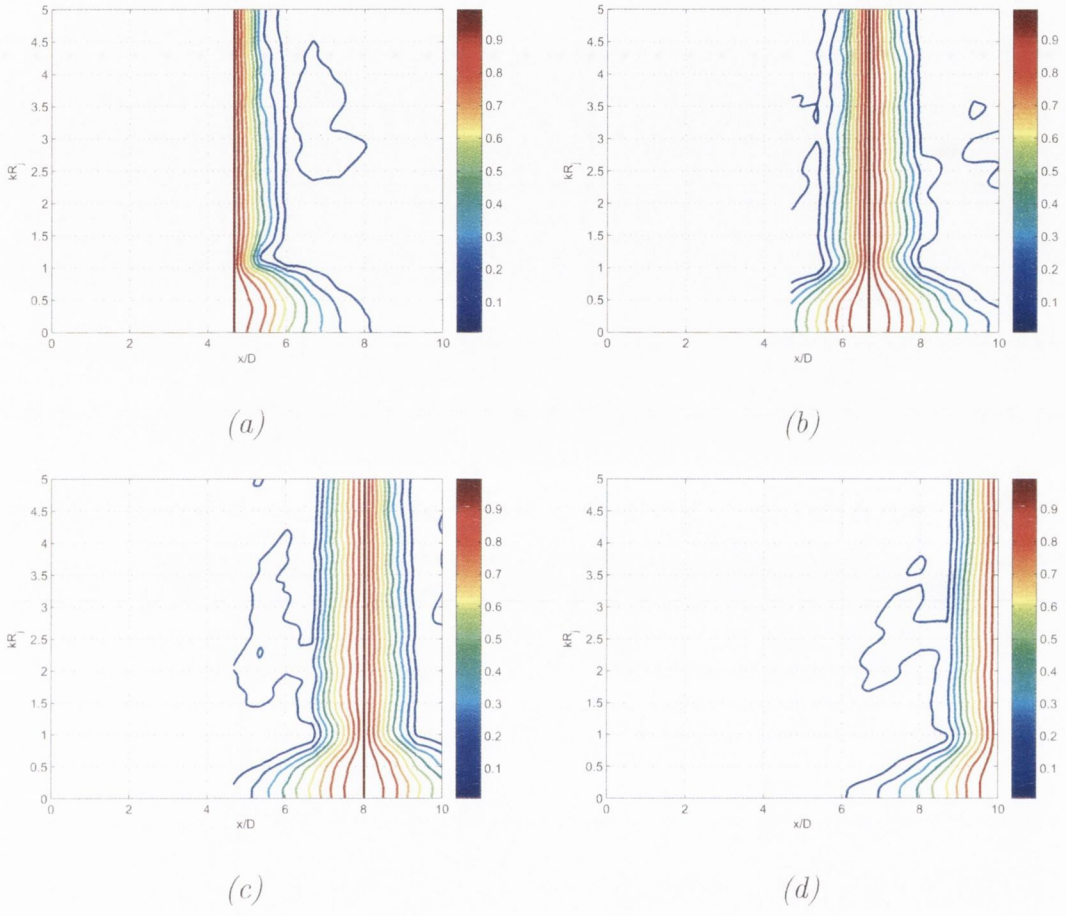

FIGURE 5.12: $r/D = 1.1$: *Contour Coherence conditioned for microphone* 1 *with reference microphone (a) 2, (b) 5, (c) 7, (d) 10*

evident. As previously noted for $kR < 1.2$ the hydrodynamic region is seen to be more coherent over a greater distance compared to that for $kR > 1.2$. The observed shape and demarcation as seen by the contour coherence agrees with those presented by Jordan et al [17].

5.1.3 Phase

The relationship of the foregoing, with respect to phase, is now analysed. Figure 5.13 illustrates the phase calculated between both microphones 2 and 7 with the

remaining downstream microphones. For completeness, the conditioned and unconditioned cases are considered. As can be seen from figure 5.13, the previously observed extraneous noise does not affect the phase estimates.

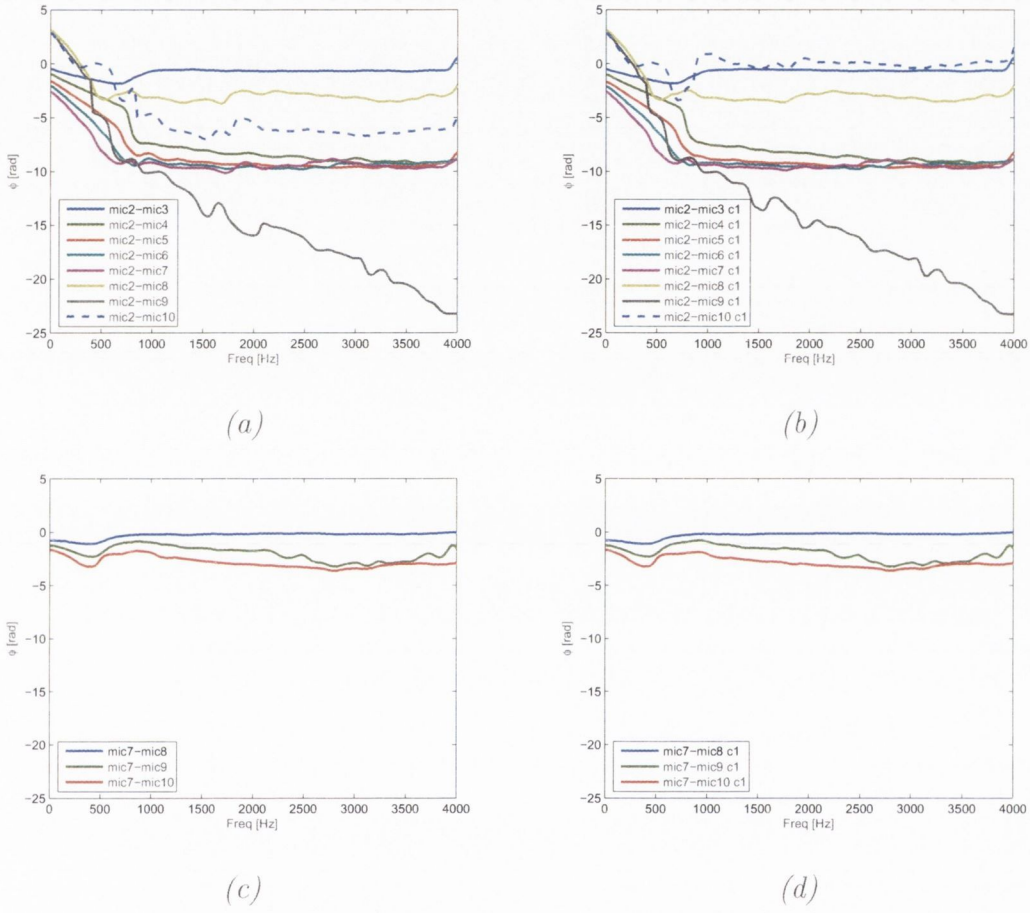

FIGURE 5.13: $r/D = 1.1$: *Microphone Phase as a function of frequency - (a): no conditioning applied, (b): conditioning for microphone* 1 *applied*

Two distinct regions were previously noted from the coherence estimates. These two regions are also seen in the phase estimates. In this respect, figure 5.14 illustrates the phase as a function of the wavenumber term kR_j, where the demarcation is once again clearly evident.

A similar decomposition to the coherence propagation, previously performed, is applied to the phase estimates. Figure 5.15 illustrates this as a function of, (a) frequency, and, (b) kR_j. Here the demarcation between regions is very ob-

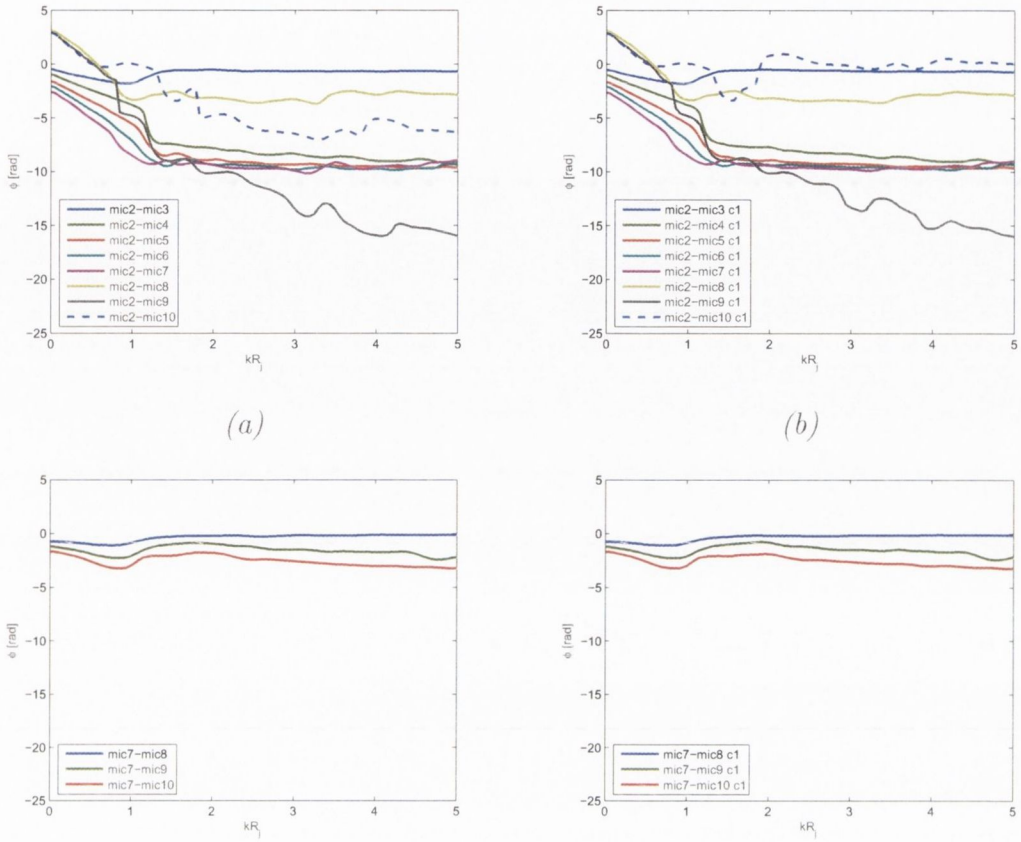

FIGURE 5.14: $r/D = 1.1$: *Microphone Phase as a function of* kR_j - *(a) & (c): no conditioning applied, (b) & (d): conditioning for microphone* 1 *applied*

vious. These results confirm, as would be expected for $r/D = 1.1$, that the hydrodynamic region is convecting while the acoustic region is propagating.

As mentioned convection velocities can be obtained from phase estimates, an example of this is shown in figure 5.16. Where the convection velocity is calculated from the phase between microphone 2 and microphones $3 - 7$, over a frequency range of $0 - 500Hz$. This represents the convecting velocity of the hydrodynamic waves where an obvious increase with frequency is seen.

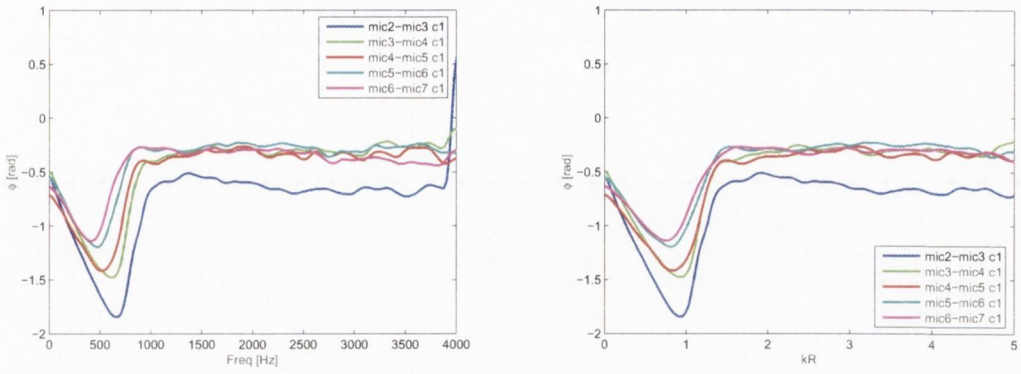

(a) (b)

FIGURE 5.15: $r/D = 1.1$: *Microphone Phase as a function of* (a) *frequency,* (b) kR_j

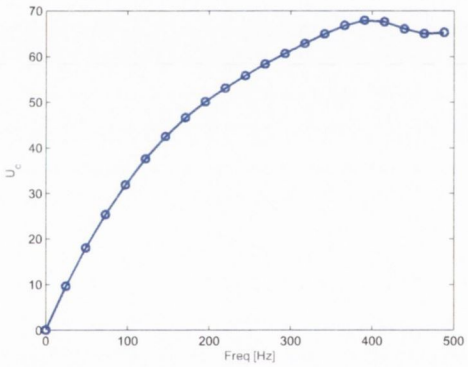

FIGURE 5.16: $r/D = 1.1$: *Convection velocity as a function of frequency*

5.2 Configuration 2 ($r/D = 4.5$)

With the microphone array positioned at $r/D = 1.1$ it was seen that both the hydrodynamic and acoustic regions of the jet were examined. In order to examine more of the acoustic region of the jet, and consequently less of the hydrodynamic region, the array must be located further in the radial direction to $r/D = 4.5$.

5.2.1 Auto spectra

For $r/D = 1.1$, it was observed that the extraneous noise affected only microphone 1 which was positioned at the jet exit. As shown by figure 5.17 (a) as a function of frequency and (b) as a function of kR_j, with the array at $r/D = 4.5$ it can

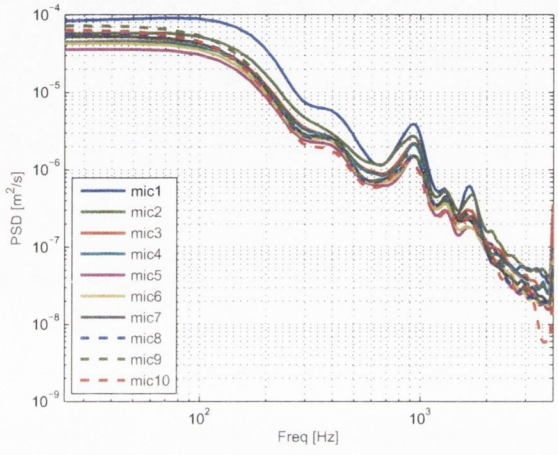

(a)

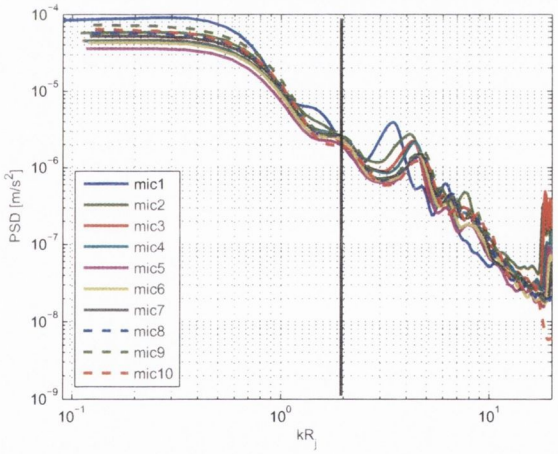

(b)

FIGURE 5.17: *$r/D = 4.5$: Auto Spectra for Microphones as a function of (a) frequency (b)* kR_j

be clearly seen that all ten microphones seem to measure this noise. When the array was positioned at $r/D = 1.1$ microphone 1 measured approximately $14dB$ for the hydrodynamic region, with the remaining downstream microphones

measuring between 40 and $49dB$. With the array positioned further in the radial direction it can be clearly seen that all microphones are measuring approximately $14dB$. With a relatively small increase in radial distance the noise levels have dramatically reduced.

An examination of the auto spectra as a function of the kR_j term reveals that this observed noise occurs predominantly in the acoustic region ($kR > 2.0$). In order to investigate further the possible origin of the extraneous noise, a laser vibrometer was used to measure vibration on the front panel of the wind tunnel, while simultaneously the microphones measured the jet noise. The coherence between the laser vibrations and microphone measurements is shown in figure 5.18 (a). For this analysis microphone 1 was positioned at $r/D = 1.1$ and microphones

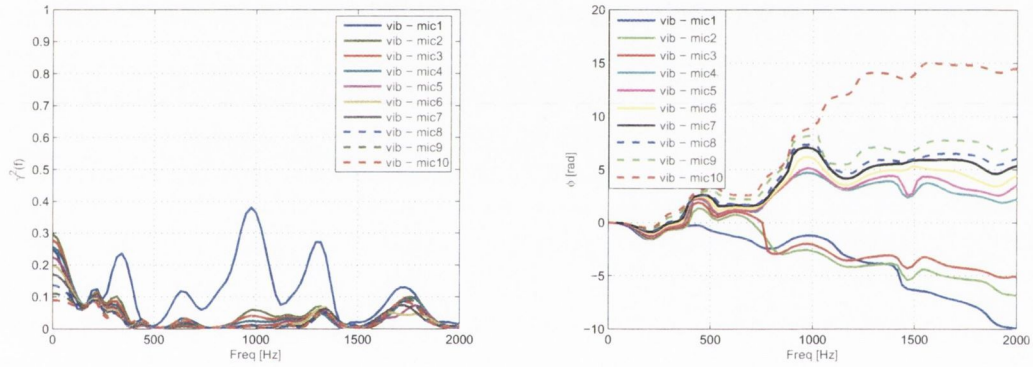

(a) *(b)*

FIGURE 5.18: *(a) Coherence between vibrations on wind tunnel with the microphone 1 positioned at $r/D = 1.1$ and the remaining microphones positioned at $r/D = 4.5$, (b) Phase between laser vibrometer and all microphones (mic1 positioned at $r/D = 1.1$, microphones $2 - 10$ positioned at $r/D = 4.5$*

$2 - 10$ at $r/D = 4.5$. This investigation reveals that the vibrations are partially coherent with the microphone measurements. The coherence is greatest with microphone 1, particularly at $200, 800, 1000, 1300$ & $1800Hz$. The remaining microphones, positioned downstream at $r/D = 4.5$, are also partially coherent with these vibrations at the same frequencies. The phase between the laser vibrometer and the microphones is shown in figure 5.18 (b). Propagation can be observed at

the frequencies where partial coherence between the vibrations and microphones occurred.

The auto spectra of the laser vibrometer and microphones 1 & 2 is shown in figure 5.19 (a). As mentioned the laser vibrometer was placed on the front panel of the wind tunnel and any vibrations present were measured. The diagram shows that there are clearly peaks in the vibration auto spectrum. These are also seen to occur in the auto spectra for microphones 1 & 2. It should be noted that the movement of the front of the plenum chamber altered throughout testing. Through numerous vibration laser tests it was concluded that the peaks seen in the microphone spectra were resulting from the movement of the front panel. Examination of the coherence between microphone 1 at $r/D = 1.1$ and the remaining microphones positioned downstream at $r/D = 4.5$, as shown by figure 5.19 (b), shows that the frequencies that were dominant in the vibration examination are also dominant here. This implies that some of the extraneous noise observed, by microphone 1 at $r/D = 1.1$ and, all ten microphones at $r/D = 4.5$, is due to the vibration of the front panel of the wind tunnel.

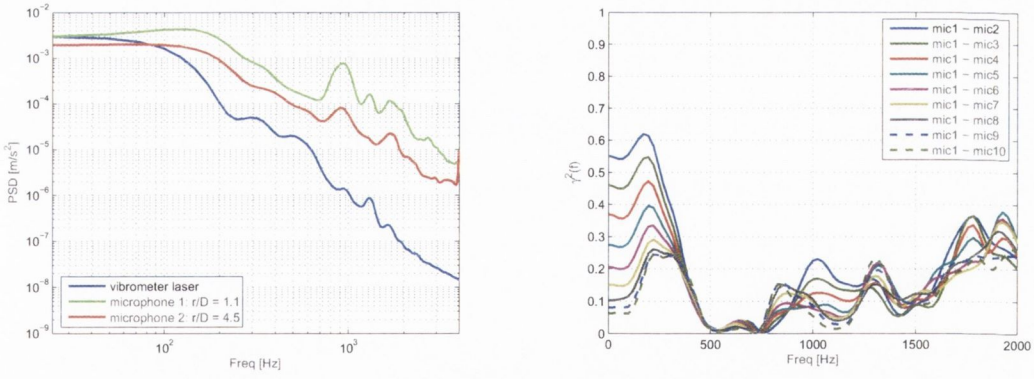

(a) *(b)*

FIGURE 5.19: *(a) Auto Spectra of vibrations on wind tunnel and microphone 1 (positioned at $r/D = 1.1$) (b) Coherence between microphone 1 (again $r/D = 1.1$) with the remaining microphones positioned at $r/D = 4.5$*

Returning to the configuration where all microphones are positioned at $r/D = 4.5$, the coherence between microphone 1 and the remaining downstream micro-

phones reveals some of these vibration frequencies previously noted, (see figure 5.20).

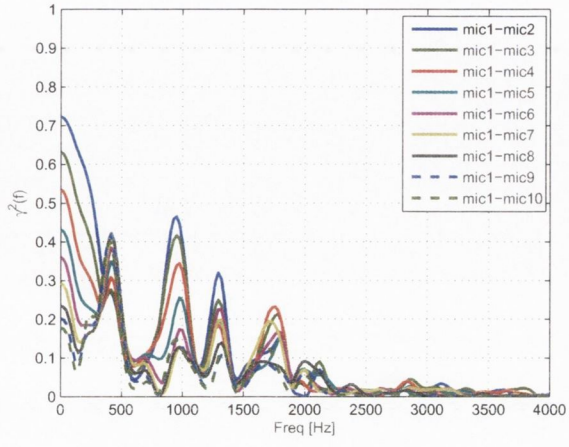

FIGURE 5.20: $r/D = 4.5$: *Coherence between Microphone* 1 *and all other microphones*

The auto spectra, conditioned for the extraneous noise, reveals little change while the observed peaks remain dominant in the acoustic region, as shown in figure 5.21.

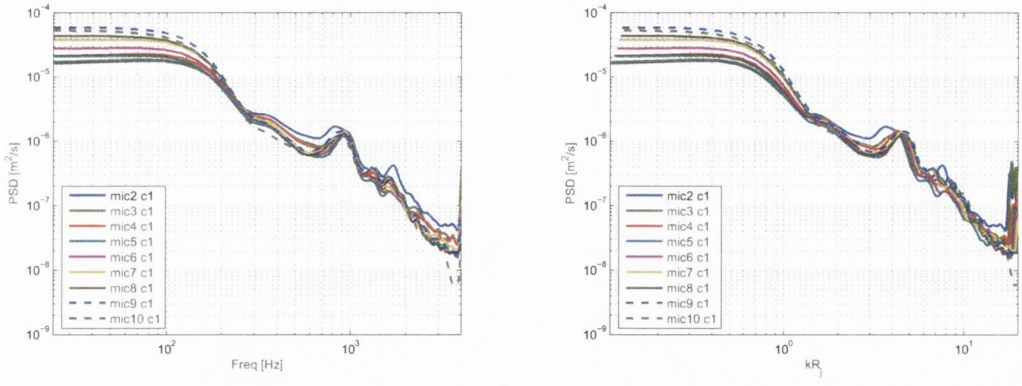

(a) *(b)*

FIGURE 5.21: $r/D = 4.5$: *Conditioned Auto Spectra for Microphones as a function of* (*a*) *frequency* (*b*) kR_j

5.2.2 Coherence

Examination of the coherence between the downstream microphones, (for example between microphone 2 and the remaining microphones as shown by figure 5.22), again reveals the presence of the extraneous noise. The unconditioned case

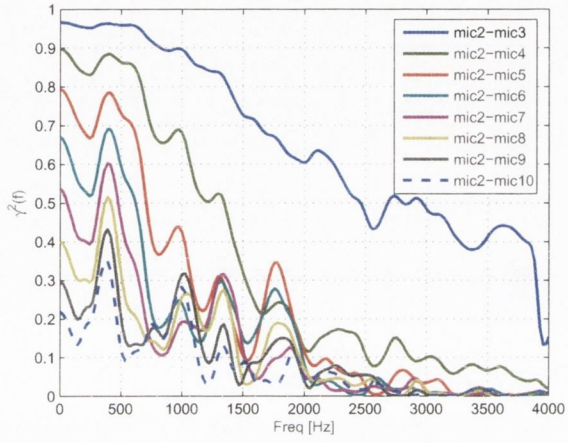

(a)

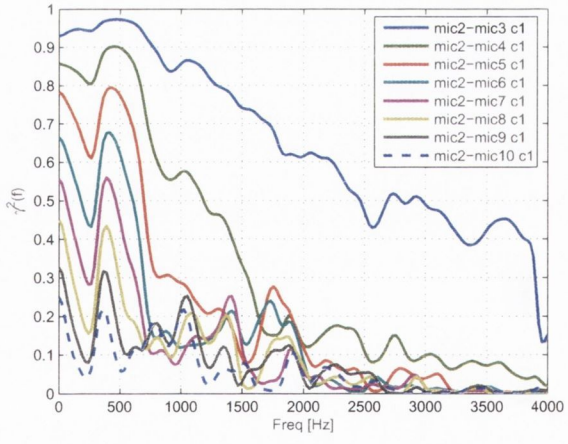

(b)

FIGURE 5.22: $r/D = 4.5$*: Coherence between Microphone* 2 *and all other microphones* (*a*) *No conditioning applied* (*b*) *Conditioning applied (removing the effect of microphone one)*

5.22 (a) and conditioned case 5.22 (b) are illustrated. While some decrease in coherence is noted at the dominant vibration frequencies with the removal of

the extraneous noise the overall change is not significant enough to eliminate the vibrations entirely.

In order to examine the propagation of the acoustic waves, the coherence between microphones $2-3, 3-4, 4-5, 5-6$ and $6-7$ is analysed. Figure 5.23 (a), as a function of frequency, and, 5.23 (b), as a function of kR_j illustrate that

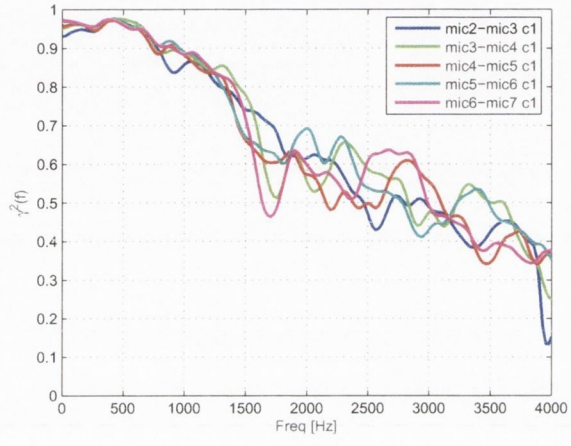

(a)

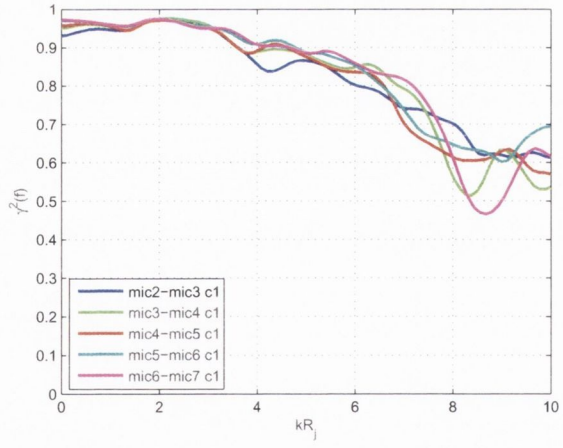

(b)

FIGURE 5.23: $r/D = 4.5$: *Coherence between Microphones as a function of* (*a*) *frequency* (*b*) kR

all microphones would seem to be measuring an area which is highly correlated in both the hydrodynamic and acoustic regions. The behaviour of the acoustic

region as measured at $r/D = 4.5$ is very different to that seen at $r/D = 1.1$ since no increase in coherence with the downstream direction is noted.

To determine if the demarcation between regions can be observed, the contour coherence is examined, as shown in figures 5.24 (unconditioned) and 5.25 (conditioned). The reference microphones are again 2, 5, 7, and 10. As noted previously, the conditioned coherence results in little change. Consequently there appears to be a division comprising two regions in the contour coherence. Nonetheless the demarcation would seem to be at $kR_j = 10$.

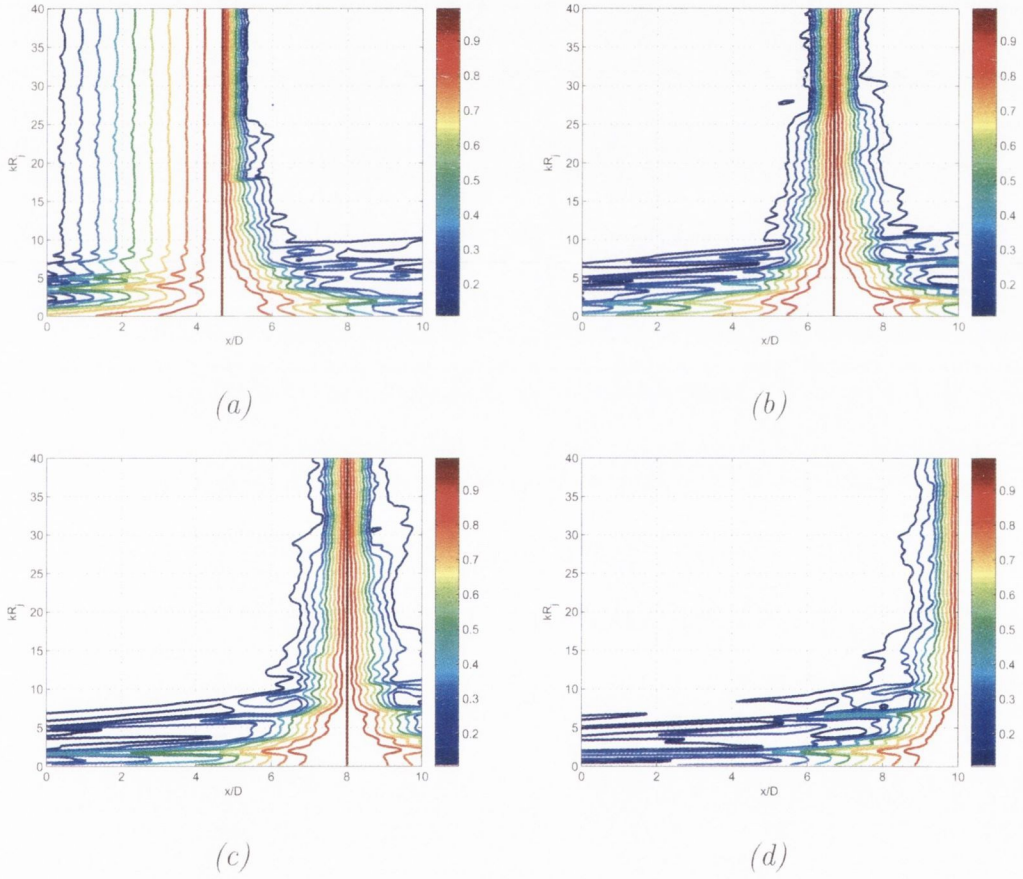

FIGURE 5.24: $r/D = 4.5$: *Contour Coherence with reference microphone (a) 2, (b) 5, (c) 7, (d) 10*

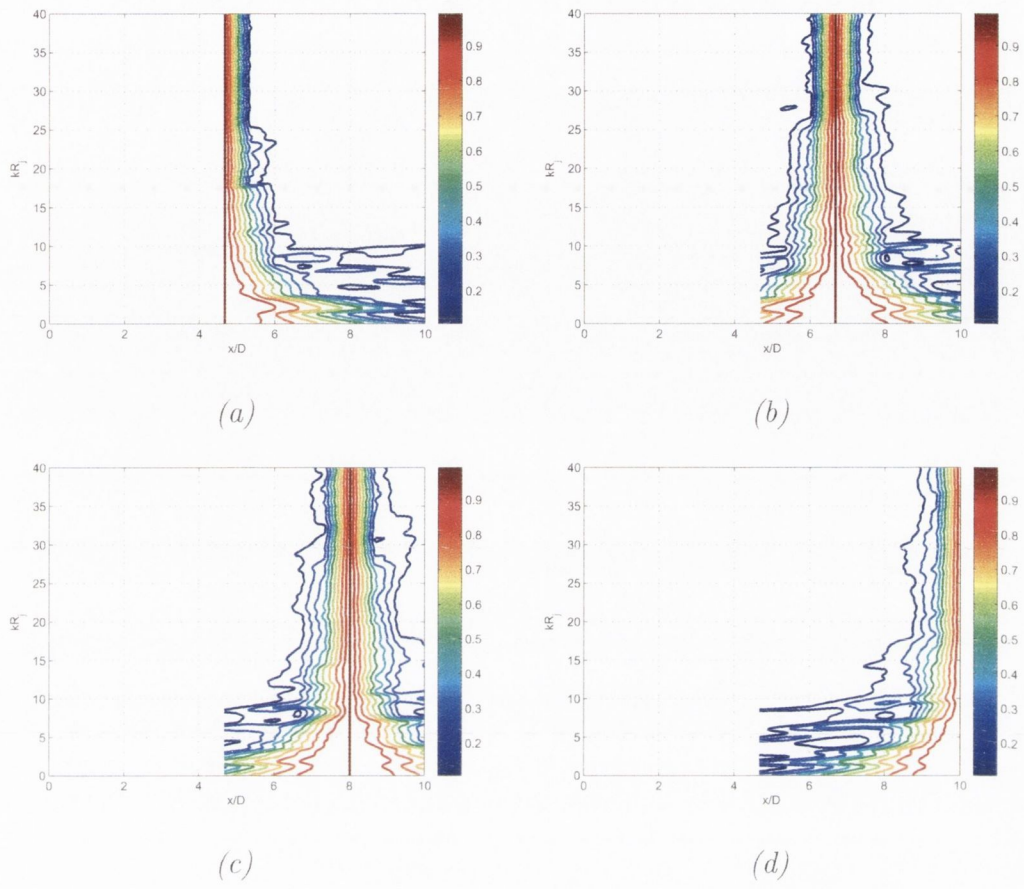

FIGURE 5.25: $r/D = 4.5$: *Contour Coherence conditioned for microphone* 1 *with reference microphone (a) 2, (b) 5, (c) 7, (d) 10*

5.2.3 Phase

As previously mentioned and shown by figure 5.13, the phase estimates are not affected by the extraneous noise. Figure 5.26 illustrates the phase between microphones 2 and 7 with the remaining downstream microphones as a function of (a) & (c) frequency and (b) & (d) kR_j. The demarcation between regions is again somewhat uncertain. However when the propagation of the phase is examined, particularly for the acoustic region, as shown by figure 5.27, it would seem to suggest that the sources being registered by these microphones are propagating past them. Therefore it would appear that in fact the acoustic region is being measured for this particular r/D. To extract source propagation velocities will

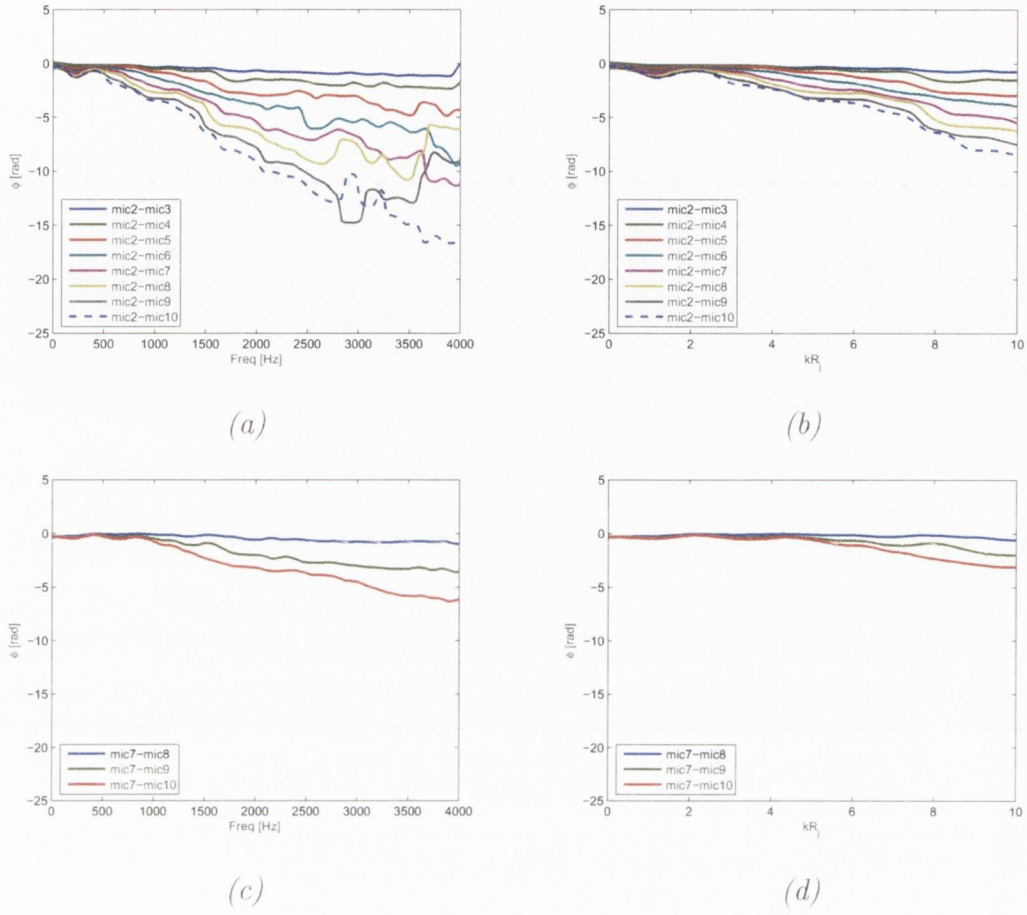

FIGURE 5.26: $r/D = 4.5$: *Microphone Phase - (a) & (c): function of frequency, (b) & (d): function of* kR

require careful analysis so as to avoid the observed vibrations that are contaminating the acoustic field.

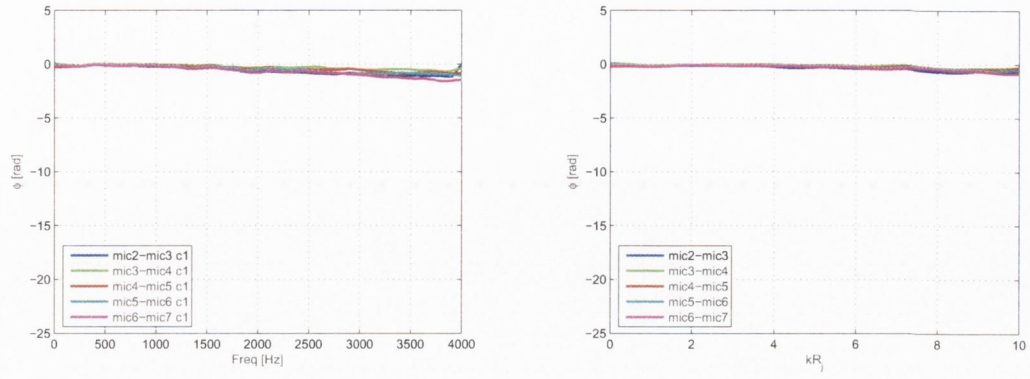

(a) *(b)*

FIGURE 5.27: $r/D = 4.5$: *Phase between Microphones as a function of* (*a*) *frequency* (*b*) kR

5.3 Concluding Remarks

The primary aim of this experimental acoustic analysis was to determine if the acoustic region of the jet could be successfully measured. As was shown by Arndt et al [16], in order to measure the acoustic region of a jet, the position of the measuring device is dependant not just on the radial distance from the shear layer axis but also on frequency. The term 'kR' evolved to describe the demarcation zone between the hydrodynamic and acoustic regions. The foregoing acoustic analysis was performed from measurements obtained at two microphone array locations ($r/D = 1.1$ & 4.5) with the jet operating at maximum velocity (i.e. $83m/s$).

The close array position of $r/D = 1.1$ enabled both the hydrodynamic and acoustic regions of the jet to be examined. The microphones were configured so that microphone 1 was located inline with the jet exit and the remaining nine microphones were located near the end of the potential core of the jet, approximately $6D$ downstream. The array was placed parallel to outer shear layer axis.

It was observed that some additional noise was measured at the jet exit. This noise was partially coherent with the downstream microphones, but had little, if

any, overall effect on coherence and phase estimates. This implied that the jet noise was dominating the observed contaminating noise for $r/D = 1.1$.

Examination of the coherence between the microphones revealed the point of demarcation between the hydrodynamic and acoustic regions of the jet. The hydrodynamic field, which comprises plane waves convecting perpendicular to the shear layer axis, was highly correlated over all microphones. The nature of noise generation in jets is such that the region at the end of the potential core and on the shear layer axis is where most mixing occurs. Hence it is here that most noise occurs. This was clearly shown when the acoustic field increased in the downstream direction from the end of the potential core, and onwards. The demarcation between regions was again evident from the phase estimates. When plotted as a function of wavenumber (kR), the phase clearly showed that for $kR < 1.2$ the hydrodynamic field was convecting and, for $kR > 1.2$ the acoustic field was propagating, as reported by Arndt et al [16] and Jordan et al [17].

In order to observe the expanding acoustic region of the jet, the array was positioned further from the jet axis to a position with $r/D = 4.5$. The contaminating noise previously observed at the jet exit was now radiating outwards as detected in all microphone measurements. The coherence between microphone 1 (positioned at the jet exit) and the remaining microphones located downstream at the end of the potential core revealed that this noise was correlated over the entire field, in the frequency range of interest to this study. When conditioning was applied to the data, very little appreciable difference resulted. The demarcation between the hydrodynamic and acoustic regions was not clearly identifiable with no increase in the acoustic field being noted in the downstream direction. The phase estimates revealed propagation occurring, however it appears that with the array positioned at $r/D = 4.5$ the extraneous noise and not the jet noise was dominating the measurements.

The remaining microphone array positions, namely $r/D = 2.0$ & 3.0, provided similar findings to those obtained at $r/D = 4.5$. When the jet was operated at a reduced velocity of $45m/s$ no further insight was obtained than when operating at maximum speed. Finally in an attempt to increase the jet velocity and hence the

jet noise, the exit nozzle was reduced to a diameter of $26mm$. This smaller nozzle only provided an increase of $5m/s$ in the exit velocity which was not significant enough to increase the jet noise to a dominant level.

Chapter 6

Source Identification

The preceding chapters have dealt with the correction procedures associated with the reconstruction technique of Sample & Hold, and the comparison of this technique to Slot Correlation. The LDA acquisition modes of coincident and non-coincident were also examined in relation to the velocity fluctuations, and, more importantly in relation to the Reynolds stress terms. Subsequently acoustic measurements were performed on the wind tunnel at Trinity College where the noise footprint of the jet was examined. All of this information will be utilized in this chapter to perform source identification of the jet using combined LDA and acoustic measurements.

LDA and acoustic measurements are used to perform detailed analysis relating to the propagation of the source terms u', v', u'^2, v'^2 & $u'v'$ to ten microphones positioned parallel to the shear layer axis. The correlation between u' & u'^2 and v' & v'^2 indicates the degree of quadratic interaction present in velocity data. The relationship between u' & v' and the microphones are termed linear source terms, whereas the relationship between u'^2 & v'^2 and the microphones are quadratic sources.

The aim of combined LDA and acoustic measurements was to identify the noise source mechanisms and examine their propagation and radiation within the area surrounding the jet. This chapter is divided into three sections. The first deals with the method used to extract information from five sources in conjunction with a number of microphones. The second details the measurement setup while

the third presents the results obtained.

6.1 Five Input Model

In order to provide a greater insight into the generation of noise it is necessary to obtain data from the LDA and microphones measurements and identify possible sources of noise. In a study of jet noise it is also important to extract this information from each noise source independently. This is necessary when correlation between input records exists. The technique used is detailed in Bendat & Piersol [50], where the relationship between each input and the output, with the mutual coherence between the inputs removed, is defined in equation 6.1.

$$G_{ij\cdot r!} = G_{ij\cdot(r-1)!} - \left[\frac{G_{rj\cdot(r-1)!}}{G_{rr\cdot(r-1)!}}\right] G_{ir\cdot(r-1)!} \tag{6.1}$$

Using this equation enables conditioned spectral quantities of order $r!$ to be calculated from known conditioned spectral quantities of order $(r-1)!$ for any $r = 1, 2, ..., q$ and i, j up to $(q+1)$, where $i > r$ and $j > r$.

The combined LDA and acoustic measurements will result in five inputs (u', v', u'^2, v'^2 & $u'v'$) and ten possible outputs (microphones $1-10$). Conditioned spectral analysis is achieved through the use of this simplistic model. Implementing a multiple input / single output model requires that the inputs are ranked according to the coherence with the output. This process cannot be applied to a multiple input / multiple output model, however an intelligent order is assigned to the inputs. The relationship between the inputs and each output is shown in figure 6.1. In order to extract the phase of the frequency response functions and work backwards to calculate $\{H_{iy}\}$ equations 6.2 & 6.3 are employed, for $i = (q-1), (q-2), ..., 2, 1$.

$$H_{qy} = L_{qy} \tag{6.2}$$

$$H_{ij} = L_{iy} - \sum_{j=i+1}^{q} L_{ij} H_{jy} \tag{6.3}$$

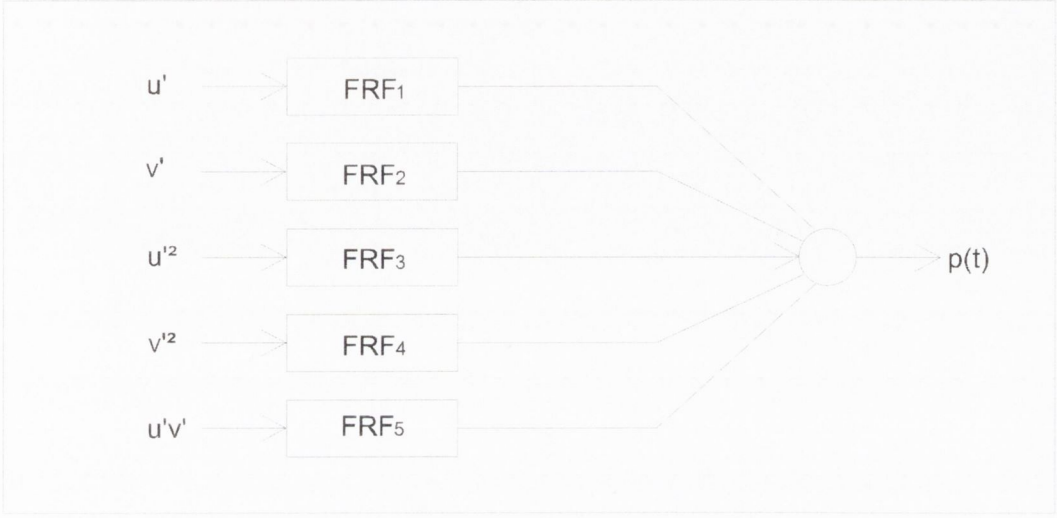

FIGURE 6.1: *Conditioned inputs & outputs*

The multiple-input output model detailed in Bendat & Piersol [50] was originally from a technique by Rice et al [51] which determined the nonlinear coefficients together with a physical model of the underlying linear structure that required excitation signals at each response location. This spectral technique is used for the identification of multiple degrees of freedom systems from input output records. Richards et al [52] compared their reverse path technique, which develops only one reverse path model from the entire set of N frequency domain, to that proposed by Rice et al [51]. They determined that the advantage of the technique of Rice et al was that the physical properties are identified however the application to a large number of degrees of freedom could be difficult. Whereas, their approach would be better suited to a large number of degrees of freedom. Roberts et al [53] used a generalised spectral estimation method similar to that proposed by Rice et al [51] where the addition of an equivalent white noise is used to model the unmeasured excitation. This modified approach overcomes the difficulty of separating linear and non-linear damping contributions using spectral methods and was applied to noise-free simulated data.

6.2 Experimental Setup

The use of the LDA system enables the velocity field to be measured non-intrusively and simultaneously with the acoustics so that the source mechanisms can be identified. The one-point/ two-component LDA system comprised of a Laser Physics $500mW$ Argon-ion laser (wavelengths of $488nm$ & $514.5nm$), a Dantec Fiberflow optical system operating in forward scatter, a Nikon camera and a burst spectrum analyser (BSA F50). This system produced a focal length of $250mm$ and a measurement volume of diameter $0.12mm$ and length $1.6mm$. The LDA and acoustic arrangement is shown in figure 6.2, where in this instance 10 microphones are mounted at an incline of approx 9 deg to the jet axis the first of which is located at the jet exit and the remainder positioned at intervals of $35mm$.

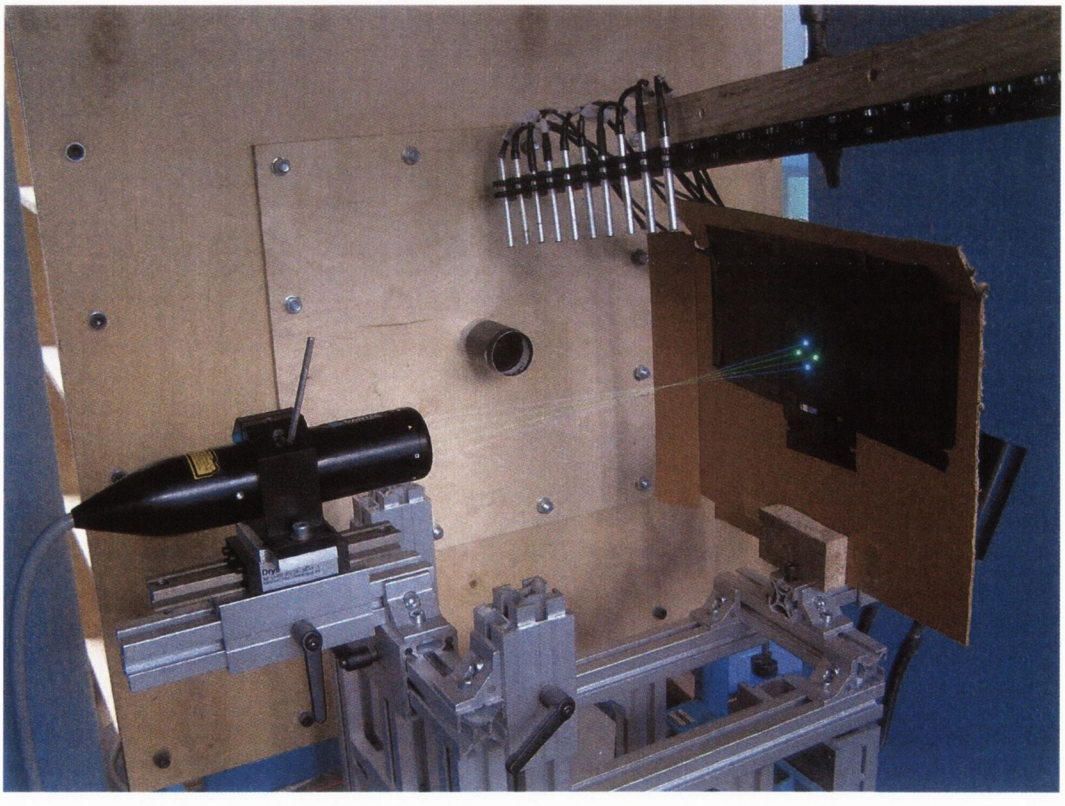

FIGURE 6.2: *Experimental Setup at Trinity - combined LDA and acoustic measurements*

The velocity and acoustic measurements were performed for two jet velocities

of $83m/s$ & $35m/s$, with the microphone array positioned at $r/D = 1.1, 2.0, 3.0$ & 4.5. In chapter 5 it was shown that the hydrodynamic and acoustic regions could be identified when the array was positioned at $r/D = 1.1$ & 4.5, where the first microphone in the array was positioned at the jet exit and the remaining microphones $(2 - 10)$ located downstream near the end of the potential core at spacings of $35mm$. A number of LDA positions were examined as depicted in figure 5.4. The results presented in the following sections where obtained when the LDA measurement volumes were located at the end of the potential core and on the lip line where the axial component (u) and radial component (v) were acquired initially in non-coincident mode. The immediate surrounding area of the test was isolated in order to shield external noise as far as possible.

6.3 Results

The correction procedures associated with the Sample & Hold reconstruction technique have been detailed in chapter 3. This technique was implemented on coincident and non-coincident LDA data which was included in the preliminary analysis of chapter 4. Before the results from the combined velocity and acoustic measurements are presented, some initial analysis of the LDA data is presented. Figure 6.3 shows the estimated spectra of the velocity fluctuation u' and the

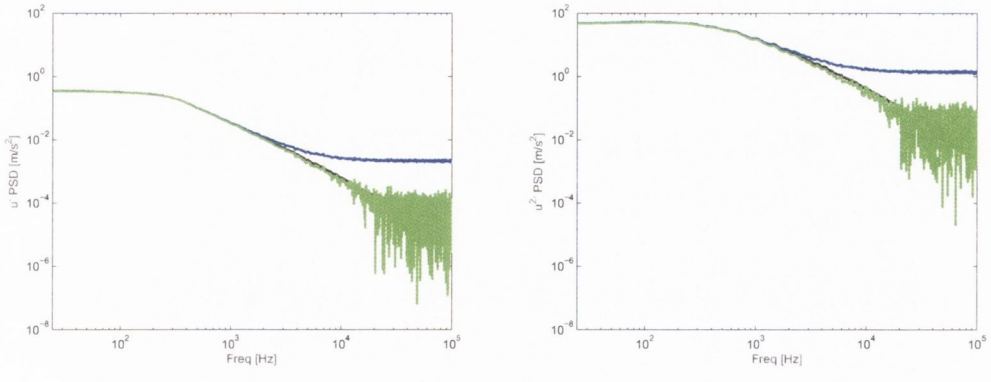

FIGURE 6.3: *LDA auto spectra (a) u', (b) u'^2 - raw S&H, S&H filter corrected, S&H filter and step noise corrected*

Reynolds stress term u'^2. The final estimates are shown in green, (i.e. filter

and step noise corrected). Similarly the auto spectra of the velocity fluctuation v' and the Reynolds stress term v'^2 are shown in figure 6.4. The mean data acquisition rates for the axial and radial components of velocity were 36 & $44kHz$ respectively.

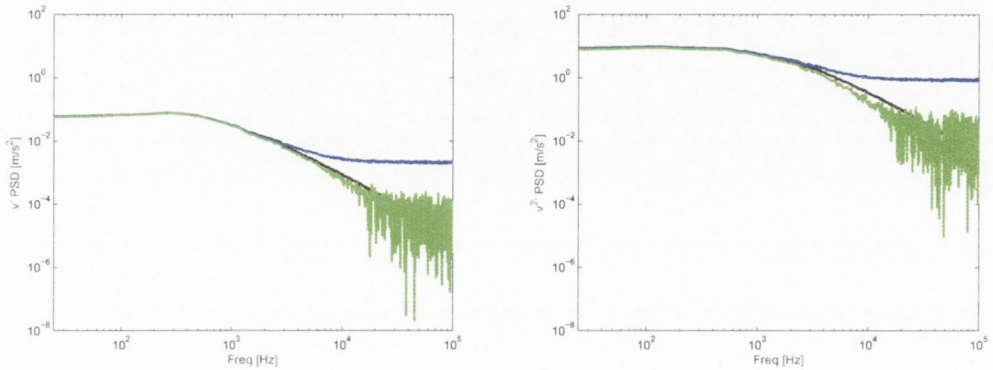

FIGURE 6.4: *LDA auto spectra (a) v', (b) v'^2 - raw S&H, S&H filter corrected, S&H filter and step noise corrected*

With regard to non-coincident LDA data, when two signals are acquired, the cross spectrum is not contaminated by step noise, as detailed in chapter 3. The original and corrected cross spectra between the velocity fluctuations u' and v' are shown in figure 6.5.

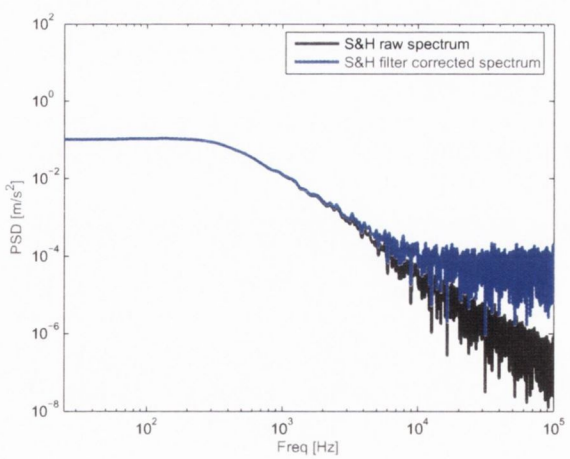

FIGURE 6.5: *LDA cross spectrum between u' & v'*

The coherence between the LDA sources is calculated from the estimated auto

and cross spectra. Figure 6.6 (a) shows the corrected coherence between u' and v', u'^2 & v'^2 and 6.6 (b) between v' & u'^2, v'^2 and u'^2 & v'^2. As discussed in chapter 4 the limiting factor in the coherence estimates is the noise to signal ratio (α).

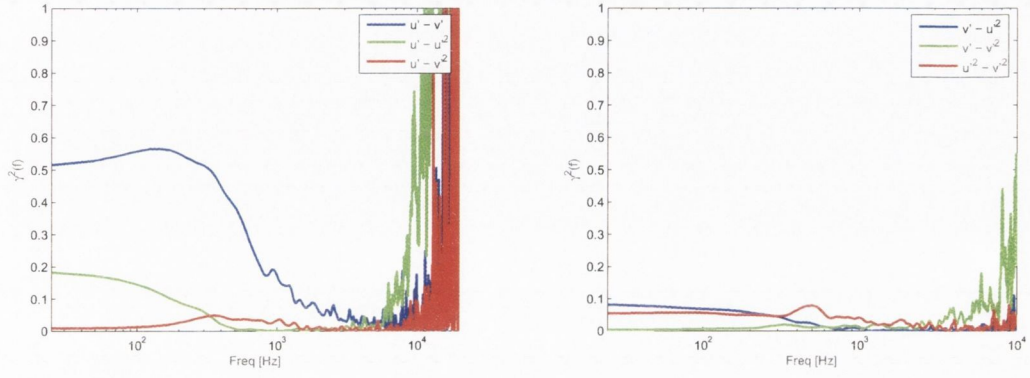

(a) *(b)*

FIGURE 6.6: *Corrected Coherence between LDA sources (a) u' with v', u'^2 & v'^2 (b) v' with u'^2, v'^2 and u'^2 with v'^2*

It was shown that the corrected coherence is greater than one when the noise to signal ratios reach a value of approximately 10, which occurs at the higher frequencies. From this example of the coherence between the LDA sources, it can be seen that mutual coherence exist between the record inputs. The greatest coherence is between the two velocity fluctuations. As expected, coherence exists between u' and u'^2, since this Reynolds stress term is calculated from the velocity fluctuation. However, the coherence between v' and v'^2 is considerably less. These correlations signify that quadratic mixing is present in the velocity data.

As shown, the LDA sources of u', v', u'^2, v'^2 & $u'v'$ have mutual correlation, implying that the conditioning identification technique proposed in section 6.1 must be implemented to extract accurate relationships between the combined velocity and acoustic measurements. The schematic of figure 5.4 shows how the combined tests were configured. Microphone 2 is located upstream of the measurement volume and microphone 3 positioned directly above while the remaining microphones are located downstream of the measurement volume. The first set of measurements (denoted 'Configuration 1') was acquired when the LDA was

located at the end of the potential core and on the lip line, initially with the microphone array located at $r/D = 1.1$ while for the second set of measurements (denoted 'Configuration 2') the microphone array was repositioned to $r/D = 4.5$.

6.3.1 Configuration 1

The acoustic measurements performed for $r/D = 1.1$ were shown to reveal both the hydrodynamic and acoustic regions of the jet. Some extraneous noise was seen in the immediate area surrounding the nozzle, but the microphones positioned further downstream did not register the noise. Through the use of combined LDA and acoustic measurements, it was expected to identify convection and propagation of noise sources to the microphone array positioned at $r/D = 1.1$.

Figure 6.7 illustrates the ordinary coherence where the coherence between each of the LDA sources (u', v', u'^2, v'^2 & $u'v'$ acquired in non-coincident mode) and each microphone in the array is displayed. Insufficient coincident data was acquired in order to examine the Reynolds stress term of $u'v'$ therefore this term will not be completely reliable (as seen from Chapter 4). Since it is mainly the hydrodynamic field that this close array configuration examines, this term will not be of major significance for this setup. In order to examine how each source propagates downstream the partial coherence is calculated, as shown by figure 6.8. As u' is the first input in the model, no conditioning is applied. Hence there is no change in the coherence. However, the remaining sources have been conditioned. The ordinary coherence of u' (figure 6.7 (a)) reveals a spatial decrease, with the maximum coherence being achieved by microphone 3, directly above the measurement volume. The next highest coherence is achieved with microphone 2, which is located upstream, this is then closely followed by microphone 4. The coherence seen by microphones $2-5$ appear to have a similar shape, where the dominant frequency is approximately 150Hz. The coherence frequency range is narrow $(0-600Hz)$ while the coherence for the remaining microphones decays quite rapidly over this band.

The v-component (radial direction) fluctuations can now be examined without interference from the u-component (axial direction). Upon close examination,

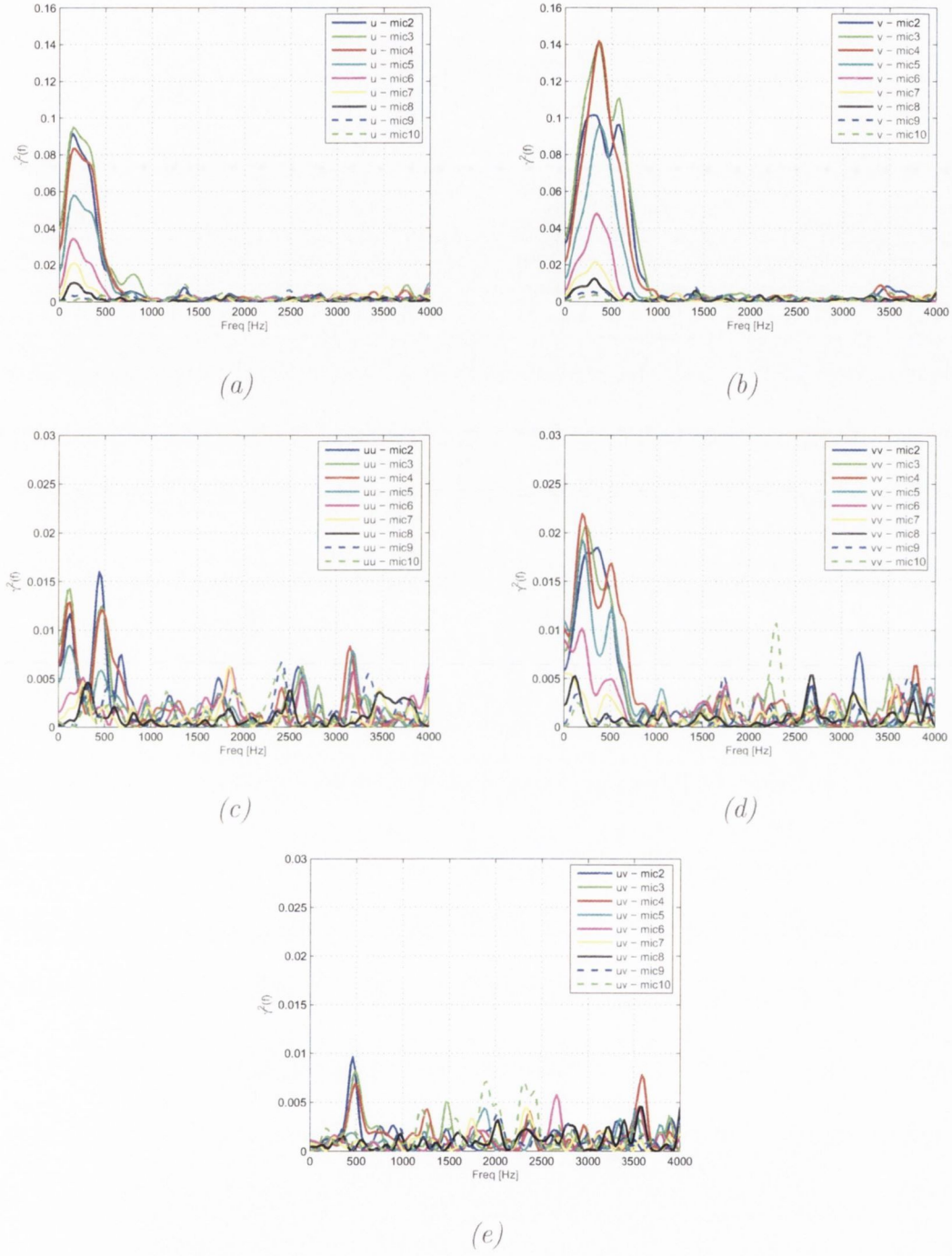

FIGURE 6.7: $r/D = 1.1$: *Ordinary Coherence between LDA sources (a) u', (b) v', (c) u'^2, (d) v'^2, (e) $u'v'$ and microphones ($2 - 10$ conditioned for microphone 1)*

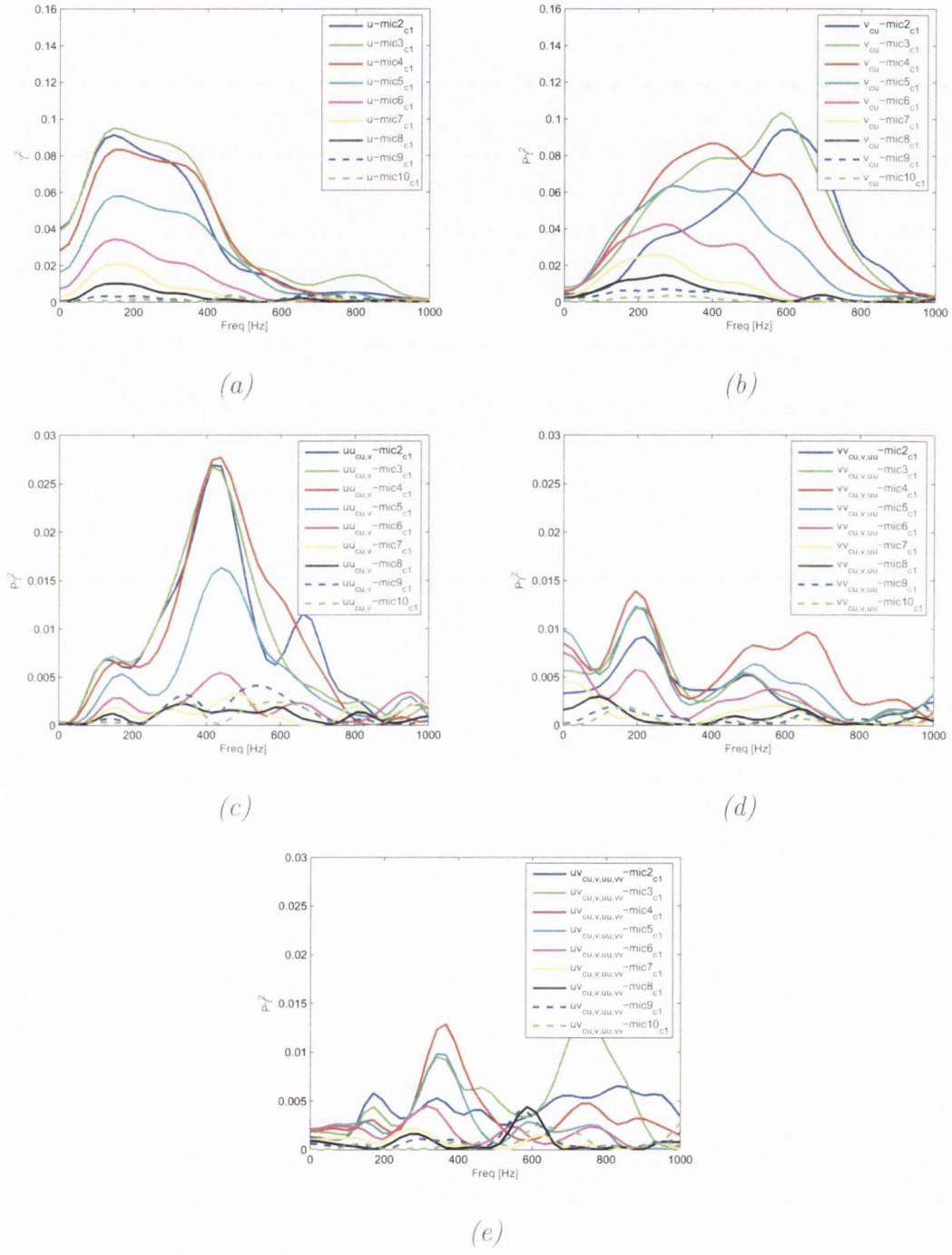

FIGURE 6.8: $r/D = 1.1$: *Partial Coherence between LDA sources and microphones* $(2-10$ *conditioned for microphone* $1)$

it appears that the dominant frequency seen in the ordinary coherence (figure 6.7 (b)) between v' and microphones 3 & 4 is reduced, leaving a frequency of approximately 600Hz dominating these microphones. These higher frequencies appear to dominate the region surrounding the measurement volume. When the source identification technique is implemented, (figure 6.8 (b)) a reduction in the overall contribution seen by microphones $2-8$ occurs. The partial coherence with microphones $4-8$ appear to exhibit a similar pattern, whereas none was obvious from the ordinary coherence. This decreasing pattern, both in size and frequency with the downstream direction, can be similarly observed.

The dominant frequencies seen in figure 6.8 (a) and (b) suggest that, as the vortices within the jet are merging, the lower frequencies start to dominate in the downstream direction. The flutter at the end of the potential core, due to the Kelvin-Helmholtz instabilities, is seen in particular in the radial direction for the microphones positioned close to the measurement volume.

The Reynolds stress u'^2 is a term that in a sense is moving in the axial direction. It would therefore be expected to observe coherence of similar magnitude with the microphones that are located on either side of measurement point. This is exactly the behaviour that is seen with the partial coherence between u'^2 and the microphone array (figure 6.8 (c)). Microphones $2, 3$ & 4 which are positioned upstream, directly above and downstream of the measurement volume in fact show this quite markedly. The dominant frequency seen by these microphones is approximately $425Hz$. Microphone 5 could also be included in this grouping since it sees a similar shape to the others, although at a lower magnitude since the source contribution is propagated downstream. The peak frequency of $425Hz$ corresponds to a Strouhal number of 0.26 based on frequency, exit velocity and diameter. A jet-noise spectrum has a peak at a Strouhal number of 0.3, however the exact Strouhal number will be dependant upon the angle from the jet axis, (Mollo-Christensen et al [54]). This observed peak suggests that the column instability is dominant for the Reynolds stress term u'^2. The remaining microphones are positioned too far away to witness any significant presence of the u'^2 term, since the coherence levels never exceed 0.005.

By comparison, for the other Reynolds stress term v'^2, the dominant frequency that is causing a disturbance in the radial direction is $200Hz$. The coherence levels noted from the partial coherence with v'^2 (figure 6.8 (d)) are half those seen by u'^2, where a very different pattern is also seen. Interestingly microphones 3 & 5 reveal almost the same coherence estimates, even though microphone 3 is positioned directly above the measurement volume and 5 downstream of it, but the source is seen to be most dominant by microphone 4. This observed behaviour depicts how the source term v'^2 is most dominant in the immediate downstream direction. The peak frequency of $200Hz$ corresponds to a Strouhal number of 0.12, which is half the observed Strouhal peak for u'^2. Once again the coherence levels seen from this source by the remaining five microphones are not of sufficient magnitude to suggest any definite conclusion.

With the microphone array positioned at this close r/D location it was shown in the previous chapter that the main region being observed is the hydrodynamic region. Even though the data was acquired in non-coincident mode, for completeness it is included in the coherence estimates. The source term $u'v'$ is most correlated with microphones $2-4$, at frequencies between 450 & $500Hz$ (figure 6.7 (e)). With the conditioning identification technique applied, the partial coherence (figure 6.8 (e)) reduces the previously noted dominant frequencies and now reveals a dominant frequency of $350Hz$, as seen by microphone 4, and a frequency of $750Hz$, as seen by microphone 3. Notwithstanding overall coherence levels are less than 0.015. It should be noted that in order to see more of the acoustic region and consequently more contribution from $u'v'$, that the array should be positioned further from the jet axis.

An alternative way to examine the coherence between the LDA sources and microphones is to observe the contribution of all the LDA sources to each microphone, as shown by figure 6.9. The plots represents what each microphone is measuring in turn from the possible five sources, where the partial coherence is being used. The velocity fluctuations are dominant throughout. The u' term has two dominant frequencies of 200 and 400Hz. This shape is maintained until approximately microphone 8. Beyond this the contribution seen is very small. The

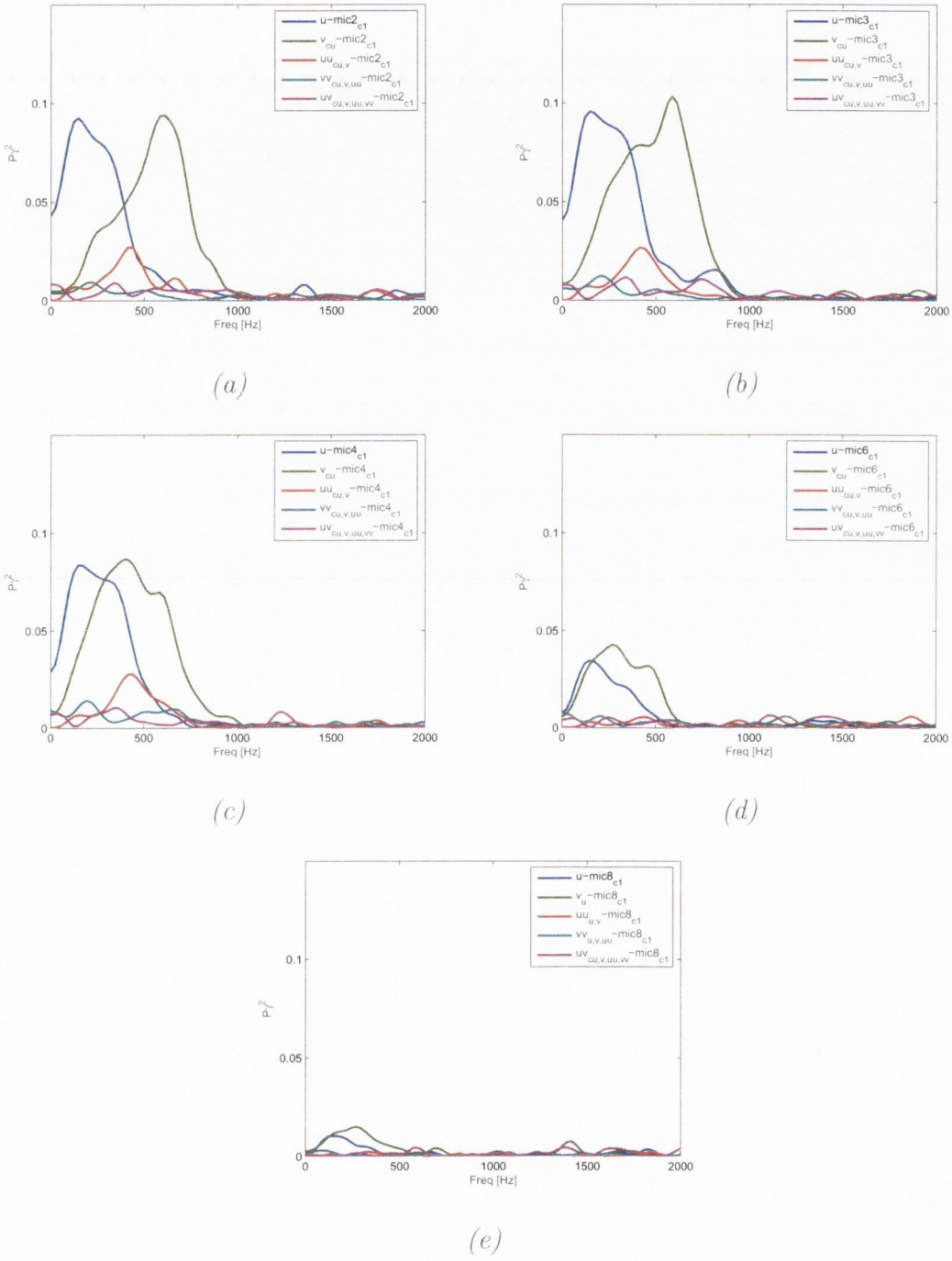

FIGURE 6.9: $r/D = 1.1$: *Partial Coherence between LDA and microphones (a)2, (b)3, (c)4, (d)6, (e)8*

v' component has the effects of u' removed, where the contribution seen by microphones 2 & 3 are different in shape than that seen by the remaining microphones. This is due to the position of the microphones relative to the source, where microphones 2 & 3 are respectively upstream of, and directly above the measurement volume. The remaining microphones which have this similar pattern of reducing coherence are all positioned downstream. The Reynolds stress terms for this close r/D location are not as dominant as the velocity fluctuations. The u'^2 term is coherent up until microphone 5, where its dominant frequency appears to be 425Hz. The contributions of v'^2 and $u'v'$ as seen by the nine microphones never attains a coherence level greater than 0.01.

For a system with multiple inputs and one output, the multiple coherence represents the fraction of power in the output accounted for by simultaneous linear filter relationships with all the inputs. Therefore the calculation of the multiple coherence between the LDA sources and microphones enables the overall contribution of the sources to the noise to be examined for each microphone, as shown in figure 6.10. It can be seen that the most dominant source contribution is seen by microphones 3 & 4. Lower frequencies are seen to dominate further downstream. When the multiple coherence is plotted as a function of the 'kR_j' term, where the perpendicular distance from each microphone to the shear layer axis is used, it is clearly evident that only the hydrodynamic region is seen. In other words, the propagation of these LDA sources are purely hydrodynamic.

In figure 5.27 of chapter 5 the demarcation between the hydrodynamic and acoustic regions was clearly evident at $kR = 1.2$, which corresponded to a frequency range of 0-1000Hz for $r/D = 1.1$. It was observed that the hydrodynamic region was convecting whereas the acoustic region was propagating. From the ordinary and partial coherence between the LDA sources and the microphones, (figures 6.7 and 6.8), the correlation above $1000Hz$ was less than 0.01. Therefore it is unlikely that an examination of the angle of the frequency response function above $1000Hz$ will provide any useful information regarding source propagation. As figure 6.11 shows, when the frequency is greater than $1000Hz$, it is difficult to determine how the sources u' and v' are convecting. For this reason the angle

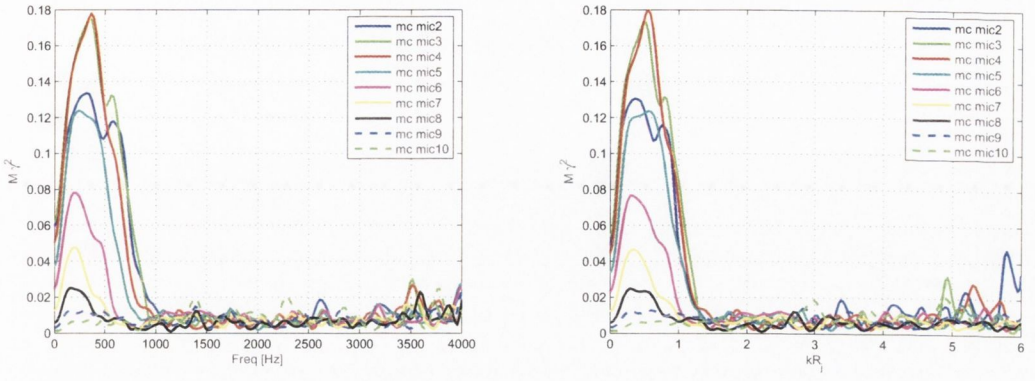

(a) *(b)*

FIGURE 6.10: $r/D = 1.1$: *Multiple Coherence as a function of* (*a*) *frequency,* (*b*) kR_j

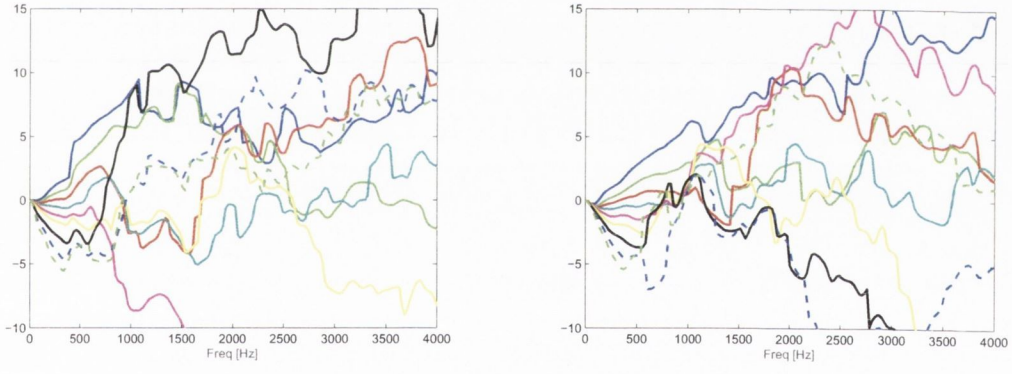

(a) *(b)*

FIGURE 6.11: $r/D = 1.1$: *Angle of Frequency Response Function for* (*a*) u', (*b*) v' *with mic2, mic3, mic4, mic5, mic6, mic7, mic8, mic9 - - & mic10 - -.*

of the frequency response function will only be examined between 0 and $1000Hz$, as shown by figure 6.12 where the normalised angle is plotted as a function of frequency between all five sources and microphones $2 - 10$. Consequently this frequency range confines the examination to the hydrodynamic region, and hence the contribution of the Reynolds stress term $u'v'$ will be of less significance.

Five frequency response functions are calculated from the five input sources which are labelled (a) through (e) in figure 6.12. The angle from the velocity

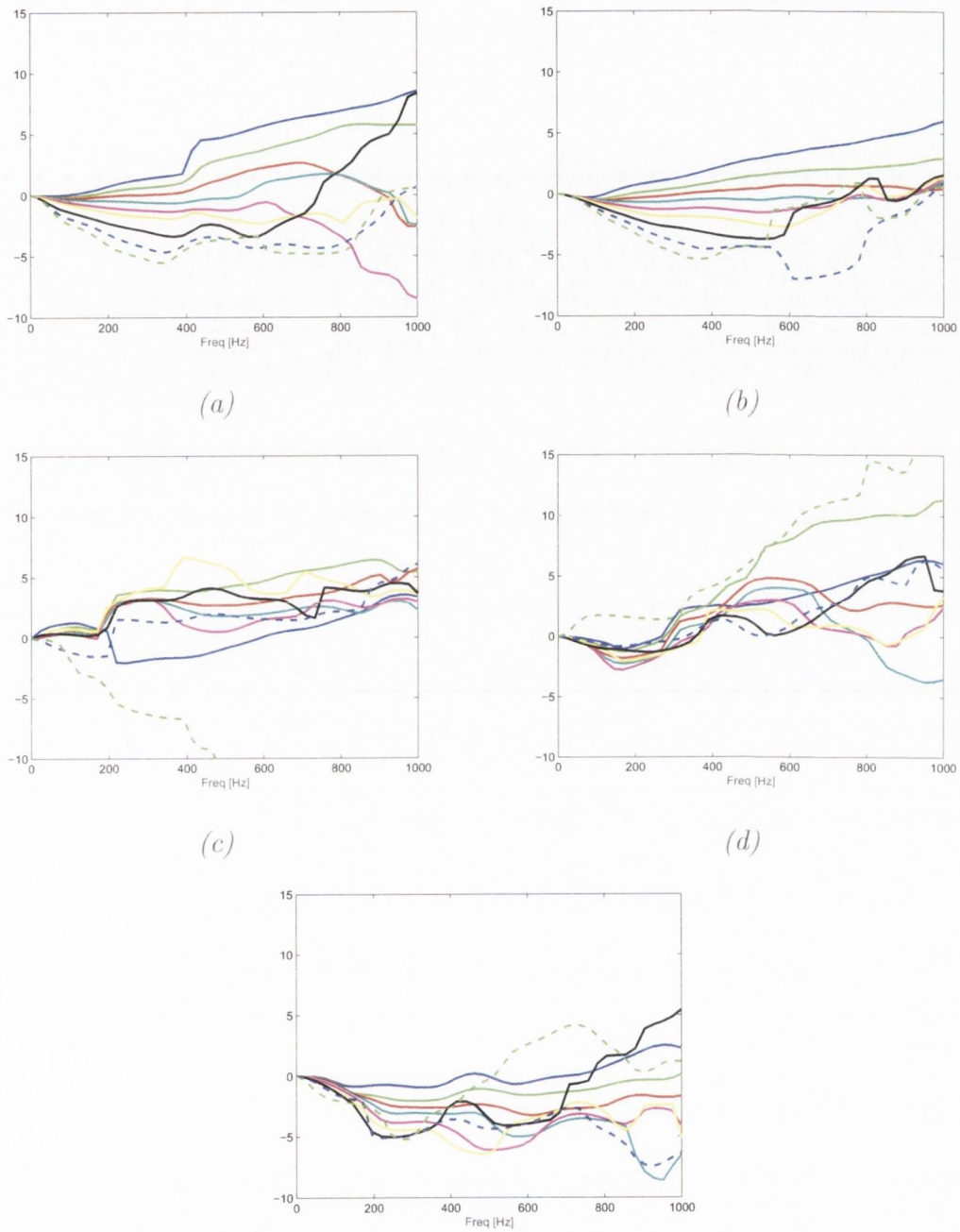

FIGURE 6.12: $r/D = 1.1$: *Angle of Frequency Response Function for* (*a*) u', (*b*) v', (*c*) u'^2, (*d*) v'^2, (*e*) $u'v'$ *with mic2, mic3, mic4, mic5, mic6, mic7, mic8, mic9 - - & mic10 - -.*

fluctuation inputs appears to have a definite trend, as seen by the microphones. It is not clear if any such trend exists for the Reynolds stress inputs. When the partial coherence was examined, (figure 6.8), it was seen by microphones $2-5$ that the Reynolds stress term u'^2 had a dominant frequency of approximately $450Hz$. It may therefore be possible to determine how this source propagates at this frequency. Similarly, the partial coherence of v'^2 revealed a dominant frequency of $200Hz$ which was seen by microphones $2-6$. Some propagation is identifiable in a region between 0 and $200Hz$ when the angle of the frequency response function of input 3, i.e. the Reynolds stress term v'^2, is calculated.

The partial coherence for the final Reynolds stress term of $u'v'$ revealed little insight into this source term for two reasons. Firstly, because the hydrodynamic region is measured predominantly at $r/D = 1.1$, and secondly, the LDA data was acquired in non-coincident mode.

Figure 6.13 (a) shows both the partial coherence and 6.13 (b) the angle of the frequency response function for coincident $u'v'$. This data was obtained with the LDA measurement volumes positioned $0.3D$ from the jet axis and $6D$ from the jet exit. Despite the difference in measurement location, there does not seem to be an improvement in the angle of the frequency response function of the source term $u'v'$ obtained from this coincident data.

6.3.2 Configuration 2

In chapter 5 it was shown that the noise radiating from the front panel of the wind tunnel affected all microphone measurements when the array was positioned at $r/D = 4.5$. In order to provide insight into the propagation of acoustic noise sources combined LDA and acoustic measurements for this configuration were performed.

The ordinary coherence between the velocity fluctuations and the microphones is shown in figure 6.14 (a) & (c) as unconditioned coherence, and 6.14 (b) & (d) with the effects of microphone 1 conditioned out. The ordinary coherence of u' reveals peaks at 200 & $1000Hz$. When microphone 1 is conditioned out there is an increase in the coherence, particularly when the microphones are positioned closer

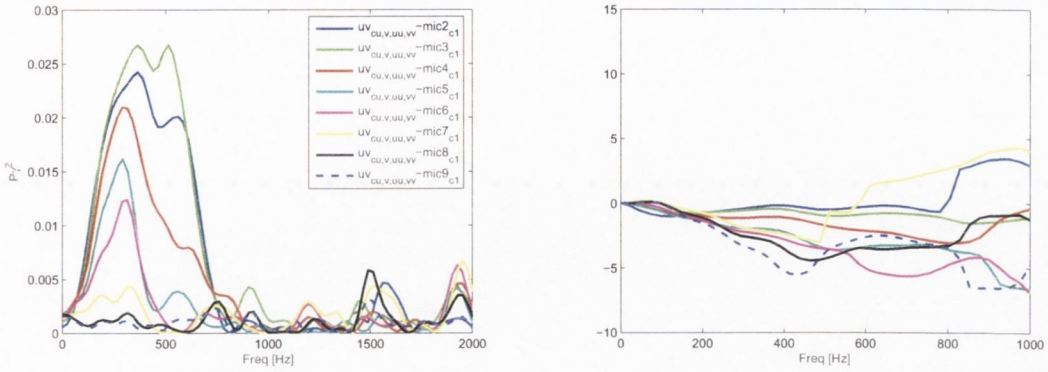

(a) *(b)*

FIGURE 6.13: $r/D = 1.1$: *Angle of Frequency Response Function for (a) Partial coherence $u'v'$, (b) Angle frequency response function $u'v'$ with mic2, mic3, mic4, mic5, mic6, mic7, mic8, & mic9 - -*

to the measurement volume. The dominant peak in the ordinary coherence of v' is $200Hz$. A secondary peak of $1500Hz$ can also be seen, measured by microphone 10. Notwithstanding the coherence between the axial velocity fluctuations and the microphones never exceeds 0.01. When microphone 1 is conditioned out some increase in coherence can be seen, particularly for microphones 2 & 3. A similar analysis is applied for the Reynolds stress terms, with the ordinary coherence shown in figure 6.15 (a),(c), & (e) and the conditioned ordinary coherence in 6.15 (b),(d), & (f). When this is performed very little overall discernable difference is observed.

When the conditioning identification technique is applied the partial coherence is examined, as shown by figure 6.16. In this instance the microphones are conditioned for microphone 1. As before u' is the first input, therefore the partial coherence is not altered by this technique. When the effects of u' are removed from v', (figure 6.16 (b)), the previously dominant coherent frequency of $200Hz$ is reduced and the coherence at $1000Hz$ is dramatically increased. The partial coherence of the Reynolds stress term u'^2 is increased at $200Hz$, similarly a slight increase occurs for v'^2. A global increase in the partial coherence for the final Reynolds stress term of $u'v'$ occurs, but in this instance the coherence is less than

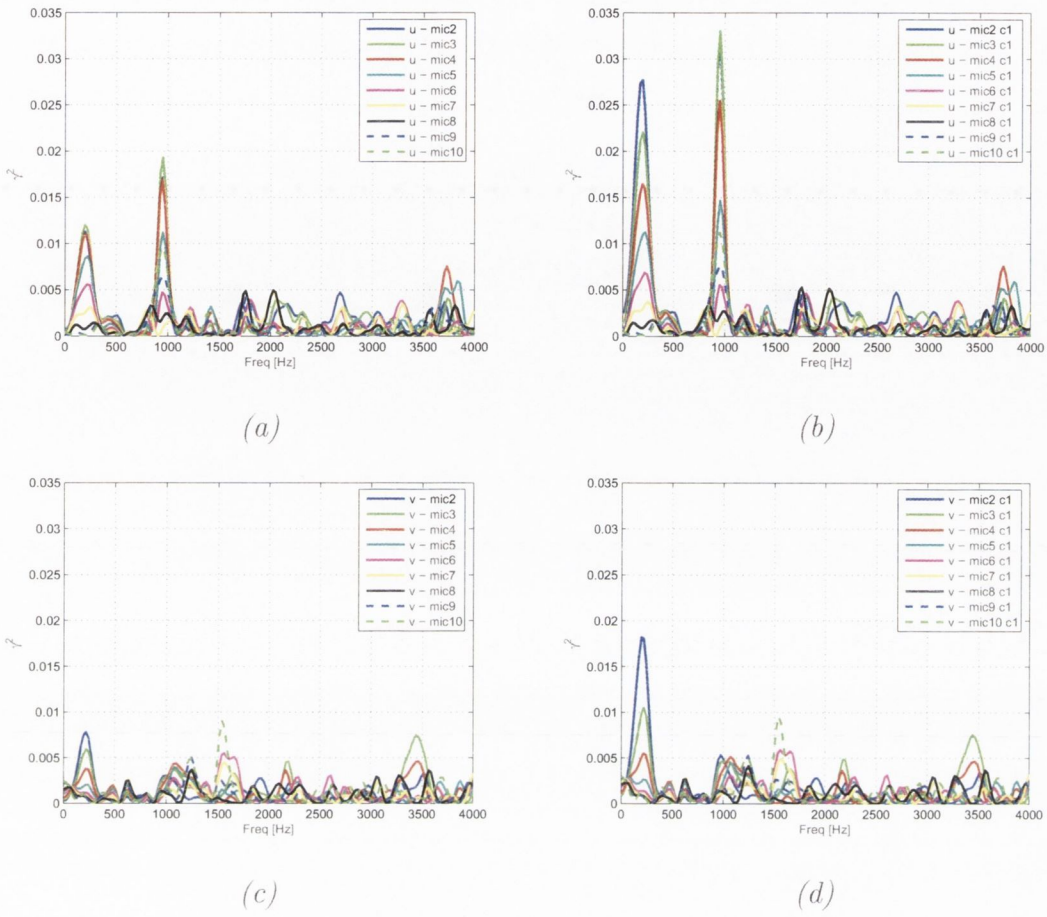

FIGURE 6.14: *r/D = 4.5: Ordinary Coherence between (a) u′ & microphones 2 – 10, (b) u′ & microphones conditioned for microphone 1, (c) v′ & microphones 2 – 10, (d) v′ & microphones conditioned for microphone 1*

0.07.

The overall contribution of the five sources, as observed by each individual microphone, is shown in figure 6.17. It is obvious that the dominant coherent frequencies are approximately 200 & $1000Hz$.

The angle of the frequency response function is examined for each LDA source, as previously performed for Configuration 1, (figure 6.18). From this analysis, it is clear that there is no conclusive evidence of noise source propagation. While some noise source propagation may be occurring there is not sufficient evidence to justify this, since the partial coherence only identified dominant vibration frequencies.

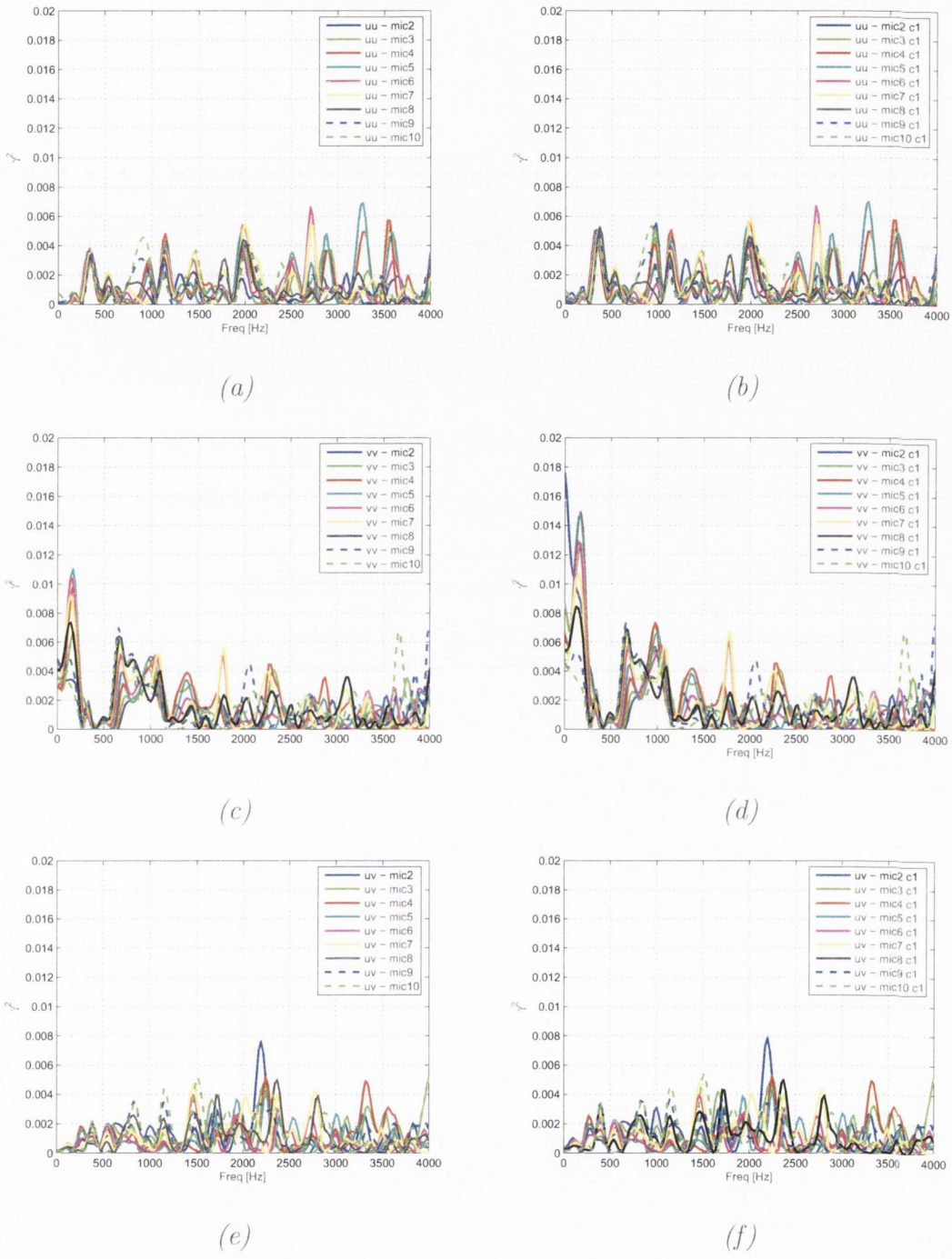

FIGURE 6.15: *$r/D = 4.5$: Ordinary Coherence between (a) u'^2 & microphones $2-10$, (b) u'^2 & microphones conditioned for microphone 1, (c) v'^2 & microphones $2-10$, (d) v'^2 & microphones conditioned for microphone 1, (e) $u'v'$ & microphones $2-10$, (f) $u'v'$ & microphones conditioned for microphone 1*

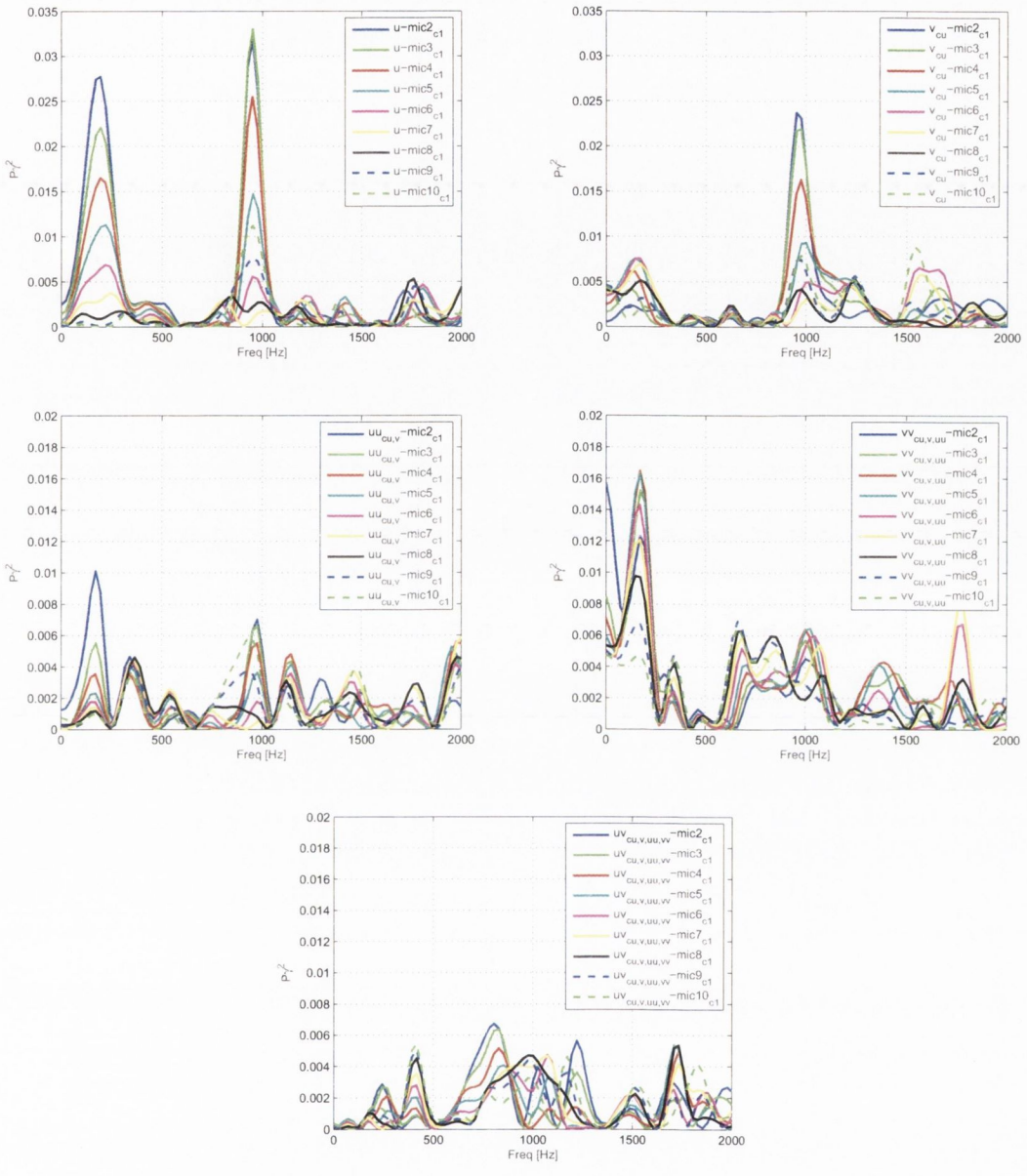

FIGURE 6.16: $r/D = 4.5$: *Partial Coherence between LDA sources and microphones* ($2 - 10$ *conditioned for microphone* 1)

6.4 Concluding Remarks

A source identification technique has been implemented on combined LDA and acoustic measurements. This technique allows noise source mechanisms and their propagation to be examined.

The combined measurements were carried out using two configurations. The

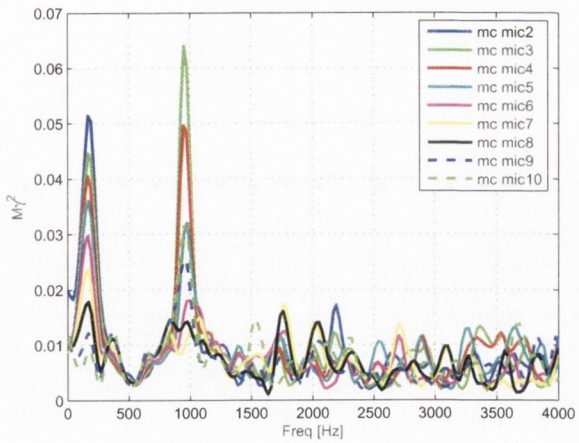

FIGURE 6.17: $r/D = 4.5$: *Multiple Coherence*

first configuration enabled both the hydrodynamic and acoustic regions to be measured successfully. The partial coherence between the LDA sources and the microphones, for this configuration, clearly revealed how the different sources behave. It was shown that the radial velocity fluctuation was greatest when measured directly above the LDA position. A clear dominant frequency was noted which decreased in the downstream direction as the source dissipated. Whereas in the case of the axial velocity fluctuation, the dominant frequency remained constant in this direction.

The partial coherence of u'^2 revealed that this source term is most correlated with those microphones that are located in the vicinity of the measurement position, whereas v'^2 is more correlated with the downstream microphones. Since it is the hydrodynamic region of the jet that is examined for the frequency range 0 to $1000Hz$, the Reynolds stress term $u'v'$ is not of significance for this configuration.

The angle of the frequency response function of the velocity fluctuations revealed a definite trend which demonstrated the convection nature of these source terms. However for the Reynolds stress terms there is no such obvious trend. The use of coincident LDA data did not provide any further insight into the propagation of the Reynolds stress term $u'v'$.

In order to measure more of the acoustic, and subsequently less of the hydrodynamic region, the second configuration was examined. The partial coherence

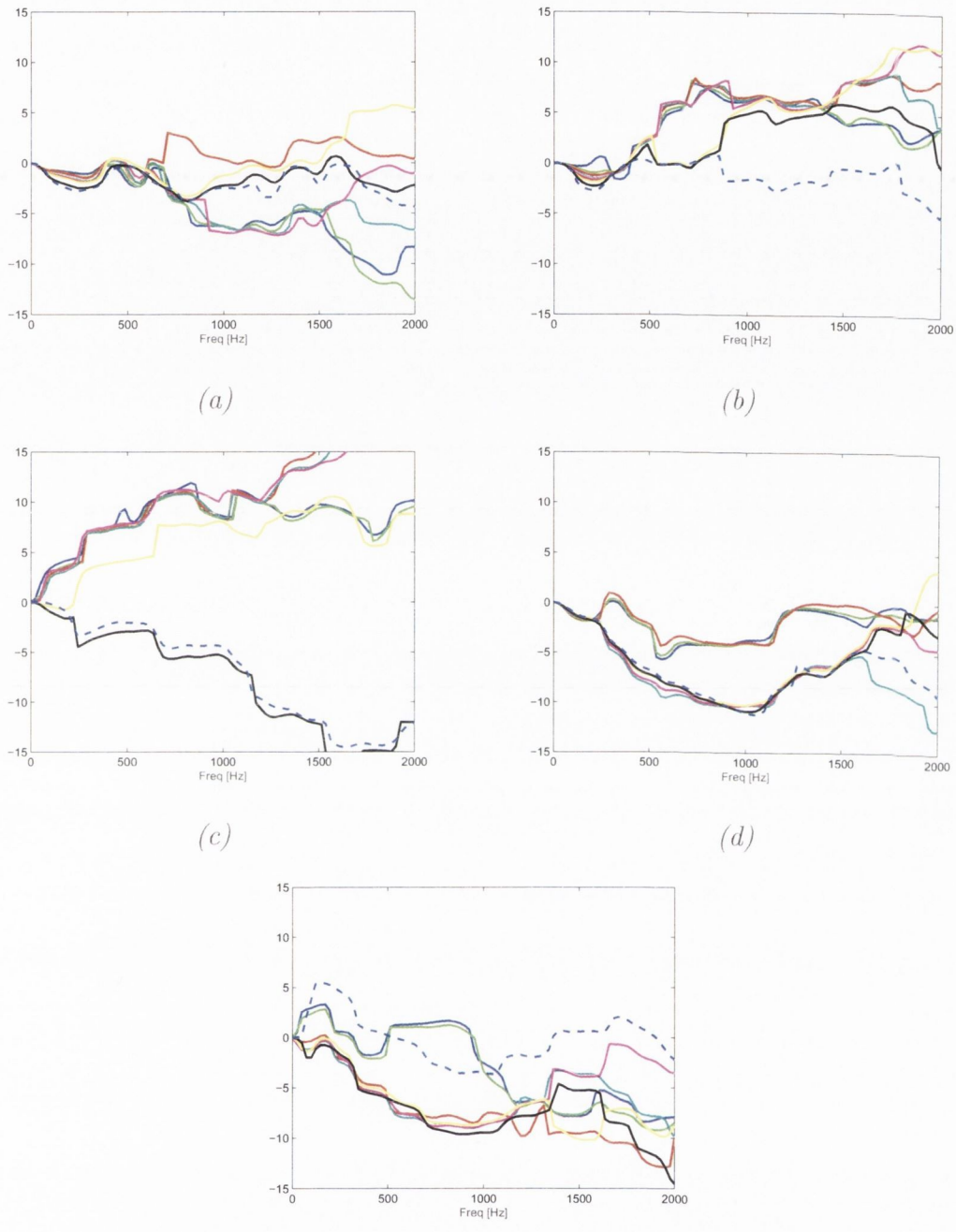

(a) (b) (c) (d) (e)

FIGURE 6.18: $r/D = 4.5$: *Angle of Frequency Response Function for* (a) u', (b) v', (c) u'^2, (d) v'^2, (e) $u'v'$ *with mic2, mic3, mic4, mic5, mic6, mic7, mic8, mic9 - - & mic10 - -.*

for this configuration revealed dominant frequencies that were associated with the vibration analysis carried out previously in chapter 5. This implies that these vibrations are inherent in the measured velocity field. The source identification technique revealed that some acoustic propagation was occurring, although its origin was inconclusive.

Chapter 7

Conclusions & Future Work

The work reported in this thesis has examined the means by which noise source mechanisms in jets can be measured and identified. To do this, combined LDA and acoustic measurements were performed.

For the LDA measurements, a Sample & Hold time domain reconstruction technique, proposed by Simon & Fitzpatrick [40], was implemented.

- Since the study of jet noise and noise source mechanisms requires a knowledge of the Reynolds stress terms, this therefore suggests that the Sample & Hold method must be expanded to deal with possible coincident signals.

Having defined the Sample & Hold correction technique, a validation procedure with the Slot Correlation method was performed on experimental data. This comparison was performed in both the frequency and correlation domains.

- Some inconsistencies were noted in the coherence estimates from Slot Correlation, and slight differences occurred between estimates of convection velocity and length and time scales using both techniques.

- Sample & Hold provided better estimates in the frequency domain than those obtained using Slot Correlation, while the differences noted in the correlation domain estimates were most likely due to the manner in which each technique calculates this domain.

- A combination of both Sample & Hold and Slot Correlation best suits an analysis of both the frequency and correlation domains from random LDA data.

An analysis was performed on the two modes of LDA acquisition, i.e. coincident and non-coincident. This analysis has regard to the implications of how the Reynolds stress term $u'v'$ is calculated.

- Some differences occurred at low frequencies in the spectral estimates of $u'v'$.
- Coincident data points were inherent in non-coincident acquisition, however these coincident points did not appear to affect the spectral estimates from the non-coincident data.
- In order to correctly estimate the Reynolds stress term, the LDA data should be acquired in coincident mode.

Source identification requires that the hydrodynamic and acoustic regions of the jet be differentiated. A preliminary acoustic analysis was performed to determine if these regions could clearly be seen. Two microphone array locations were employed.

- With the array positioned at $r/D = 1.1$ both regions were successfully identified.
- The convecting hydrodynamic and propagating acoustic regions were shown from both the coherence and phase estimates.
- When the array was repositioned to $r/D = 4.5$, less of the hydrodynamic and more of the acoustic region was examined.
- Vibrations originating from the front panel of the wind tunnel were contaminating the microphone measurements, for this array location.
- Attempts were made to condition out this additional noise, but there was not sufficient jet noise at this location to be recorded.

- Although it was possible to determine that some propagation was occurring at certain frequencies, it was not possible to conclude, on a qualitative basis, its definitive source.

Combined LDA and acoustic measurements, with the LDA positioned at the end of the potential core and on the lip line, and the microphone array at $r/D = 1.1$ & 4.5, were performed to examine source identification and propagation.

- The first configuration identified that the greatest contribution from the sources was seen by the microphones positioned directly above and immediately downstream of the LDA position.

- The most dominant sources were the velocity fluctuations. The column instability was identified from both the Reynolds stress terms of u'^2 and v'^2.

- The array was positioned too close to the jet axis to conclude how the source term $u'v'$ behaved.

- The second configuration aimed to reduce the effects of the hydrodynamic region and increase that of the acoustic. However, the vibrations that were associated with the front panel of the wind tunnel, registered by the microphones at $r/D = 4.5$, were also inherent in the LDA velocity measurements.

The techniques and developments described above have the potential to advance further knowledge and understanding of the important area of jet noise. In order to fully explore that potential it will be necessary to apply these source analysis methods to an investigation of jet noise at higher acoustic levels than those achievable for the purpose of this thesis. However, there are sufficient grounds established herein for believing that further research in this area is warranted.

Bibliography

[1] Geneva, W. H. O., 1999, "Guidelines for community noise," p. 19.

[2] Ffowcs-Williams, J., 1977, "Aeroacoustics," *Annual Review in Fluid Mechanics,* **9**, pp. 447–468.

[3] Ribner, H. S., 1964, "The generation of sound by turbulent jets," *Advances in Applied Mechanics,* **8**, pp. 104–178.

[4] George, 1989, "The self-perservation of turbulent flows and its relation to initial conditions and coherent structures," *Recent Advances in Turbulence.*

[5] Lighthill, M. J., 1952, "On sound generated aerodynamically i: General theory," *Proceedings of the Royal Society,* **221**, pp. 564–587.

[6] Tam, C. K. W., 1998, "Jet noise: Since 1952," *Theoretical Computational Fluid Dynamics,* **10**, pp. 393–405.

[7] Crow, S. C., and Champagne, F. H., 1971, "Orderly structure in jet turbulence," *Journal of Fluid Mechanics,* **48**, pp. 547–591.

[8] Brown, G. L., and Roshko, ., 1974, "On density effects and large structure in turbulent mixing layers," *Journal of Fluid Mechnanics,* **64**, pp. 715–816.

[9] Laufer, J., 1974, "On the mechanism of noise generated by turbulence," *Omaggio a Carlo Ferrari, Libreria Editrice Universitarita Levrotto & Bella, Torino*, pp. 451–464.

[10] Hussain, A. K. M. F., 1986, "Coherent structures and turbulence," *Journal of Fluid Mechanics,* **173**, pp. 303–356.

[11] Ffowcs-Williams, J. E., 1963, "The noise from turbulence convected at high-speed," *Philos. Trans. Royal Society London Series A,* **255**, pp. 469–503.

[12] Ribner, H. S., 1969, "Quadrupole correlation governing the pattern of jet noise," *Journal of Fluid Mechanics,* **38**, pp. 1–24.

[13] Atvars, J., Schubert, L. K., and Ribner, H. S., 1965, "Refraction of sound from a point source placed in an air jet," *Journal of Acoust Society America,* **37**, pp. 168–170.

[14] Tam, C. K. W., 1991, "Jet noise generated by large-scale coherent motion," *Aeroacoustics of Flight Vehicles: Theory and Practice,* **1**, pp. 311–390.

[15] Morrison, G. L., and McLaughlin, D. K., 1979, "Noise generation by instabilties in low reynolds number supersonic jets," *Journal of Sound and Vibration,* **65**, pp. 177–191.

[16] Arndt, R. E. A., Long, D. F., and Glauser, M. N., 1997, "The proper orthogonal decomposition of pressure fluctuations surrounding a turbulent jet," *Journal of Fluid Mechanics,* **340**, pp. 1–33.

[17] Jordan, P., Coiffet, F., Delville, J., Gervais, Y., and Ricard, F., 2004, "Acoustic-hydrodynamic interaction on the entrainment region of subsonic jet flow," *10th AIAA/CEAS Aeroacoustics Conference*, p. 3020.

[18] Hileman, S., 2000, "An attempt to identify noise generating turbulent structures in a high speed axisymmetric jet," *AIAA conference 2000*, pp. 2000–2020.

[19] Lighthill, M. J., 1993, *Computational Aeroacoustics* Springer Verlag.

[20] Self, R. H., 2004, "Jet noise prediction using the lighthill acoustic analogy," *Journal of Sound and Vibration,* **275**, pp. 757–768.

[21] Bogey, C., Bailly, C., and Juve, D., 1999, "Computational of mixing layer noise using large eddy simulation," *AIAA/CEAS Aeroacoustics Conference.*

[22] Andersson, N., 2005, "A study of subsonic turbulent jets and their radiated sound using large-eddy simulation," *PhD Thesis, Department of Applied Mechanics, Chalmers University of technology.*

[23] Spalart, P. R., 1999, *Strategies for turbulence modelling and simulations, Engineering turbulence modelling and experiments 4* W. Rodi and D. Laurance, Elsevier.

[24] Shur, M., Spalart, P., Strelets, M., and Travin, A., 1999, *Strategies for turbulence modelling and simulations, Engineering turbulence modelling and experiments 4* W. Rodi and D. Laurance, Elsevier.

[25] Tam, C. K. W., and Aurialt, L., 1999, "Jet mixing noise from fine scale turbulence," *AIAA Journal,* **37**, pp. 145–153.

[26] Bailly, C., Lafon, P., and Candel, S., 1997, "Subsonic and supersonic jet noise predictions from statistical source models," *AIAA journal,* **35**, pp. 1688–1696.

[27] Bailly, C., and Juve, D., 1999, "A stochastic approach to compute subsonic noise using linearised euler equations," *5th AIAA/CEAS Aeroacoustic Conference*, p. 1872.

[28] Bailly, C., and Juve, D., 2000, "Numerical solution of acoustic propagation problems using linearised euler equations," *AIAA Journal,* **38**, p. 22.

[29] Self, R. H., 2002, "Progress report on acoustic source model formulation," *JEAN Task 2.1 Report.*

[30] Kerhervé, F., Power, O., Fitzpatrick, J., and Jordan, P., 2004, "Determination of turbulent scales in subsonic and supersonic jets from ldv measurements," *Proceedings of the 12th International Symposium Application of Laser Techniques to Fluid Mechanics.*

[31] Gaster, and Roberts, 1975, "Spectral analysis of randomly sampled signals," *Journal Inst Maths Appl,* **15**, pp. 195–216.

[32] Buchave, P., and H. H. von Benzon, C. N. R., 1990, "Lda bias: Comparison of measurement errors from simulated and measured data," *Proceedings of the 5th International Symposium on the Application of Laser Anemometry to Fluid Mechanics*, p. 29.3.

[33] Lee, D. H., and Sung, H. J., 1994, "Assessment of turbulent spectral bias in laser doppler velocimetry," *Experiments in Fluids*, **16**, pp. 223–235.

[34] Britz, D., and Antonio, R., 1996, "A comparison of methods of computing power spectra of lda signals," *Measurements Sci Technol*, **7**, pp. 1042–1053.

[35] Benedict, L. H., Nobach, H., and Tropea, C., 1998, "Benchmark tests for the estimation of power spectra from lda signals," *9th International Symposium on Applications of Laser Techniques in Fluid Mechanics*, p. 32.6.

[36] Adrian, R. J., and Yao, C. S., 1987, "Power spectra of fluid velocities measured by laser doppler anemometry," *Experimental Fluids*, **5**, pp. 17–28.

[37] Edwards, R. V., and Jensen, A. S., 1983, "Particle-sampling statistics in laser anemometers: sample-and-hold systems and saturable systems," *Journal of Fluid Mechanics*, **133**, pp. 397–411.

[38] Boyer, L., and Searby, G., 1986, "Random sampling: Distortion and reconstruction of velocity spectra from fast fourier transform analysis of the analog signal of a laser doppler processor," *Journal of Applied Physics*, **60**, pp. 2699–2707.

[39] Nobach, H., Muller, E., and Tropea, C., 1998, "Efficient estimation of power spectral density from laser doppler anemometer data," *Experiments in Fluids*, **24**, pp. 499–509.

[40] Simon, L., and Fitzpatrick, J., 2004, "An improved sample-and-hold reconstruction procedure for estimation of power spectra from lda data," *Experiments in Fluids*, **37**, pp. 272–280.

[41] Fitzpatrick, J., and Simon, L., 2005, "Estimation of cross-power spectra using sample-and-hold reconstruction of laser doppler anemometry data," *Accepted for publication in Experiments in Fluids*.

[42] Mayo, W. T. J., Shay, M. T., and Titter, S., 1974, "Digital estimation of turbulent power spectra from burst counter ldv data," *Proceedings 2nd Internation Workshop on Laser Velocimetry, Purdue University*, pp. 16–26.

[43] van Maanen, H. R. E., and Tummers, M. J., 1996, "Estimation of the autocorrelation function of turbulent velocity fluctuations using the slotting technique with local normalisation," *Proceedings of the 8th International Symposium Application of Laser Techniques to Fluid Mechanics*, p. 36.4.

[44] Benedict, L. H., Nobach, H., and Tropea, C., 2000, "Estimation of turbulent velocity spectra from laser doppler data," *Measurements of Science and Technology*, **11**, pp. 1089–1104.

[45] van Maanen, H. R. E., Nobach, H., and Benedict, L. H., 10, "Improved estimator for the slotted autocorrelation function of randomly sample lda data," *Measurements of Science and Technology*, **1999**, pp. L4–7.

[46] Jordan, P., Gervais, Y., Valiere, J.-C., and Foulan, H. "Final results from single point measurements, deliverable 3.4," *EU Research Programme*.

[47] Jordan, P., and Gervais, Y., 2003, "Modelling self and shear noise mechanisms in anisotropic turbulence," *9th AIAA/CEAS Aeroacoustics Conference and Exhibit*, pp. 2003–3318.

[48] Laurendeau, E., Jordan, P., Gervais, Y., and Kerhervé, K., 2003, "Estimation of self and shear noise directivity patterns from subsonic jets via synchronous acoustic/aerodynamic measurements," *Euronoise, Naples*, pp. SC37–375.

[49] Chatellier, L., and Fitzpatrick, J., 2005, "Spatio-temporal correlation analysis of turbulent flows using global and single-point measurements," *Experiments in Fluids*, **38**, pp. 563–575.

[50] Bendat, J. S., and Piersol, A. G., 2000, *Random Data Analysis and Measurement Procedures*, 3rd ed. John Wiley & Sons.

[51] Rice, H. J., and Fitzpatrick, J. A., 1991, "A procedure for the identification of linear and non-linear multi-degree-of-freedom systems," *Journal of Sound and Vibration,* **149**, pp. 397–411.

[52] Richards, C. M., and Singh, R., 2000, "Comparison of two non-linear system identification approaches derived from reverse "path" spectral analysis," *Journal of Sound and Vibration,* **237(2)**, pp. 361–376.

[53] Roberts, J. B., Dunne, J. F., and Debonas, A., 1995, "A spectral method for estimation of non-linear system parameters for measured response," *Probabilistic Engineering Mechanics,* **10**, pp. 199–207.

[54] Mollo-Christensen, E., Kolpin, M. A., and Martuccelli, J. R., 1964, "Experiments on jet flows and jet noise far-field spectra and directivity patterns," *Journal of Fluid Mechanics,* **18**, p. 285.